A Study of J/ψ Production at the LEP e^+e^- Collider; and the Implementation of the DELPHI Slow Controls System

Timothy John Adye
Lincoln College, Oxford

A thesis submitted for the degree of Doctor of Philosophy
at the University of Oxford
April 1998

A Study of J/ψ Production at the LEP e^+e^- Collider; and the Implementation of the DELPHI Slow Controls System

Timothy John Adye
Lincoln College, Oxford

A thesis submitted for the degree of Doctor of Philosophy
at the University of Oxford
April 1998

Abstract

This thesis describes two separate areas of work conducted for the DELPHI detector at LEP.

The first concerns the Slow Controls of the DELPHI detector, which enable a single operator to oversee the proper functioning of the apparatus and to diagnose faults as they occur. The hardware and software of this system, as well as their interface to the experiment and the operator, are described. Some conclusions are drawn from seven years' design work and the initial six years' operation of DELPHI.

Secondly, a study is made of the production, at e^+e^- collision centre of mass energies close to the Z^0 resonance, of J/ψ mesons, decaying to $\mu^+\mu^-$. J/ψ mesons produced via a B-hadron are used to measure the mean B lifetime,

$$\tau_B = (1.53 \pm 0.11\ (\text{stat.}) \pm 0.06\ (\text{syst.}))\ \text{ps}.$$

A measurement is also made of the fraction of J/ψs produced promptly at the e^+e^- collision point,

$$\frac{N(Z^0 \to \text{prompt J}/\psi X)}{N(Z^0 \to \text{J}/\psi X)} = (9.6 \pm 3.2\ (\text{stat.}) \pm 1.2\ (\text{syst.}))\%.$$

This method is largely model-independent.

Contents

Introduction **1**

Acknowledgements **3**

List of Common Abbreviations **5**

1 J/ψ Production from the Z^0 **9**

2 The DELPHI Detector **13**
2.1 The LEP Machine 13
2.2 Detector Overview 16
2.3 Tracking Detectors 20
2.3.1 Vertex Detector (VD) 20
2.3.2 Inner Detector (ID) 27
2.3.3 Time Projection Chamber (TPC) 27
2.3.4 Outer Detector (OD) 28
2.3.5 Forward Chambers A (FCA) 29
2.3.6 Forward Chambers B (FCB) 29
2.4 Ring Imaging Cherenkov Counters (RICH) 29
2.5 Calorimetry 30
2.5.1 High-density Projection Chamber (HPC) 30
2.5.2 Forward Electromagnetic Calorimeter (EMF) 31
2.5.3 Hadron Calorimeter (HAC) 31
2.6 Muon Chambers 32
2.6.1 Barrel Muon Chambers (MUB) 32
2.6.2 Forward Muon Chambers (MUF) 34
2.6.3 Surround Muon Chambers (MUS) 35
2.7 Scintillators 36
2.8 Luminosity Monitors 36
2.8.1 Small Angle Tagger (SAT) 37
2.8.2 Small Angle Tile Calorimeter (STIC) 37
2.8.3 Very Small Angle Tagger (VSAT) 37
2.9 Solenoid 38
2.10 Data Acquisition (DAS) and Trigger 38
2.11 Event Reconstruction 40
2.11.1 Offline Processing 40
2.11.2 Track Reconstruction 43
2.11.3 Beamspot 45

2.11.4 Muon Identification 45
2.12 Detector Simulation 48

3 Slow Controls **51**
3.1 Introduction and Overview 51
3.2 Detector Requirements 54
3.2.1 General Principles 54
3.2.2 General Features 55
3.2.3 Barrel Tracking Detectors 56
3.2.4 Forward Tracking Chambers 57
3.2.5 Ring Imaging Cherenkov Counters (RICH) 58
3.2.6 Calorimetry 59
3.2.7 Muon Chambers 60
3.2.8 Scintillators 61
3.2.9 Luminosity Monitors 61
3.2.10 Other Systems 62
3.3 Front-end Systems (G64) 62
3.3.1 G64 Hardware 64
3.3.2 G64 Software 67
3.4 VAX Systems 70
3.4.1 Hardware 70
3.4.2 VAX System Software 71
3.5 VAX Monitoring and Control Programs 72
3.5.1 Elementary Process (EP) 72
3.5.2 Expert Interaction (HIPE) 74
3.6 Error Message Handling (EMU) 75
3.6.1 Use of EMU in DELPHI 76
3.6.2 EMU Display 77
3.7 Databases 78
3.7.1 Slow Controls Configuration Database 79
3.7.2 Status Update Database 79
3.8 High-level Representation (SMI) 80
3.8.1 Use of SMI in DELPHI 80
3.8.2 SMI Display 81
3.8.3 Big Brother 85
3.9 Ancillary Systems 87
3.9.1 Gas Systems 88
3.9.2 General Surveillance System (GSS) 88
3.9.3 Solenoidal Magnet 89
3.9.4 LEP Accelerator 90
3.10 Operations 90
3.10.1 Normal Operations 90
3.10.2 Dealing with Problems 91
3.11 Example 91
3.12 Experience 96
3.12.1 Particular Strengths of the System 96
3.12.2 Problems and Solutions 97

3.12.3 Re-evaluation of Past Decisions and Possible Future Improvements . . . 98
3.13 Summary . . . 99

4 A Measurement of the Mean B-Hadron Lifetime 101
4.1 Overview of Method . . . 101
4.2 Analysis Program . . . 102
4.2.1 Event Selection . . . 105
4.2.2 Muon Identification . . . 106
4.2.3 Initial J/ψ Candidate Selection . . . 108
4.2.4 Vertex Reconstruction . . . 109
4.2.5 Intermediate Candidate Parameters . . . 111
4.3 J/ψ Candidate Selection . . . 116
4.4 Fit Techniques . . . 117
4.4.1 Fit Result Representation . . . 122
4.4.2 Backgroundless Decay Time Fit . . . 126
4.4.3 Mass Distribution Parameterization . . . 127
4.5 B-Hadron Decay Times . . . 129
4.6 Sample Composition . . . 132
4.7 Lifetime Fit . . . 133
4.7.1 Fit Results . . . 136
4.7.2 Fit to Monte Carlo Data . . . 140
4.8 Systematic Errors . . . 140
4.9 Results and Interpretation . . . 144

A The DELPHI Collaboration 147

B Track Parameterization 151

C G64 crates and Elementary Processes 155

D Fitting Methods 163
D.1 Unbinned Extended Maximum Likelihood Fit . . . 163
D.2 Unbinned Maximum Likelihood Fit . . . 164
D.3 Binned Maximum Likelihood Fit . . . 164
D.4 Binned χ^2 Fit . . . 166

References 169

List of Tables

2.1 Integrated luminosity and total number of hadronic Z^0 events recorded by DELPHI. . . . 17
2.2 Characteristics of the DELPHI tracking and particle identification detectors. . . . 21
2.3 Characteristics of the DELPHI calorimeters. . . . 31
2.4 Muon identification efficiencies and misidentification probabilities for the four MUFLAG tags. . . . 49

3.1 The gases used by each DELPHI detector partition. . . . 55
3.2 Summary of the G64 crates and Elementary Processes used by each detector partition. . . . 63
3.3 SMI states and commands of the Elementary Process. . . . 82
3.4 SMI states and commands of a typical detector partition. . . . 83

4.1 Initial J/ψ candidate selection statistics. . . . 104
4.2 Fit function terms after convolution. . . . 128
4.3 Definition of lifetime fit fractions. . . . 135
4.4 Monte Carlo fit results 141
4.5 Summary of systematic errors. . . . 144
4.6 Summary of different B lifetime measurements 145

C.1 G64 crates and Elementary Processes used by each detector partition. 155

List of Figures

1.1 Mechanism for the decay B → J/ψK. 10
1.2 Feynman diagrams for various prompt J/ψ production mechanisms . 11

2.1 Location of the LEP collider at CERN. 14
2.2 The LEP injector complex. 15
2.3 Photograph of the DELPHI experimental hall. 17
2.4 Schematic layout of DELPHI. 18
2.5 Schematic layout of the 1994 Vertex Detector. 22
2.6 Cross section of a Vertex Detector double-sided plaquette. 23
2.7 Vertex Detector intrinsic hit resolutions. 26
2.8 Track impact parameter errors as a function of momentum. 27
2.9 Schematic layout the the TPC. 28
2.10 A Barrel Muon Chamber sector. 33
2.11 Cross-section through a Barrel Muon Chamber. 33
2.12 Cross-section through a Forward Muon Chamber. 35
2.13 Assumed variation of energy loss with momentum. 44
2.14 Inverse momentum distribution of 45.6 GeV/c muons. 46
2.15 Track momentum precisions from simulated data. 46
2.16 Identification efficiency of standard muon tag. 49

3.1 Diagram of the overall structure of DELPHI Slow Controls system. . . 52
3.2 Photograph of MAC–G64 and CAEN crates. 64
3.3 A typical screen from the HIPE Expert Display. 75
3.4 A typical screen from the EMU Display. 78
3.5 A typical screen from the SMI display. 84

4.1 Distribution of parameters used in the hadronic event selection. . . . 107
4.2 Reconstructed masses of all J/ψ candidates passing the initial cuts. . 110
4.3 $\mu\mu$ opening angle for all J/ψ candidates passing the initial cuts. . . . 110
4.4 Variation in the sample composition with reconstructed momentum . 116
4.5 Fit to the reconstructed masses of J/ψ candidates 118
4.6 Display of a candidate J/ψ event. 119
4.7 Vertex Detector views of a candidate J/ψ event. 120
4.8 Mass and decay time reconstruction errors 124
4.9 Comparison of mass fit representations 125
4.10 Comparison of lifetime fit representations 125
4.11 Monte Carlo correction for B decay time uncertainty. 131
4.12 Opposite-sign sample composition 132
4.13 Lifetime distribution for like-sign candidates in the sideband 137

4.14 Lifetime distribution for opposite-sign candidates in the sideband . . 138
4.15 Lifetime distribution for opposite-sign candidates in the signal window 139

B.1 Illustration of the track impact parameter. 153

Introduction

This thesis describes work carried out on the DELPHI detector at the LEP e^+e^- collider at CERN near Geneva in Switzerland. Until the autumn of 1995, LEP operated at centre-of-mass energies close to the Z^0 pole. This has provided many rich fields of study: probing the properties of the Z^0 itself, searching for new particles among its decays, and making use of the large cross-section as a factory for the production of other particles for study in a relatively clean environment compared to hadron machines.

DELPHI is a general purpose detector with particular strengths in the fields of particle identification and the precise measurement of particle decays close to the collision point. It is no coincidence that these are both especially important for the study of B-hadrons, which have been an active area of research at LEP, and are central to the analysis presented in chapter 4.

I first worked on the DELPHI detector as a summer student at the Rutherford Appleton Laboratory (RAL) in 1984, when I made some first Monte Carlo studies of the proposed Vertex Detector. Since 1986, when I took up a position at RAL as a Physicist–Programmer, I have been responsible for much of the DELPHI Slow Controls system: specifically the Elementary Process (described in section 3.5.1) and a first version of HIPE (section 3.5.2). I have also collaborated on the VAX–G64 communications (section 3.3.2) and EMU (section 3.6) systems, as well as the overall design of the Slow Controls system. In 1994 I wrote a description of this system for publication [82]. Chapter 3 is based on this paper, though considerably expanded.

After DELPHI started running in 1989/90, I started the DPhil for which this thesis

is submitted. As well as continuing work on the Slow Controls (much of the final system came into operation during this period), I was also involved in the initial design and implementation of the Vertex Detector event viewing [27] and the analysis package, VDCLAP (section 2.3.1). My main field of analysis has been on J/ψ production in DELPHI, and this is described in chapter 4. The early stages of this work involved studies of the DELPHI track reconstruction (section 2.11.2) quality.

Much of the J/ψ studies presented later have been performed in close collaboration with Paula Collins. While I created the basic analysis program framework (described in section 4.2) and our post-ntuple analyses and fits were largely independent, Paula contributed significantly to the development of the analysis program in many areas of additional study detailed in [1]. She also developed code for extracting and interpreting Monte Carlo truth information, of which I have made extensive use.

This thesis is organized as follows.

Chapter 1 presents a brief outline of the current understanding of J/ψ production at LEP. Further details may be obtained from the references given.

Chapter 2 describes the DELPHI detector, its Data Acquisition system, and those aspects of the event analysis chain that are common to a variety of studies.

Chapter 3 gives a detailed account of the DELPHI Slow Controls system, concentrating on the system in operation from 1993–5. In previous years the system was still under development. Subsequent years saw running above the W^+W^- threshold, as well as the replacement in 1997 of the VAX computers with Alpha (AXP) systems (still running the VMS operating system), and the initial deployment of G64-based 68020 processors as a replacement for some of the more heavily loaded 6809 processors.

Chapter 4 details a study of J/ψ production at LEP. J/ψs are used as a tag of B-hadron decay positions, allowing for a measurement of a mean B-hadron lifetime. The number of J/ψs produced at the e^+e^- collision point is also obtained.

Acknowledgements

I am extremely grateful to the many people who have helped me in the study for and preparation of this thesis.

My supervisor, Gerald Myatt, has always been extremely helpful and has been particularly understanding about receiving last-minute text to read over the past few weeks.

For many valuable encouragements and discussions on my analysis, I am indebted to my colleagues at RAL, especially Robert Sekulin, who has also been an indefatigable advisor, proof-reader, and cheer-leader in-chief; Bill Murray, for his advice on so many occasions (and for getting me out of a hole late one Sunday evening); and Wilbur Venus and George Kalmus, for their support.

I am also grateful to Fabienne Ledroit, Oleg Kuznetsov, and other members of Team 11, Subgroup 4, for enlightenment on all matters J/ψ.

Primarily, though, I must thank Paula Collins, my erstwhile collaborator. She was a tremendous help in many areas, but more importantly she showed me that it was possible (even though that was supposed to be my job).

The DELPHI Slow Controls system would have been no more than a glint in Ugo's eye, had it not been for the sterling and often heroic work of my colleagues in the Slow Controls group: André Augustinus, Robert Sekulin, and Gareth Smith. I would also like to thank my former co-workers Mark Dönszelmann, Tiziano Rovelli, Peter Lorenz, Ignacio Martinez, Angel Camacho, Karsten Spang, Flavio Fontanelli, Gian Gopal, Michel Jonker, and John Barlow, who played a major rôle in various aspects of the design and initial implementation of the system.

For their help in testing the system (often to destruction) and providing me with many useful suggestions, I would like to thank many of my colleagues in the DELPHI Collaboration, particularly the various detector partitions' Slow Controls 'responsibles'. I also acknowledge with thanks the support I have received from the members of the DELPHI DAS group, in particular Yura Belokopytov, Boda Franek, and Frank Harris.

I am also grateful for the high quality of support from many people in ECP, CN, and SL divisions at CERN. For their vision and its realization, as well as much useful collaboration in my own areas of endeavour, I would particularly like to thank Tim Berners-Lee and Paul Burkimsher.

I want to thank all my contemporaries in the Oxford DELPHI group for making my (many!) years in Oxford and Geneva as enjoyable as they were: DPhil students Andrew Pinsent, Nigel Crosland, Christine (snow babe) Beeston, Martin (snake-charmer extraordinaire) Bates, Guy (2 m) Wilkinson (though still not forgiven for the Wall of Utter Death), Simon (Cliffy) Hodgson, Paula (top psiwanger and gossipmeisterin) Collins, Simon Blyth, Rashid Zuberi (who throws a mean wed-

ding bash), Steve Bosworth, John Holt, Ainsley (chocolate heaven) Normand, Kin Yip, Chris Parkes, Julie Thomas, Jim Libby, Geoff Morton, and Juan Palacios. Postdocs Paul ("they are all bastards") Dauncey (who suggested looking at J/ψs in the first place), Gary (francophone) Barker, and Lino Demaria.

Also, thanks to John Grandidge for casting a professional eye over this tome, Urs Wielgosz for valuable thesis submission advice, and everyone associated with the OU SF Group for keeping me from becoming too sane.

I am very grateful to Robin Devenish and Roger Barlow for sparing the time to read and examine this thesis.

Finally, I acknowledge the many organisations who have supported my work on this thesis and, albeit indirectly, my DPhil studies: the Science and Engineering Research Council, the Particle Physics and Astronomy Research Council, the Rutherford Appleton Laboratory, the Daresbury and Rutherford Appleton Laboratories, and the Council for the Central Laboratory of the Research Councils.

This thesis is dedicated to JACHEN, without whom it would of course have been impossible.

Oxford, April 1998

List of Common Abbreviations

ADC		analog-to-digital converter
ALEPH	[13]	detector situated at collision point 4 of the LEP collider
ASCII		American Standard Code for Information Interchange (basic 7-bit character set)
AST	[114]	Asynchronous System Trap (VMS process-context interrupt)
BCO	§2.10	LEP beam cross-over
CAEN	§3.3.1	a commercial high voltage unit
CARGO	§3.7	the DELPHI database system
CATS	§3.3.2	Common Access to Transport Service (communications protocols interface)
CERN		European Laboratory for Particle Physics
CMS		centre of mass system
CPU		Central Processing Unit
DAS	§2.10	Data Acquisition system (AKA DAQ)
DELANA	§2.11.1	DELPHI analysis program
DELPHI	§2.2	detector situated at collision point 8 of the LEP collider
DELSIM	§2.12	DELPHI simulation program
DIM	§3.8	DELPHI Information Management communications system
DMA		direct memory access, allowing a peripheral to access memory without intervention by the CPU
DST	§2.11.1	post-DELANA data storage format
DSTANA	§2.11.1	post-DELANA analysis library
DSTFIX	§2.11.1	post-DELANA event processing
DUI	§3.8.2	DELPHI (graphical) User Interface
EMF	§§2.5.2,3.2.6	Forward Electromagnetic Calorimeter
EMU	§3.6	Error Message Utility
EP	§3.5.1	Elementary Process
EPROM		Erasable Programmable Read Only Memory
FB	§2.10	Fastbus

FCA	§§2.3.5,3.2.4	Forward (tracking) Chambers A
FCB	§§2.3.6,3.2.4	Forward (tracking) Chambers B
FLEX	§3.3.2	the G64 Operating System
G64	§3.3	microprocessor bus or the microcomputer based on it
GSS	§3.9.2	General Surveillance System
HAC	§§2.5.3,3.2.6	Hadron Calorimeter
HIPE	§3.5.2	expert interface to the Elementary Process
HOF	§§2.7,3.2.8	Forward Hodoscope
HPC	§§2.5.1,3.2.6	High-density Projection Chamber (barrel electromagnetic calorimeter)
HV		high voltage
ID	§§2.3.2,3.2.3	Inner (tracking) Detector
IEEE		Institute of Electrical and Electronics Engineers
JETSET	§2.12	Lund e^+e^- Monte Carlo generator with jet fragmentation
L3	[15]	detector situated at collision point 2 of the LEP collider
LED		Light-Emitting Diode
LEP	§2.1	Large Electron–Positron collider
LV		low voltage
MAC	§3.3.1	double-height crate containing G64 and input/output cards
MC		Monte Carlo simulation
MHI	[121]	Model Human Interface package
MINUIT	[148]	function minimization and error analysis package
MUB	§§2.6.1,3.2.7	Barrel Muon Chambers
MUC	§2.6	Muon Chambers (barrel, forward, and surround)
MUF	§§2.6.2,3.2.7	Forward Muon Chambers
MUS	§§2.6.3,3.2.7	Surround Muon Chambers
MWPC		multiwire proportional chambers
NDF		number of degrees of freedom
NMR		nuclear magnetic resonance
OD	§§2.3.4,3.2.3	Outer (tracking) Detector
OPAL	[16]	detector situated at collision point 6 of the LEP collider
OSI	§3.3.2	Open Systems Interconnect network protocols (ISO standard)
PAW	[145]	Physics Analysis Workstation data manipulation and presentation program
PIA	§3.3.1	Parallel Input Adapter
QED		Quantum Electrodynamics

RAL		Rutherford Appleton Laboratory
RAM		random-access (read/write) memory
RIB	§3.2.5	Barrel RICH
RICH	§§2.4,3.2.5	Ring Imaging Cherenkov Counters
RIF	§3.2.5	Forward RICH
RMS		root mean square
ROM		read-only memory
RPC	§3.3.2	Remote Procedure Call
SAT	§§2.8.1,3.2.9	Small Angle Tagger luminosity monitor
SCI	§§2.7,3.2.8	Scintillator Trigger Counters
SC	chapter 3	Slow Controls
SLIMOS	§3.10	shift leader in matters of safety
SMI	§3.8	State Management Interface
S/N		signal to noise ratio
SPS	§2.1	Super Proton Synchrotron
STIC	§§2.8.2,3.2.9	Small Angle Tile Calorimeter luminosity monitor
TANAGRA	§2.11.1	data storage format used in DELANA
TCP/IP		Transmission Control Protocol over Internet Protocol (Internet standard)
TD	§2.11.1	digitization TANAGRA bank
TE	§2.11.1	track element TANAGRA bank
TK	§2.11.1	reconstructed track TANAGRA bank
TLA		three-letter acronym
TMAE	§3.2.5	a photo-ionizing vapour
TOF	§§2.7,3.2.8	Time of Flight counters
TPC	§§2.3.3,3.2.3	Time Projection Chamber
VAX	§3.4	computers used in the online for high-level control
VD	§§2.3.1,3.2.3	Vertex Detector
VDCLAP	§2.3.1	VD analysis library
VMS	§3.4.2	the VAX operating system
VSAT	§§2.8.3,3.2.9	Very Small Angle Tagger luminosity monitor
VT100		text-based computer terminal

Chapter 1

J/ψ Production from the Z^0

J/ψ meson production from Z^0 decays can be described by two classes of mechanism. The dominant one is via the weak decay of B-hadrons[1]

$$Z \to b\bar{b}, b \to J/\psi X. \tag{1.1}$$

with the J/ψ produced in association with other hadrons, X, produced both in the hadronization of the b quark and the subsequent decay of the B-hadron.

In common with other B decay modes, the large Z^0 mass (91 GeV/c^2, compared to B-hadron masses of 5.3–5.6 GeV/c^2) provides the B-hadrons with a large boost ($\sim$ 6.1, with average momentum $\sim$ 32 GeV/c) which, coupled with their relatively long lifetime ($\sim$ 1.6 ps), gives an average decay distance of around 2.9 mm at LEP. Such distances are measurable using vertex detectors, such as the one pioneered by DELPHI and described in section 2.3.1. This is exploited in the analysis described in chapter 4.

In the spectator model, the B-hadron decay is dominated by the b-quark, for example as shown in figure 1.1. Although the spectator model fails dramatically in the charm sector, as evidenced by different lifetimes for different species (e.g. $\tau_{D^+} = (1.057 \pm 0.015)$ ps but $\tau_{\Omega_c^0} = (0.064 \pm 0.020)$ ps [2]), the heavier b-quark

[1] In other words, the decay of naked beauty to hidden charm.

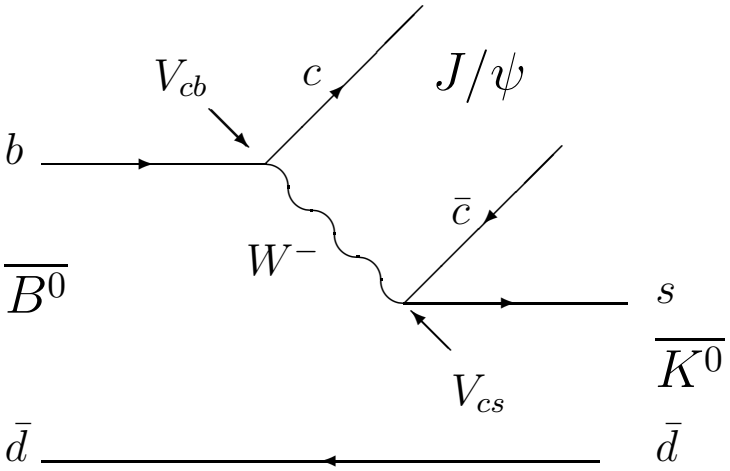

Figure 1.1: Mechanism for the decay B $\rightarrow$ J/ψK.

mass should produce much smaller differences, though there is still considerable theoretical uncertainty as to how much smaller [3, 4]. Experimentally [5], there seem to be no significant differences between the $B^{\pm}$, B^0, and B_s meson lifetimes, but a shorter B-baryon lifetime is seen ($\tau_{\Lambda_B}/\tau_{B^0} = 0.78 \pm 0.05$), though not yet understood theoretically.

Many experimental determinations of B-hadron lifetimes, including the one described in chapter 4, do not distinguish the different species, and so measure a mean. Given the different B lifetimes, slightly different values may be obtained depending upon the composition of the B-hadron source and (for exclusive and semi-inclusive studies) the branching fractions to the selected final states.

More details on the mean B lifetime and J/ψ production from B decays can be found in [1, chapter 1]

Other production mechanisms produce the J/ψ promptly at the e^+e^- collision point (see figure 1.2). The most significant processes are

Charm fragmentation: The primary reaction is $Z^0 \rightarrow c\bar{c}$. One c-quark emits a gluon, which splits into another $c\bar{c}$ pair. If the secondary $\bar{c}$-quark is of opposite colour and approximately collinear to the primary c-quark, then a charmonium state can be formed. The branching fraction for this process is predicted [7] to be

$$\mathrm{Br}(Z^0 \rightarrow c\bar{c} + \text{prompt J}/\psi) = 0.8 \times 10^{-4} \qquad (1.2)$$

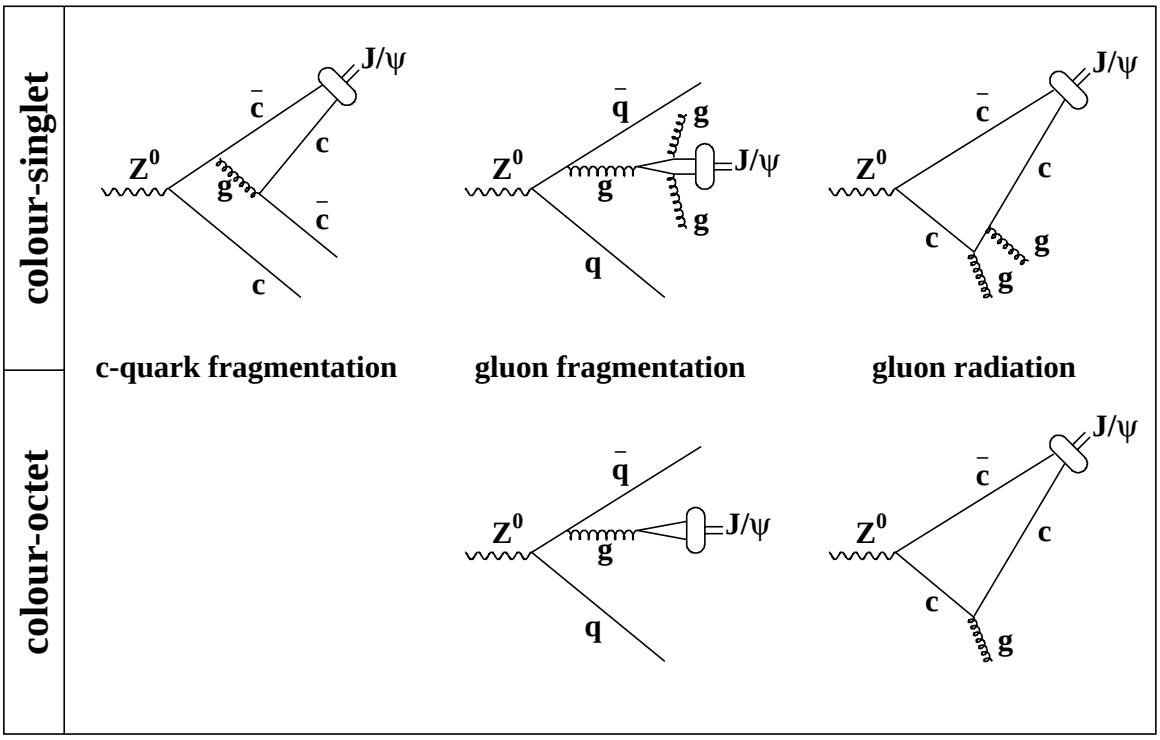

Figure 1.2: Feynman diagrams for various prompt J/ψ production mechanisms [6].

Gluon fragmentation: In this case a virtual gluon emitted from one of the quarks in a $Z^0 \to q\bar{q}$ decay forms a charmonium state. Originally this process was expected to have had a much smaller branching fraction [8] than that of charm fragmentation because only the 'colour singlet' mode was considered. This requires the $c\bar{c}$ quarks to be mutually colourless to form a J/ψ. However more recent models, where the J/ψ is formed via a 'colour octet' state which evolves into the singlet state with the emission of soft gluons, give larger expected branching fractions

$$\mathrm{Br}(Z^0 \to q\bar{q}+g^* \to \text{prompt J}/\psi) = 1.9\times10^{-4}\ [7]^2 \quad \text{and} \quad 1.5\times10^{-4}\ [11] \quad (1.3)$$

though with a factor of ~ 2 uncertainty. In principle, the colour octet mode also contributes to charm fragmentation, but is expected to be negligible.

In both cases the branching ratio predictions are based on fits [9, 10] to J/ψ

[2]Reference [7] quotes a branching ratio of 3.3×10^{-4}, which is based on an amplitude calculated in [9]. Using their updated amplitude from [10] gives 1.9×10^{-4}.

transverse momentum distributions measured at CDF [12].

The large Z^0 hadronic cross section ($\sim$ 30 nb) and LEP luminosities (139 pb^{-1} integrated luminosity at the Z^0 recorded by DELPHI in 1992–5) mean that, despite the small branching fraction [2, page 218]

$$\mathrm{Br}(Z^0 \to J/\psi X) = (0.380 \pm 0.027)\% \,, \tag{1.4}$$

a reasonable number of J/ψs are produced. The decay mode $J/\psi \to \mu^+\mu^-$, which accounts for $(6.02 \pm 0.19)\%$ [2, page 532] of J/ψ decays allows a particularly clean J/ψ selection.

Chapter 2

The DELPHI Detector

The DELPHI[1] detector is one of four [13, 14, 15, 16] installed around the LEP[2] electron–positron collider at CERN.[3] For its first seven years LEP operated at around 91 GeV centre-of-mass energy (the Z^0 resonance). At the end of 1995 it made a brief foray to 136 GeV. From July 1996 it has been mostly been running above the W^+W^- threshold, initially at 161 GeV. In this thesis I describe the detector configuration and experimental results from the period of Z^0 running.

DELPHI is designed as a general purpose detector with special emphasis on particle identification (using the Ring Imaging Cherenkov (RICH) detector) and precise measurement of particle decays close to the collision point (using the silicon Vertex Detector (VD)).

2.1 The LEP Machine

As shown in figure 2.1, LEP is located on the Swiss–French border near Geneva. It is roughly circular (actually eight straight sections on either side of each cavern, interspersed with curved sections), 26.7 km in circumference and between 50 and

[1] ***De****tector with* ***L****epton, Photon, and* ***H****adron* ***I****dentification*, ©Gerald Myatt. The members of the DELPHI Collaboration are listed in appendix A.

[2] ***L****arge* ***E****lectron–****P****ositron* collider

[3] *European Laboratory for Particle Physics.* The acronym, 'CERN', is from its original title, ***C****onseil* ***E****uropéen pour la* ***R****echerche* ***N****ucléaire.*

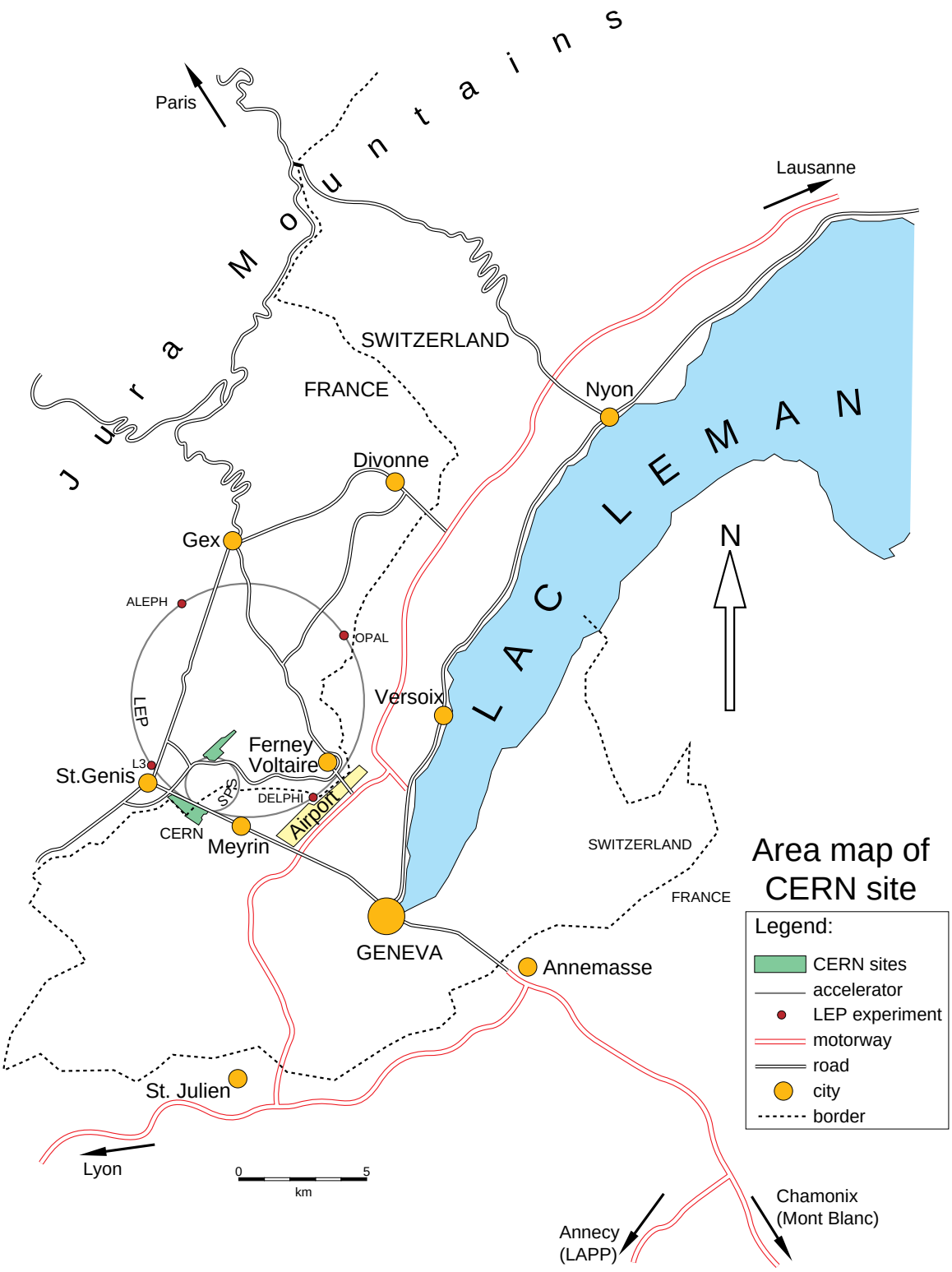

Figure 2.1: Location of the LEP collider at CERN. The positions of the four experiments (DELPHI, OPAL, ALEPH, and L3) and the SPS accelerator are also shown.

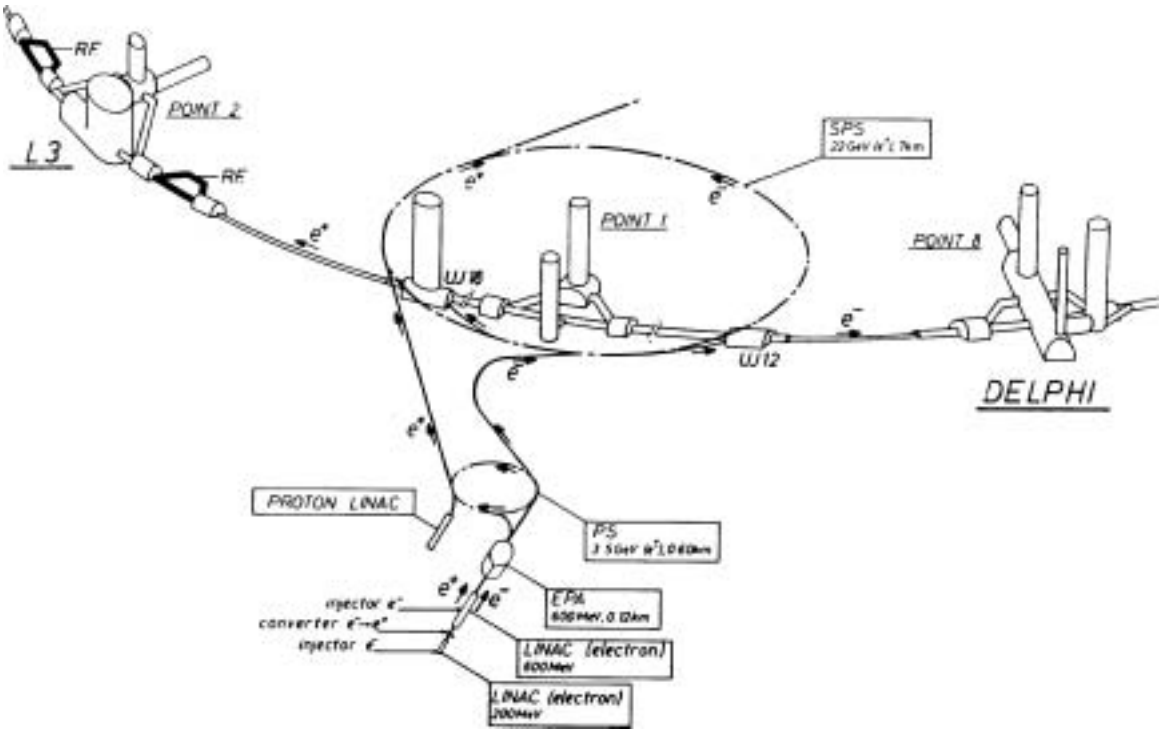

Figure 2.2: The LEP injector complex. The two closest detector caverns on the LEP beamline (DELPHI and L3) are also shown.

170 m below ground level.

The injector system, which starts at the main CERN site, is shown in figure 2.2. The LEP Injector Linacs (LIL) produce electrons and positrons (the positrons from the collision of 200 MeV electrons with a tungsten converter), which are separately accelerated to 600 MeV. After storage in the Electron–Positron Accumulator (EPA), they are injected into the Proton Synchrotron (PS) and thence into the Super Proton Synchrotron (SPS); these accelerate the particles to 3.5 and 20 GeV respectively. After injection into LEP, the counter-rotating electrons and positrons are accelerated to 45 GeV using a radio frequency (RF) acceleration system powered by sixteen 1 MW klystrons, operating in two of the straight sections of the ring. The beams are bent into orbit by 3368 dipole magnets and focused with 808 quadrupole and 504 sextupole magnets. Superconducting quadrupoles provide additional focusing around the four interaction regions, where the beams are squeezed to a RMS width of about $(200 \times 5)\ \mu\text{m}^2$ (horizontal $\times$ vertical).

The expected event rate is

$$N = \int \sigma \mathcal{L}(t) \mathrm{d}t \,, \tag{2.1}$$

where σ is the cross-section for the process in question (~ 30 nb for $\mathrm{e^+e^-} \to \mathrm{Z^0} \to \mathrm{q\bar{q}}$ at the $\mathrm{Z^0}$ peak[4]). In LEP, the luminosity, $\mathcal{L}$, defined by equation 2.1, is approximately

$$\mathcal{L} = \frac{n_b f N_{e^-} N_{e^+}}{4\pi\sigma_x\sigma_y} \tag{2.2}$$

The n_b bunches in each beam circulate round the ring with a frequency f. Each bunch contains N_{e^-} electrons or N_{e^+} positrons and has RMS dimensions $\sigma_x \times \sigma_y$ (given above) at the interaction point. Typical 1994 values $n_b = 8$ and $f = 11.2$ kHz (corresponding to a beam cross-over rate of 11 μs), with $N_{e^+} = N_{e^-} = 1.7 \times 10^{11}$ give a luminosity, $\mathcal{L}$, of 2.1×10^{31} $\mathrm{cm^{-2}s^{-1}}$.

The LEP design and commissioning is described in [17], while its subsequent operation and performance is summarized in [18]. As well as higher currents and better operational efficiency, the luminosity was improved using the Pretzel [19] and bunch train [20] schemes, which increased the number of bunches of electrons + positrons in the machine from $4 + 4$ (1989–92) to $8 + 8$ (1992–4), and thence to $12 + 12$ (1995). Table 2.1 summarizes the luminosity and number of events observed by DELPHI.

2.2 Detector Overview

The detector and its front-end electronics are situated 100 m underground in the experimental cavern (see figure 2.3). The layout of DELPHI is illustrated in figure 2.4.

The detector has a cylindrical geometry consisting of successive layers of charged tracking detectors (Vertex Detector, Inner Detector, Time Projection Chamber (TPC), and outside the Cherenkov detector (Barrel RICH), the Outer Detector at a radius of 2 m), followed by electromagnetic and hadron calorimetry (provided respectively

[4] 1 nb $= 10^{-33}$ $\mathrm{cm^2}$

Year	$\int \mathcal{L} dt$ (pb^{-1})	$N_{had}/10^3$
1989	0.7	13
1990	5.8	125
1991	17.2	275
1992	24.1	751
1993	36.3	755
1994	46.3	1484
1995	31.7	750
Total	162.1	4153

Table 2.1: Integrated luminosity and total number of hadronic Z^0 events [23] recorded by DELPHI in the period 1989–95. N_{had} is higher in 1992 and 1994 relative to the integrated luminosity because during the other years a significant amount of data was taken off-peak, where the cross-section is much lower.

Figure 2.3: The DELPHI experimental hall. This view shows the counting houses, which are in front of the detector itself.

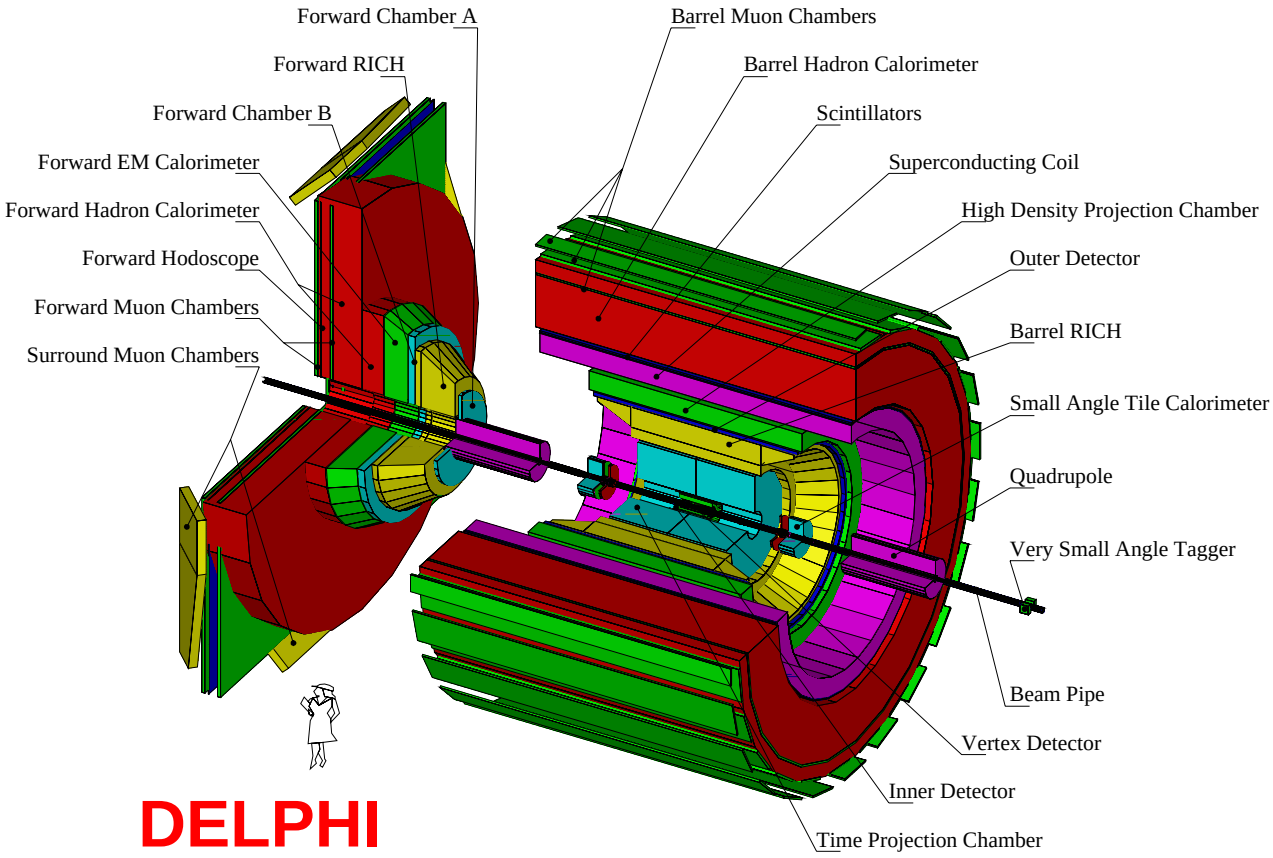

Figure 2.4: Schematic layout of the 1994–5 DELPHI detector, showing a cutaway view of the barrel and the $-z$ endcap, and a 'standard woman' for scale. Note that the Forward Chambers A are actually fixed to the Time Projection Chamber, but shown here on the front of the endcap for clarity.

by the High-density Projection Chamber and instrumented magnet yoke), and finally muon chambers (at 5 m radius). There is a similar arrangement in the endcaps (forward tracking chambers, RICH, electromagnetic and hadron calorimetry, and muon chambers at 5 m on either side of the interaction point). Additional scintillators and muon chambers between barrel and endcaps, and low-angle calorimeters (mainly for measuring Bhabhas) aim to provide near-4π solid-angle coverage. The tracking chambers use a solenoidal magnetic field of 1.2 tesla, provided by a superconducting electromagnet just inside the hadron calorimeter.

The primary coordinate scheme [21] used by the DELPHI collaboration has the z-axis along the electron beam direction (parallel to the detector's central magnetic field), horizontal x-axis pointing towards the centre of LEP, and vertical y-axis pointing upwards, so that (x, y, z) make a right-handed Cartesian system. Given the cylindrical symmetry of the detector (and the processes it measures) it is often more convenient to use a cylindrical or spherical coordinate system with radial and polar coordinates, R and θ, giving respectively the perpendicular distance and the angle from the z-axis. The azimuthal coordinate, ϕ, gives the angle from the x-axis in the xy projection. Due to DELPHI's symmetry about the xy plane, quoted polar angles $\theta < 90^\circ$ will imply also the reflection in the xy plane $(180^\circ - \theta)$, unless otherwise stated.

Tables 2.2 and 2.3 summarize the characteristics of the main detector components described in the following sections. Particular attention is paid to the Vertex Detector and Muon Chambers which play an important rôle in the analysis presented in chapter 4. More details of the detector design may be found in [22, 14] and references given below. A review of the performance of DELPHI in its first six years of operation is given in [23]. The Slow Controls of each detector component are described in section 3.2, with table 3.1 listing the gas mixtures used.

2.3 Tracking Detectors

The trajectory of charged particles may be determined by their ionizing effects on the material they pass through. The track curvature in a magnetic field can be used to determine a particle's momentum (and charge), which in DELPHI's central uniform 1.2 T field is given in GeV/c by $p = 0.0036\rho/\sin\theta$, where ρ is the radius of curvature in cm.

Tracking of charged particles in the barrel is provided by the Inner Detector (ID), TPC, and Outer Detector (OD). The forward chambers (FCA and FCB) are used in the endcaps. All these detectors use gases as ionizing media. Additional extremely precise measurements are made close to the interaction point by the silicon Vertex Detector (VD). See table 2.2 for a comparison of these detectors' specifications.

2.3.1 Vertex Detector (VD)

A recognition of the importance of precise measurements close to the interaction region to identify and reconstruct short-lived particles, particularly given the emphasis on particle identification prompted by the RICHes, led to the inclusion of a high-precision silicon Vertex Detector in the design of DELPHI.

Geometry

After initial tests during the pilot run of 1989, two layers of single-sided detectors (measuring only the azimuthal coordinate) at 9 and 11 cm radii (designated **inner** and **outer** respectively) were installed in 1990. This was the first use of this technology in a collider [24].

In 1991 an additional (**closer**) layer was added at 6.3 cm, when experience with LEP operation allowed a reduction of the beampipe radius from 7.9 to 5.6 cm. The new beampipe is composed of beryllium, rather than aluminium to reduce multiple scattering.

For the 1994 run, the closer and outer layers were replaced with double-sided

Detector	Coordinate	Geometric Acceptance			measurements per track per coord.	Resolution per point (σ) [mm]
		R [cm]	$\|z\|$ [cm]	θ [deg] ($+z$)		
VD (1990)	$R\phi$	$9, 11$	≤ 12	≥ 37	2	0.008
VD (1991–3)	$R\phi$	$6.3, 9, 11$	≤ 12	≥ 28	3	0.008
VD (1994–5)	$R\phi$	$6.3, 9, 11$	≤ 14	≥ 25	3	0.008
	z				2	0.009($\perp$)–0.040
ID (–1994)	$R\phi$	11.8–22.3	≤ 40	≥ 17	24	0.075–0.125
trigger layers	z	23–28	≤ 50	≥ 30	5	0.5($\perp$)–1
ID (1995–)	$R\phi$	11.8–22.3	≤ 62	≥ 10	24	0.085
straw tubes	$R\phi$	25–30	≤ 105	≥ 15	5	2.4
TPC	$R\phi$	35–111	≤ 134	≥ 20	16	0.25
	z				16	0.88
	$\mathrm{d}E/\mathrm{d}x$				192	6.2% total
RIB liquid	θ_c	124–148	≤ 155	≥ 40	~ 14	13.3 mrad
RIB gas	θ_c	148–196	≤ 177	≥ 40	~ 8	4.3 mrad
OD	$R\phi$	197–206	≤ 232	≥ 42	5	0.11
	z				3	35
MUB	$R\phi$	$445, 479, 532$	≤ 385	≥ 52	2–6	1
	z					10
FCA	x, u, v	30–103	155–165	11–32	2	.3
RIF liquid	θ_c	450–125	172–185	16–35	~ 7	11.4 mrad
RIF gas	θ_c	450–180	206–266	12–35	~ 8	2.5 mrad
FCB	x, u, v	53–195	267–283	11–36	4	.3
MUF	x, y	70–460	$463, 500$	9–43	$2 + 2$	$1 + 2$
MUS	ϕ, θ	480–655	410–575	42–52	2	10,25

Table 2.2: Some characteristics of the DELPHI tracking and particle identification detectors: Vertex Detector (VD), Inner Detector (ID), TPC, Outer Detector (OD), Forward Chambers A and B (FCA and FCB respectively), Barrel and Forward RICHes (RIB and RIF), and Barrel, Forward, and Surround Muon Chambers (MUB, MUF, and MUS).

detectors [25], which are capable of measuring both the azimuthal and longitudinal coordinates. The inner layer remained of the old design (and in fact used modules scavenged from the inner and outer layers of the previous detector).

The geometry of the 1994 detector is shown in figure 2.5. Each shell consists of 24 modules with a 10–20% overlap in ϕ between modules. The 12 modules in the three layers on each side ($+x$ and $-x$) are assembled into two half-shells, which are independently installed into DELPHI. Each module consists of 4 silicon detectors (**plaquettes**), bonded together end-to-end for a total length of 24 cm for the inner and outer layers, and 22 cm (1991–3) / 28 cm (1994–5) for the closer layer.

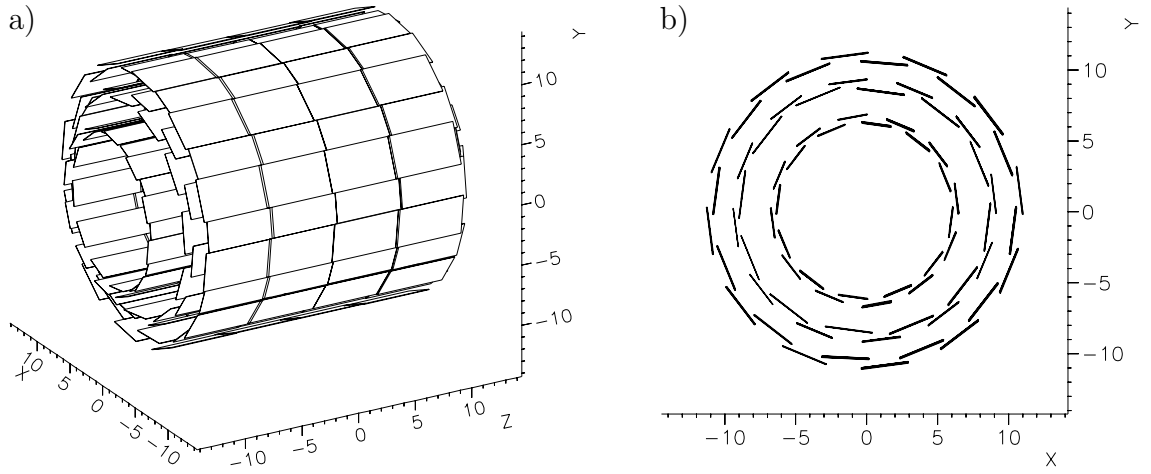

Figure 2.5: Schematic layout of the 1994 Vertex Detector in a) perspective and b) $R\phi$ views. The scale is in cm. The geometry of the 1991–3 detector was similar, except that it did not have the longer innermost layer, and the modules of the outer two layers had a 'paddle wheel' arrangement.

Detectors

The single-sided detector plaquettes consist of 285 μm-thick phosphorous-doped n-type silicon with 7 μm-wide boron-doped p^+ strips parallel to the z-axis spaced at intervals of 25 μm. By applying a reverse bias of $\sim$ 60 V to these diodes, the n-type silicon is depleted of charge carriers. The passage of a charged particle through the detector liberates electron–hole pairs. The holes drift to the diodes where the deposited charge is detected.

Every other diode (i.e. at 50 μm intervals) is read out via capacitive coupling: the aluminium readout strip is separated from the p^+ silicon by a 0.23 μm layer of silicon dioxide insulator. Capacitive coupling, rather than direct charge readout, is used to reduce the leakage current and hence detector noise. Each unconnected strip is capacitively coupled to the readout strips on either side of it. This causes the deposited charge to be distributed over several readout strips (most often two), allowing the position measurement to be improved over simple strip enumeration by using the relative charge deposits on each strip.

As shown in figure 2.6, the double-sided detector has n^+ strips running across its other side, allowing the z-coordinate to be measured by picking up the electron signal. A layer of metal readout lines, orthogonal to those running along the n^+ strips, allows

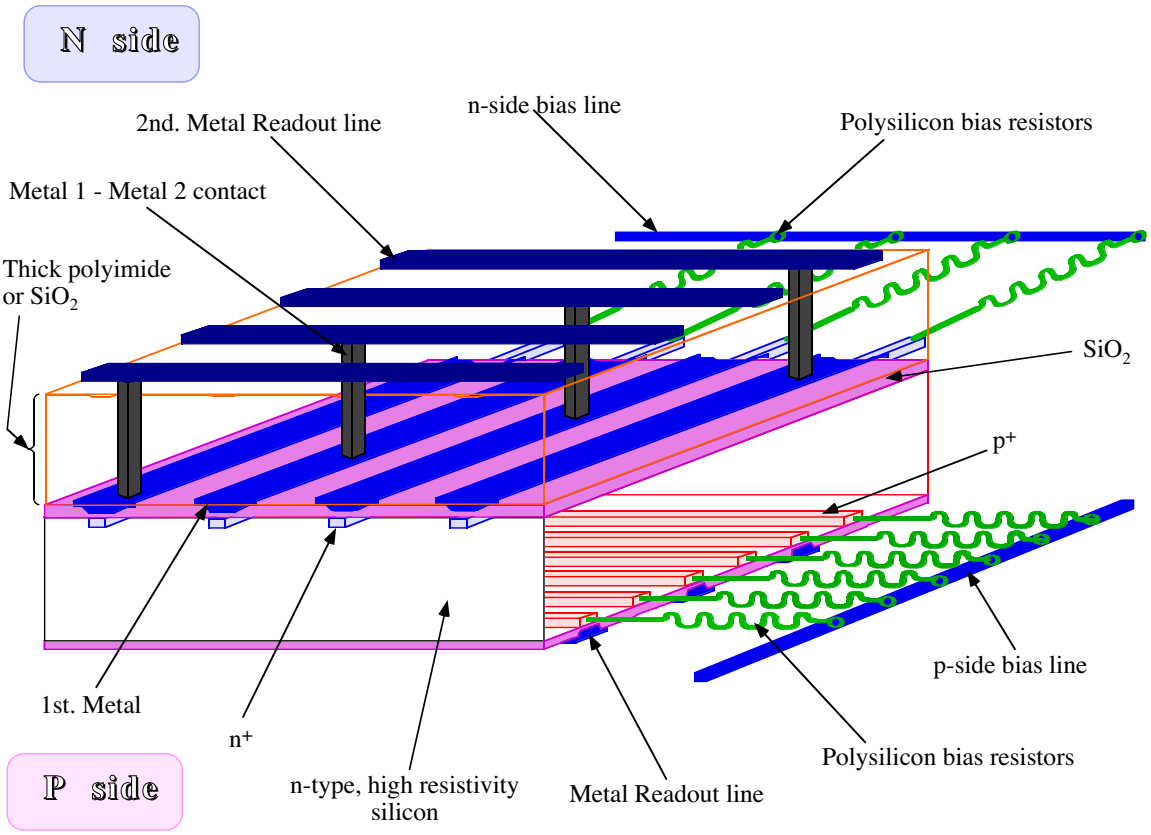

Figure 2.6: Cross section of a Vertex Detector double-sided plaquette.

the signals from the n-side to be read out at the end of the detector.

In order to improve the signal-to-noise (S/N) ratio in z, the n^+ strip pitch is increased at the ends of the module, where the larger incidence angle of the tracks spreads the charge over a larger area. The two plaquettes on each side of a module are bonded such that the n-side of one is joined to the p-side of the other, further improving the (S/N) of the z-measurement. The opposite polarities of signals from the two plaquettes also alleviates the ambiguity produced by multiplexing (3:1 in the closer and 2:1 in the outer layer) the connections between the two metal layers on the n-side.

Readout

Pairs of plaquettes are wire-bonded in series to form half-modules, which are read out at either end by onboard CMOS chips, which each preamplify and multiplex the charges from 128 channels. 4–10 chips are read out serially at 2.5 MHz on a single

twisted pair cable connected via a line driver and repeater to the data acquisition crates (in the counting houses, ~ 25 m away). 36 (1991–3) or 48 (1994–5) SIROCCO[5] Fastbus modules, each with two readout units consisting of a flash ADC and digital signal processor are used to digitize the signal stream and perform pedestal and noise calculations and zero suppression. A total of 73,728 (1991–3) or 125,952 (1994–5) strips are read out.

Temperature and humidity variations (which are monitored as described in sections 3.2.3 and 3.2.10) as well as detector interventions can affect the alignment. Until 1995, the stability of the outer layer position relative to the ID was monitored (every 64th beam crossing) to a 1 μm precision using lasers.

Reconstruction

Channels passing a S/N cut (in 1994, 2.5 on the p-side and 1.4 on the n-side) are grouped into clusters, which are accepted if their total $S/N > 5$. The hit position is calculated from the pulse-height weighted position of the cluster maximum and its largest neighbour ($\eta = S_{i+1}/(S_i + S_{i+1})$), corrected for nonlinear charge sharing between the two strips. n-side clusters with a large incidence angle ($> 15^\circ$ from the normal) where the charge is spread over several strips use the strips on the edge of the cluster.

The local x or z coordinates cannot be converted into global DELPHI coordinates without additional information (usually external tracks). Before 1994, no z coordinate was available, and even since then there is no reliable way of directly associating the p-side hit with its n-side counterpart. Although the plaquettes are aligned closely with the z-axis, this is not perfect, so even a precise separate measurement of $R\phi$ or z cannot be made. For these reasons, it is necessary to associate initial track measurements from the ID, TPC, and OD with individual VD hits before conversion to the DELPHI coordinate system and inclusion into the global track fit. First $R\phi$

[5] ***Si****licon Strip* ***R****ead****o****ut* ***C***AMAC ***Co****ntroller,* anachronisticly named since they are Fastbus modules.

and then (using the resultant precision improvement) z hits are associated with each track. Remaining unassociated hits are checked for the possibility of VD-only tracks (perhaps due to material interaction outside the VD) using the beamspot position as the external constraint.

In order to obtain the full precision of the Vertex Detector, the relative positions of the plaquettes as well as the global alignment of the VD within DELPHI must be accurately measured [26]. The relative position of each module within a half-shell is determined to 25 μm before insertion into DELPHI with a combination of microscope (for the strip positions relative to the module) and mechanical probe (relative module positions) measurements. The 2 μm (1994–5) microscope measurement precision is sufficient for plaquette–plaquette alignment. Tracks passing through the regions where two modules overlap, 3-hit tracks, and dimuon ($Z^0 \rightarrow \mu^+\mu^-$) events are used to improve the module–module alignment, align the two half-shells relative to each other, and align the VD with respect to the rest of DELPHI. An overall alignment precision of the order of half the intrinsic hit precision is obtained.

All these tasks are performed by a single software library, VDCLAP[6] [28], which was the first detector physics package in DELPHI to be used at all levels of the reconstruction (DELANA, DSTFIX, as well as analysis programs). VDCLAP operates on VD hit, track, alignment, association, efficiency, dead strip, and beamspot data held in standard `COMMON` blocks.

Performance

Minimum ionizing particles at normal incidence give (1994–5) S/N between 11 (closer z) and 17 (outer, $R\phi$ and z), producing a single-hit efficiency of 98–99% and, as shown in figure 2.7, an intrinsic resolution of 8–9 μm (7.6 μm in the outer layer) in $R\phi$ and 9–40 μm in z (9 μm for perpendicular tracks passing through the outer layer).

The overall precision of a vertex detector may be described in terms of track impact parameters (see definition in appendix B) with respect to the production

[6] ***V**ertex **D**etector **C**ommon **L**ibrary for **A**ll **P**rograms*

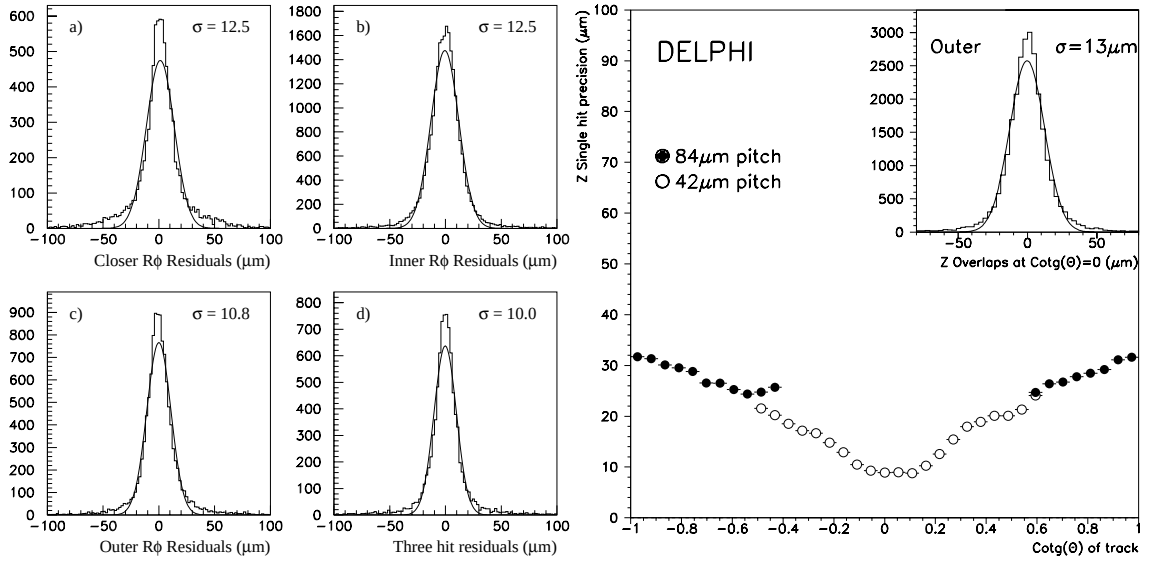

Figure 2.7: Vertex Detector intrinsic hit resolutions. Shown on the left are the $R\phi$ residuals for tracks passing through the overlap regions in the a) closer, b) inner, and c) outer layers ($\sigma/\sqrt{2}$ gives the single hit resolution). d) shows the inner-layer residuals for tracks with hits in all three layers (single hit resolution $= \sigma/\sqrt{1.5}$). In z the resolution depends on the track incidence angle, as shown for the outer layer on the right. The closed circles represent the region where the readout pitch was doubled. The inset shows the z hit residuals for normally incident tracks (single hit resolution $= \sigma/\sqrt{2}$).

vertex, usually the primary vertex (see section 2.11.3). There are two components to the impact parameter error (excluding the uncertainty in the production vertex, which does not concern us here): the intrinsic precision of the VD hits, extrapolated to the vertex; and the uncertainty due to multiple scattering in the beam pipe and VD material. In the $R\phi$ and Rz planes these may be parameterized with

$$\sigma_{R\phi} = \frac{\alpha_{\rm MS}}{p \sin^{3/2}\theta} \oplus \sigma_{0,R\phi} \tag{2.3}$$

and

$$\sigma_z = \frac{\alpha'_{\rm MS}}{p \sin^{5/2}\theta} \oplus \sigma_{0,z}\,, \tag{2.4}$$

where the constants $\alpha_{\rm MS}$ (multiple scattering) and σ_0 (intrinsic precision) are best fitted from the data as shown in figure 2.8. The fitted curves give $\alpha_{\rm MS} = 65\ \mu$m·GeV/$c$ and $\sigma_{0,R\phi} = 20\ \mu$m in equation 2.3 and $\alpha'_{\rm MS} = 71\ \mu$m·GeV/$c$ and $\sigma_{0,z} = 39\ \mu$m ($80^\circ < \theta < 90^\circ$) or 96 μm ($45^\circ < \theta < 55^\circ$) in equation 2.4.

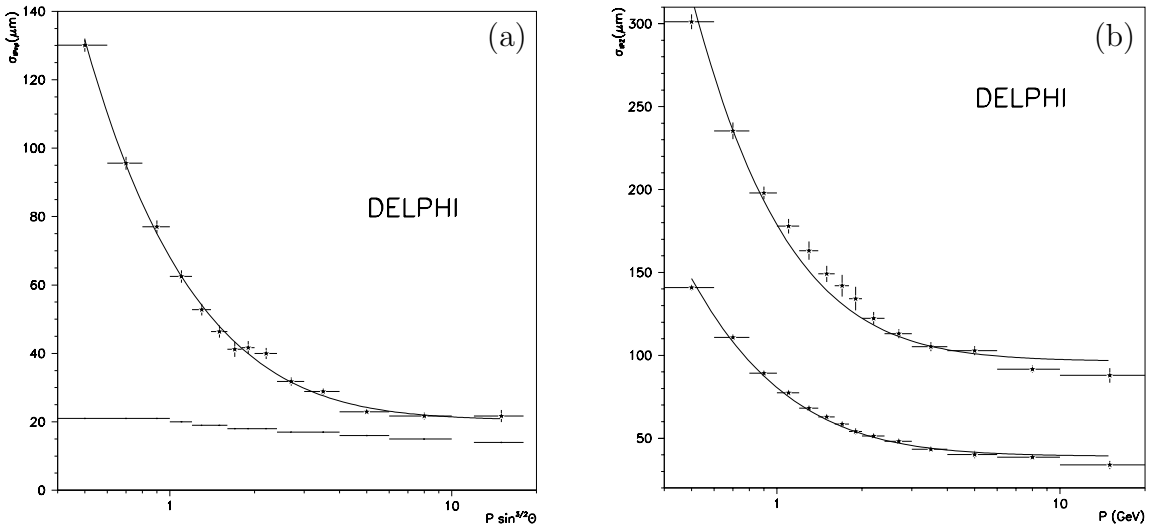

Figure 2.8: Track impact parameter errors as a function of momentum in (a) the $R\phi$ plane and (b) the Rz plane (lower curve: $80° < \theta < 90°$, upper curve: $45° < \theta < 55°$). Fits to parameterizations 2.3 and 2.4 are shown. The error due to uncertainty in the primary vertex position (shown on the lower curve in (a)) has been removed.

2.3.2 Inner Detector (ID)

The Inner Detector [29] consists of two components: the jet chamber is a high-resolution drift chamber providing $R\phi$ tracking information, while the trigger layers provide a rapid readout in both $R\phi$ and z.

The jet chamber consists of 24 azimuthal sectors, each with a plane of 24 axial wires down its centre. A variation in the drift field (and hence drift velocity) with R allows for constant drift time for all measurements of radial tracks, and hence a rapid trigger.

Outside this, the trigger layers consist of 5 layers of 192 multiwire proportional chambers (MWPC; before 1995) or straw tubes (1995 [30]). As well as measuring the z-coordinate, the $R\phi$ measurement can be used to help resolve the left–right ambiguity of the jet chamber.

2.3.3 Time Projection Chamber (TPC)

The TPC [31] is the main tracking detector in DELPHI, providing three-dimensional position information, a momentum measurement (from the track curvature in the magnetic field), and some particle identification based on the specific ionization in

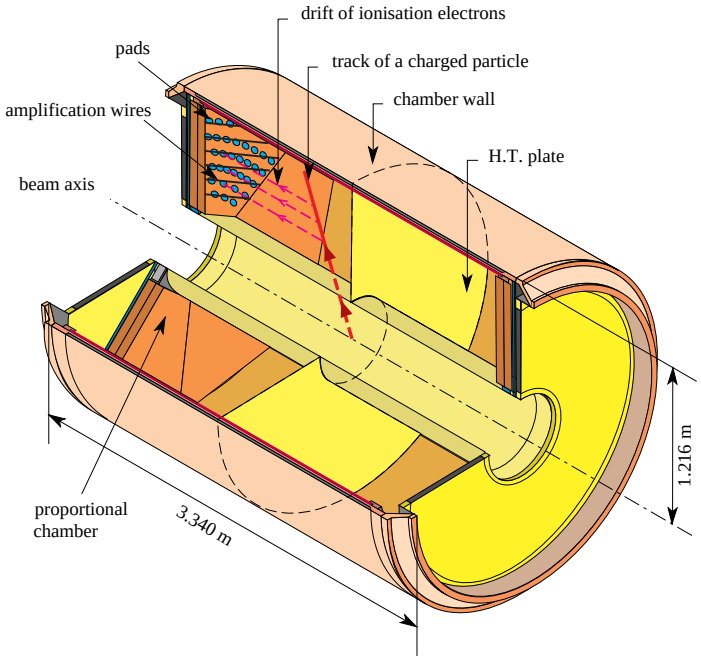

Figure 2.9: Schematic layout the the TPC.

the detector.

The layout of the TPC is shown in figure 2.9. The cylindrical vessel is divided in two by a cathode plane at $z = 0$ producing a uniform drift field of 187 V/cm. Primary electrons liberated by the passage of charged particles drift to the two ends of the detector. These are each divided into 6 azimuthal sectors, acting as MWPCs, each with 16 azimuthal cathode pad rows 4 mm behind 192 sense wires. The charge avalanche initiated on the anode wires by the primary electrons induces a signal on the pads, giving the $R\phi$-coordinate. The drift time to the sense wires gives the z-coordinate. The pulse height is a measure of the initial ionization ($\mathrm{d}E/\mathrm{d}x$), which can be used for particle identification.

2.3.4 Outer Detector (OD)

The size of the the TPC is constrained by the Barrel RICH surrounding it. The Outer Detector [32] provides an additional track measurement outside this to extend the distance over which the track curvature is measured and hence improve the overall momentum resolution.

The OD consists of 24 overlapping planks, each of 145 drift tubes, arranged into 5 staggered layers. The $R\phi$-coordinate is obtained from the drift time, and z (3 layers only) from the relative timings of the signal at the two ends of the anode wires.

2.3.5 Forward Chambers A (FCA)

The Forward Chambers A are mounted on either end of the TPC, and are thus mechanically part of the barrel. Each side consists of three modules each of two staggered layers of drift tubes, operating in limited streamer mode. The wire orientation of each module is 120° from the other two, providing two measurements of each of three non-orthogonal coordinates (x, u, v).

2.3.6 Forward Chambers B (FCB)

The Forward Chambers B are positioned outside the Forward RICH. Each endcap consists of two semicircular modules, each with 12 planes of wires. Pairs of staggered wire planes are orientated 120° from their neighbours, providing four measurements of each of the same (x, u, v) coordinates used in the FCA.

2.4 Ring Imaging Cherenkov Counters (RICH)

The RICH detectors (RIB [33] and RIF [34]) employ an ambitious technique to identify charged hadrons in the barrel and endcaps respectively. The velocity, β, of a particle travelling faster than the local speed of light in a material medium may be determined by measuring the presence and angle of emission of Cherenkov light. This ultraviolet light is detected using the time projection technique in quartz drift tubes (48 in the barrel, 24 in each endcap) containing a small quantity of a photo-ionizing vapour (TMAE). Both the Cherenkov angle (reconstructed from the positions of individual photons crossing the drift tubes with respect to the particle's trajectory) and number of photons give a measure of the particle's velocity. With the momentum determined

from the tracking detectors, this allows, in many cases, the particle's mass, and hence identity, to be determined.

Two perfluorocarbon Cherenkov radiators are used: a liquid radiator consisting of C_6F_{14} to identify soft particles (0.7–8 GeV/c) and a gaseous radiator of C_5F_{12} (RIB) or C_4F_{10} (RIF) to identify hard particles (2.5–25 GeV/c). The gas radiator is situated behind the drift tubes, so the Cherenkov light is reflected and focused back to them with parabolic/spherical (RIB/RIF) mirrors on the far wall of the detector. No focusing is required for light from the liquid radiator which is thin compared to its distance from the drift tube.

2.5 Calorimetry

By converting an incident particle into a shower of secondary particles, calorimeters provide information on the energy of neutral as well as charged particles and can help in particle identification. Electromagnetic calorimeters are designed for the identification of electrons and photons, which induce a shower of electrons, positrons, and photons by elastic Coulomb scattering from nuclei in the converter. On the other hand, hadron calorimeters rely specifically on detecting the hadron showers produced by inelastic hadronic interactions with the nucleons of the converter.

The two principal electromagnetic calorimeters in DELPHI are the HPC in the barrel and EMF in the endcaps. The SAT (before 1994), STIC (from 1994), and VSAT provide additional electromagnetic calorimetry in the very forward region, though are mainly used for the luminosity measurement (see section 2.8). The barrel and endcap Hadron Calorimeters (HAC) are of similar design. The properties of the calorimeters are listed in table 2.3.

2.5.1 High-density Projection Chamber (HPC)

The barrel electromagnetic calorimeter, HPC [35], consists of 6 rings of 24 modules each. Each module is a small TPC, segmented with 41 lead partitions, which induce

Detector	Geometric Acceptance			Depth	Samples along shower	Readout granularity [deg]		Shower resolution
	R [cm]	$\|z\|$ [cm]	θ [deg] $(+z)$			$\Delta\theta$	$\Delta\phi$	(σ_E/E) [%]
HPC	208–260	≤ 254	≥ 43	$18X_0$	9	.1	1	6.4
HAC (barrel)	320–479	≤ 380	≥ 43	$6\lambda_I$	4	3	3.75	17
SAT (–1993)	10–36	233–285	2.5–7.7	$28X_0$	8	.7	7.5,15	4.4
STIC (1994–)	6.5–42	218–249	1.7–10.6	$27X_0$	49	.9	22.5	2.7
EMF	46–240	284–340	10–36.5	$20X_0$	1	1	1	3.8
HAC (endcaps)	65–460	340–489	11–48	$6\lambda_I$	3–4	2.6	3.75	17
VSAT	$\sim$ 6–9	770	0.3–0.5	$24X_0$	12			5

Table 2.3: Some characteristics of the DELPHI calorimeters: barrel and forward electromagnetic calorimeters (HPC and EMF respectively), Hadron Calorimeter (HAC), and luminosity monitors (SAT/STIC and VSAT). X_0 is the radiation length and λ_I the nuclear interaction length. The shower energy resolution is given for 45.6 GeV.

an electromagnetic shower from the passage of electrons or photons, as well as providing the drift field. A pattern of pads at the end of each module measures the radial and azimuthal coordinates, with the z-coordinate coming from the drift time. This technique provides a three-dimensional picture of the evolution through the lead converters of an electromagnetic shower. Scintillators [36] to provide fast triggering on electromagnetic showers are placed close to the position of shower maxima in the HPC.

2.5.2 Forward Electromagnetic Calorimeter (EMF)

The Forward Electromagnetic Calorimeter [37] consists of 4532 lead glass blocks on each side. The Cherenkov signal induced by the charged particles in a shower is read out by the phototriode backing each block.

2.5.3 Hadron Calorimeter (HAC)

The iron yoke for the magnet is instrumented with plastic streamer tubes [38] to detect showers produced by hadrons interacting in the iron. The barrel Hadron Calorimeter consists of 20 layers of limited streamer tubes sandwiched between 5 cm thick iron plates and segmented into 24 modules. A similar arrangement of 12 sectors are used in each endcap. Each tube consists of a plastic cathode surrounding a single anode

wire. The streamer charges from the anodes of 4–7 layers are read out together. Since 1995 (1996 in the endcaps), the cathode of each tube has been read out independently, thus increasing the granularity to improve the π/μ separation [39].

2.6 Muon Chambers

The Muon Chambers (MUC) are designed to identify muons by detecting them outside most of the iron of the hadron calorimeter — all other charged particles are likely to have been absorbed within the calorimeters. Since muons are minimum ionizing particles with an energy loss of $\mathrm{d}E/\mathrm{d}x \approx 0.016$ GeV/cm in the HAC iron, any with momenta above 2–3 GeV/c can penetrate the ~ 110 cm of iron.

Three layers of drift chambers are provided for muon detection in the barrel, and two in the endcaps. During 1994, additional chambers were added covering the gap at 50° between the barrel and forward muon chambers.

2.6.1 Barrel Muon Chambers (MUB)

Drift chambers, operating in proportional mode and surrounding the DELPHI barrel, make up the Barrel Muon Chambers [40]. As shown in figure 2.10, the **inner** modules (20 cm inside the iron of the Hadron Calorimeter) are composed of 14 chambers bonded together, arranged into three layers. The third layer is not normally read out, but was included as a spare, given the near impossibility of replacement. The **outer** and **peripheral** modules (outside the iron), each made up of 7 chambers in two layers, are arranged such that the peripherals cover the cable gaps between outer modules. In all cases the active chambers within each module are staggered in order to resolve the drift chambers' inherent left–right ambiguity. Two modules, separated by a 3 cm gap at $z = 0$, cover the length of the DELPHI barrel.

Figure 2.11 shows a single MUB chamber. Most have a gas volume of $363 \times 20 \times 1.6$ cm^3, consisting of an argon/methane/carbon dioxide mixture in proportions 84.6/8.9/6.5% (1994).

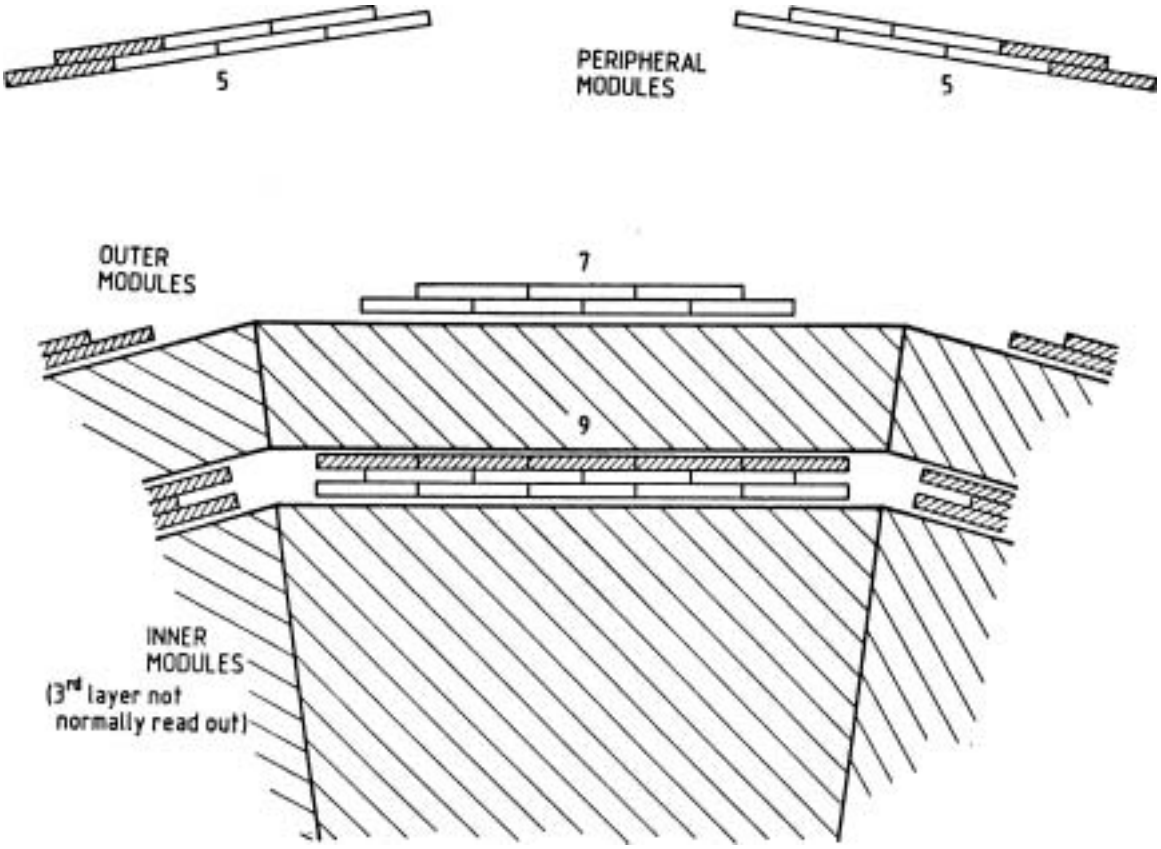

Figure 2.10: xy view of a Barrel Muon Chamber sector. The shaded third layer of the inner module is not used.

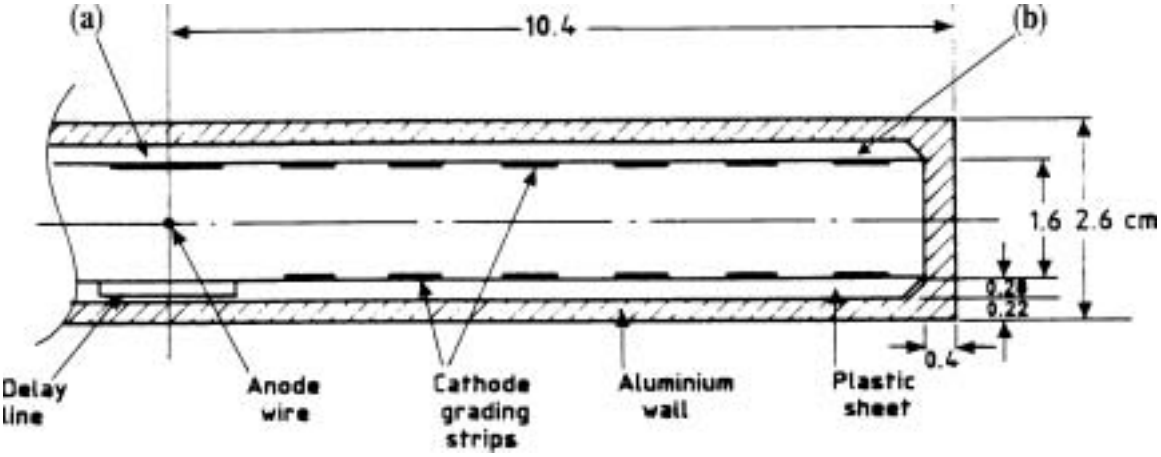

Figure 2.11: Cross-section in the xy plane showing half of a Barrel Muon Chamber. The dimensions are given in cm. The labels (a) and (b) are referred to in the text.

Charged particles (mostly muons, hopefully!) passing through this gas produce electron–ion pairs. These drift at a constant velocity of 4.6×10^{-3} cm/ns, accelerated by the electric field and decelerated by collisions with gas molecules. The roughly uniform 400 V/cm electric field is produced between a 47 μm diameter gold-plated tungsten anode wire at 6150 V, running down the centre of the chamber, and 13 copper cathode strips along each wall, graded between 4000 V (on the central strip, (a)) and ground (at the edges, (b)).

When the electrons approach the central anode wire, they gain sufficient energy from the higher field there to ionize the gas, producing an avalanche of electron–ion pairs and a signal on the wire. The time from the incident particle's crossing the MUB (assumed to be when the e^+e^- bunches collided in LEP) and this signal is the drift time, which gives a measure of the drift distance and hence $R\phi$ coordinate (assuming the left–right ambiguity can be resolved).

One of the two wider central cathode strips acts as a delay line. It is composed of insulated copper windings with a signal propagation time of 0.5 cm/ns. The signal induced on the delay line from the avalanche at the anode is measured at both ends of the chamber, the relative times of arrival giving a measure of the z-coordinate.

An intrinsic measurement precision of about 1 mm in $R\phi$ and 10 mm in z is obtained from each chamber.

2.6.2 Forward Muon Chambers (MUF)

The Forward Muon Chambers [41] consist of two planes of chambers in each endcap, operating in limited streamer mode. One plane is 20 cm inside the iron of the forward HAC, the other outside. They each consist of four 4.4×4.4 m^2 quadrants (with a corner cut off to make room for the beampipe) of two layers of 22 drift chambers each. The two layers have wires orthogonal to each other, so that the drift coordinate of one measures x, the other y.

Each drift chamber (see figure 2.12) has a sensitive volume of $435 \times 19 \times 2$ cm^3, filled with a carbon dioxide/argon/isobutane/isopropanol vapour mixture in proportions

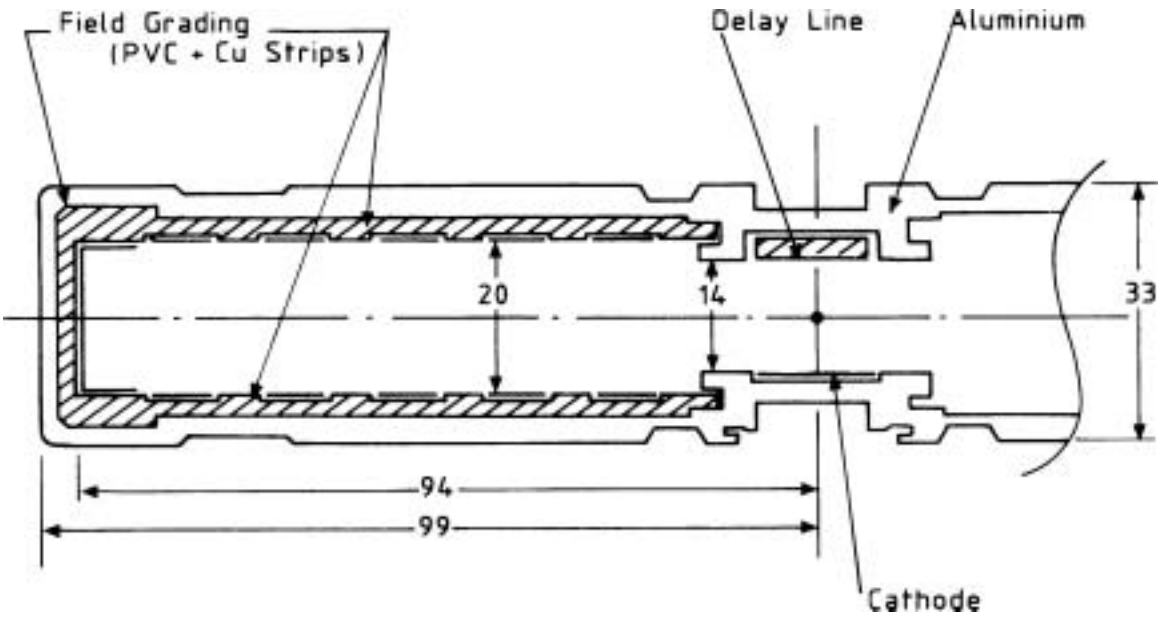

Figure 2.12: Cross-section in the xz or yz plane showing half of a Forward Muon Chamber. The dimensions are given in mm.

68.3/15.0/15.0/1.7%. Its principles of operation are similar to that of the MUB, except that the MUF is operated in limited streamer rather than proportional mode. The anode is a 100 μm diameter stainless steel wire. The drift velocity is 7.3×10^{-4} cm/ns in the 700 V/cm electric field. The drift time to the anode gives one coordinate (x or y) to a precision of about 1 mm, while the propagation time down the delay line gives the other (y or x) to about 2 mm.

2.6.3 Surround Muon Chambers (MUS)

The Surround Muon Chambers [42], which were added during 1994, cover the gap at $\theta \sim 50^\circ$ between the barrel and forward muon chambers, significantly improving the hermeticity of DELPHI's muon detection. Each of the eight chambers (mounted at the sides, top, and bottom of each endcap) is composed of two modules of two planes of plastic streamer tubes of the same design as those of the Hadron Calorimeter (see section 2.5.3).

2.7 Scintillators

Scintillators provide a very rapid signal on the passage of charged particles, and so are an important component of the Trigger to read out the rest of the detector. They can also be used to reject cosmic muons, which are not synchronized with the beam crossing, as well as completing the angular coverage over dead regions in the other detectors. Light generated in the scintillating material is detected with photomultipliers.

The scintillator layer in the HPC has already been mentioned (section 2.5.1). The Time of Flight (TOF) counters [43] in the barrel are mounted just outside the Solenoid, and the Forward Hodoscope (HOF) outside the iron in the endcaps. In order to identify the presence of unreconstructed missing energy (particularly important for particle searches at LEP 2) due to the gaps in the calorimeters, lead-scintillator counters are placed in the HPC θ-gaps at 90° [45] and 40° [44], and in the ϕ-cracks between HPC modules.

2.8 Luminosity Monitors

Knowledge of the electron–positron luminosity is required for the measurement of absolute cross-sections, which are given by

$$\sigma = \frac{N_{\mathrm{sel}} - N_{\mathrm{bkg}}}{\varepsilon \int \mathcal{L} \mathrm{d}t} \tag{2.5}$$

where the numbers of events in a selected sample are N_{sel} (total) and N_{bkg} (background), and the selection efficiency is ε.

The integrated luminosity, $\int \mathcal{L} \mathrm{d}t$, is obtained by measuring the rate of small-angle Bhabha (non-resonant $\mathrm{e^+e^-} \rightarrow \mathrm{e^+e^-}$ scattering) events. The cross-section of this reaction is dominated by well-understood QED processes. Using the lowest-order

Born approximation, the cross-section in the angular range $\theta_{\min}$ to $\theta_{\max}$ is given by

$$\sigma_B = \frac{16\pi(\alpha\hbar c)^2}{s}\left(\frac{1}{\theta^2_{\min}} - \frac{1}{\theta^2_{\max}}\right) \approx \frac{1042\ (\mathrm{GeV})^2 \cdot \mathrm{nb}}{s\theta^2_{\min}} \tag{2.6}$$

where s is the square of the centre of mass energy and α is the fine-structure constant.

Using this and equation 2.5 for Bhabha events selected by the luminosity monitors, the e^+e^- luminosity may be measured. Equation 2.6 shows the importance of accurately measuring the lower bound of the angular acceptance.

2.8.1 Small Angle Tagger (SAT)

The Small Angle Tagger calorimeter [46] consisted of cylindrical layers, concentric with the beam axis, of lead and scintillating fibres, read out with photodiodes. A precisely machined lead (–1992)/tungsten (1992–3) mask, 12 radiation lengths ($12X_0$) deep, accurately defined the inner edge of the fiducial region. A silicon-strip tracker [47] (1991–3) was used to check for distortions in calorimeter position measurements. The SAT was in operation until the end of 1993.

2.8.2 Small Angle Tile Calorimeter (STIC)

The Small Angle Tile Calorimeter [48] replaced the SAT for the start of datataking in 1994. It is a sampling calorimeter consisting of layers of scintillating tiles sandwiched between steel-laminated lead plates. The tiles are read out, via wavelength shifting fibres, with phototetrodes. Silicon-strip detectors aid the reconstruction of the shower direction. A $17X_0$ thick tungsten mask on one side is used to accurately define the inner radial acceptance for Bhabhas.

2.8.3 Very Small Angle Tagger (VSAT)

The Very Small Angle Tagger [49], by virtue of the higher Bhabha rates at lower angles (equation 2.6), allows the luminosity to be monitored online. It consists of interleaved

tungsten converters and silicon detectors positioned beyond the LEP superconducting quadrupole focusing magnets on either end of DELPHI.

2.9 Solenoid

The solenoidal magnet [50] produces a field of 1.2 tesla by using a 2.6 m-radius superconducting coil carrying a current of 5000 A, maintained at a temperature of 4.5 K. Trim coils round the two ends of the main coil ($I \approx -850$ and $I \approx -650$) are used to improve the field homogeneity.

2.10 Data Acquisition (DAS) and Trigger

The Data Acquisition system (DAS, rather than the more common acronym, DAQ) [51] is responsible for reading out the digitized data from the various parts of the detector and recording the results for subsequent analysis.

The basic problem to be overcome by most data acquisition systems is the difference in rate between beam collisions (in LEP, beam cross-over, or **BCO**, occurs every 22 or 11 μs depending upon whether there are 4 or 8 bunches per beam) and the maximum possible (or desirable) data readout and storage rate (perhaps 20 Hz). The Trigger system [52] overcomes this problem by only reading out the detector if there are indications of a significant interaction.

Four levels of triggering are used in DELPHI. The first level, **T1**, makes no correlation between detector partitions, and uses information only from detectors with fast readout times: ID, TPC ($\theta < 43°$), OD, FCA, FCB, TOF, HOF, HPC scintillators, EMF, and MUB; so the decision can be made 3.5 μs after BCO. Once the TPC, HPC, and MUF drift times are complete the signals from these detectors (available 23 μs after BCO) as well as correlations between detectors, can be added to provide the second level trigger, **T2**, 39 μs after BCO. At a nominal luminosity of 1.5×10^{31} cm^{-2}s^{-1}, the $\sim$ 700 Hz (T1) and $\sim$ 4.5 Hz (T2) trigger rates produce dead times of 2% (T1) and 1% (T2).

The various T2 components are designed to select tracks, muon signals, calorimeter energy deposits, or Bhabha events. There is considerable redundancy between Trigger components, allowing an accurate determination of the trigger efficiency, though it is barely distinguishable from 100% for hadronic events.

T3 repeats the T2 logic in software using digitized and calibrated data, allowing tighter cuts to be applied. **T4** uses a tailored version of the DELPHI reconstruction program, DELANA (see section 2.11.1), to reject events with no track pointing towards the interaction region and no energy deposit in the calorimeters. The T3 and T4 processing occurs asynchronously with respect to BCO, introducing no dead time. Each reduces the data rate by a factor of two, so data is recorded at a rate of about 1 Hz.

The data acquisition performed in the counting rooms in the experimental cavern is based on the Fastbus standard [53]. Each detector partition has its own digitization modules, most with a 4-event Front-End Buffer (**FEB**) to reduce the loss of events due to chance spurts in the trigger rate. Following a positive T2 signal the FEB data is copied (asynchronously with BCO) to the Crate Event Buffer (**CEB**) by the Crate Processor (**CP**) program, running in a Fastbus Intersegment Processor (**FIP**). The FIP also performs local T3 processing. Data from a number of CEBs are merged by the partition's Local Event Supervisor (**LES**; also running in a FIP) into the Spy-Event Buffer (**SEB**; used for local monitoring) and Multi-Event Buffer (**MEB**).

For events that pass T3, individual partitions' MEB data are combined by the Global Event Supervisor (**GES**) into the Global Event Buffer (**GEB**) and transferred to the VAX mainframe on the surface via optical fibre. On the VAX the data is managed by the Model Buffer Manager (**MBM**) and written to disk by Data Logger processes. T4 processing is performed, and selected events are written to disk and then copied to tape (before 1995: 250 Mb IBM 3480 cartridges, written locally; now 10 Gb Digital Linear Tape (DLT) in the CERN central computer centre).[7]

[7]The FEB is connected to the CEB. The CEB is connected to the SEB. The SEB is connected to the MEB. The MEB is connected to the GEB. The GEB is connected to the MBM. *Hear the word of the Lord.*

2.11 Event Reconstruction

2.11.1 Offline Processing

The **raw data** tapes written by the Data Acquisition system go through a number of standard processing steps before being used for individual analyses, such as the one described in chapter 4. Their task is to infer details of the products of the e^+e^- interaction from the electronic measurements made by the detector. Thus, for example, the raw data, consisting of digitized drift times and charge measurements on specified channels in the tracking detectors, are converted into trajectories through DELPHI from which the creation point, direction, and momentum of the charged particles can be inferred.

The majority of this generic analysis is performed by the **DELANA** program [54], which is based on the **TANAGRA**[8] [55] data model and access routines. TANAGRA provides a common format for storing the results of each stage of the processing,[9] as described below.

1. Calibrations are applied to the digitizations from the raw data and saved in a semi-standard form (**TD** TANAGRA banks).

2. Where possible, pattern recognition, local to each subdetector, is performed. The sophistication of the output track elements (**TE** banks) depends on the subdetector concerned (e.g. individual $R\phi$ or Rz measurements from the VD, track segments from the ID, TPC, and OD, and energy clusters from the calorimeters).

3. TPC track elements are extrapolated to the other detectors and an initial association is made with their track elements (not the VD at this stage). Additional searches are made for ID–OD (in the TPC cracks), FCA–FCB, and FCB–beamspot (for very small angles) track element associations in order to recover tracks

[8] ***T**rack **Ana**lysis and **Gra**phics*

[9] "TANAGRA is like the mafia: it protects you, it is expensive, and you did not ask for it." [55]

that are not seen (or well measured) in the TPC. At this stage, ambiguous associations are maintained as separate track strings (**TS** banks).

4. Each track string is then passed through the full track fit (see section 2.11.2). Ambiguities can now be removed using the fit χ^2, leaving a self-consistent set of tracks (**TK** banks).

5. These tracks are then extrapolated to each detector and used to guide a second stage of local pattern recognition and, where necessary, the track is refitted. It is at this stage that the VD hits are associated and included in the track fit (done here in order to take advantage of the optimum track determination in the VD association). A final search for missed tracks is performed on unassociated TEs.

6. Calorimeter energy clusters, muon chamber hits (see section 2.11.4), and RICH information are associated with the fitted tracks. Unassociated calorimeter energy deposits are used to form neutral 'tracks'.

7. A vertex search produces track bundles (**TB** banks), and a vertex fit performed to determine vertex positions (primary and possibly decay vertices; **TV** banks). At present this information is only used for diagnostic purposes, since the cuts used in vertex fitting are highly analysis-dependent.

Constants and parameters used by DELANA are read [56] from the CARGO [129] database based upon the time the event being analysed was captured by the DAS. Section 3.7 describes CARGO and the information written to it by the online system. CARGO is also used by DELANA for many of its other parameters, such as the detector geometry. The statuses of the various detector partitions are combined with the DELANA processing status to provide a set of flags, which are written out as run selection files for use in physics analyses.

Following the DELANA reconstruction, two types of tagging algorithms are applied. Both have very loose cuts in order not to reject events that might be accepted after post-DELANA corrections are applied. The 'DELANA tags' [57] produce a broad

categorization of each event as, for example, hadronic Z^0, leptonic Z^0, Bhabha seen in SAT/STIC, etc. The 'Physics Teams tags' [58] select events of interest to specific classes of analysis. Events selected by either of these groups of tags are written to the main ('**DST OR**') output stream.

A full DELANA processing of a year's data can take many weeks. In order to allow corrections and refined calibrations (e.g. Vertex Detector alignment) to be updated at frequent intervals, a second stage of processing, **DSTFIX** [59], is performed (and can be reperformed) on the DST output of DELANA. DSTFIX can make changes at the TE level and refit tracks. It is also used to adjust the efficiency, cleanliness, and precision of simulated data to better match the quality of the real data. A number of particle identification algorithms, considerably more sophisticated than those used in DELANA, are run on the output of DSTFIX: charged hadrons (p, $K^{\pm}$, and $\pi^{\pm}$) are identified with the RICH [60] and TPC dE/dx [61], electrons [62] with the electromagnetic calorimeters, and muons [75, 76] with the muon chambers. A primary vertex fit and b-tagging algorithm [63] is also run to identify $Z^0 \rightarrow b\bar{b}$ events by the increased impact parameters of tracks from B hadron decays.

The analysis chain causes the data to be interpreted and transformed between a number of forms, all of which are based on the **ZEBRA** [64] memory management system (part of the CERN library), which provides dynamic data structuring within Fortran 77 (which lacks the pointer or reference data types required for this data model). ZEBRA also provides methods for file input/output for these data structures in a format that allows the data to be transported between computers with different numeric representations.

Raw data [65] is output by the DAS (or, for simulated events, by DELSIM) and read in by **DELANA**.

TANAGRA [55] provides a data model to ensure a clean and safe interface between DELANA routines, since these are written and maintained by many different people. TANAGRA is also based on ZEBRA, so its data can be output to a file,

and in fact this was the primary output of DELANA in DELPHI's first two years. However, since then, the volume of data has made it impractical to save the detailed TANAGRA files for anything other than debugging purposes.

DST[10] [66] is now the primary output of DELANA. It includes reconstructed track parameters, as well as the TE track elements, allowing the tracks to be refit post-DELANA. The average full DST hadronic event size is 60 kilobytes.

LongDST [67] is written by DSTFIX and has the results of the particle identification and b-tagging algorithms included.

ShortDST [68] is also written by DSTFIX, but includes less reconstruction information (e.g. it does not include the TEs), reducing the average hadronic event size to 20 kilobytes.

MiniDST [69] is written by the PHDST program. It contains a subset of information from the shortDST, stored in a compressed form, allowing it to be kept on disk for rapid analysis. The average miniDST hadronic event size is 6 kilobytes.

All the offline code is written in Fortran 77 [116]. Due to the large number of collaborating institutes within DELPHI as well as its long timescale, the simulation and analysis tools have been required to work on a diverse collection of computing architectures and operating systems: HP-UX and DEC Alpha Unix, VAX and Alpha VMS, and IBM VM/CMS systems being only the most common. In order to allow for system-specific code, as well as providing a rudimentary form of revision control, the PATCHY system [70] was used.

2.11.2 Track Reconstruction

Two stages of track fitting are performed in DELANA (once on the possibly ambiguous track strings, and then again following ambiguity resolution) as well as an additional

[10] ***D**ata **S**ummary **T**apes*

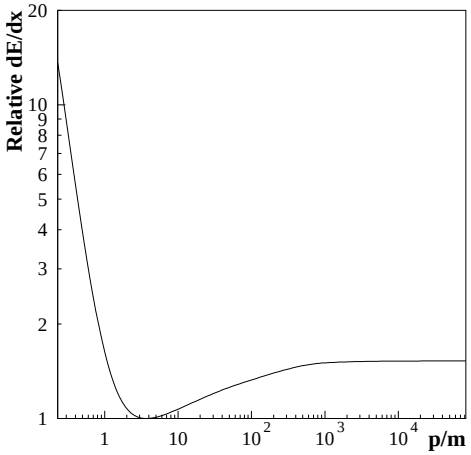

Figure 2.13: Assumed variation of energy loss ($\mathrm{d}E/\mathrm{d}x$) with momentum (plotted as p/m), relative to the minimum ionization. $\mathrm{d}E/\mathrm{d}x_{\mathrm{min}}$ depends on the materials traversed; composite values between 0.02 and 0.2 GeV per radiation length are typical.

track fit using the corrections and improved VD alignment available in DSTFIX. Essentially the same algorithm is used in each case, with TEs as input. In the case of the ID, TPC, and OD these are themselves the result of local track fits.

The effects of the particle's passage through the material between the points where measurements are made must be taken into account. Small-angle **multiple scattering**, which introduces additional uncertainties in the angle of extrapolated track elements, is described by a Gaussian distribution with RMS plane-projected scattering angle of

$$\sigma_\theta = \frac{0.0136 \text{ GeV}/c}{p}\sqrt{x/X_0}\,[1 + 0.038\ln(x/X_0)] \tag{2.7}$$

(a good approximation for $\gamma \gg 1$), where p is the momentum and x/X_0 is the fraction of a radiation length traversed. Scattering at larger angles is not treated at this stage. The **energy loss** due to ionization is also taken into account in the fit as shown in figure 2.13.

The track fit is based on a Kalman filter [71], which allows 'outliers' (TEs whose presence in the track fit significantly degrades the fit χ^2) to be iteratively removed as part of the fit process.

The spatial precision of the overall tracking is largely determined by the vertex detector, so the results were summarized in section 2.3.1 (see in particular figure 2.8).

The momentum precision at 45.6 GeV/c can be measured using $Z^0 \to \mu^+\mu^-$ events (radiative Z^0 decays are removed by requiring an acollinearity of less than 0.15°). These are shown in figure 2.14. RMS widths of $\sigma_p/p = 3\%$ in the barrel and 6% in the endcaps are found. At lower momenta, simulated data are used, as shown in figure 2.15.

2.11.3 Beamspot

The primary vertex (Z^0 decay position) is within the region encompassed by the crossing of the electron and positron beams. Its RMS size is typically 200 μm in x, negligible in y (< 3.9 μm in 1994), and ~ 1 cm in z. The position and size change slowly throughout the LEP fill as well as between fills.

The beamspot position and size [72] (at least in the xy plane) can be used directly as a measure of the primary vertex position and error, as a constraint on an event-by-event primary vertex fit, or to identify tracks coming from a secondary vertex.

A primary vertex fit is performed for each hadronic event passing cuts designed to reduce the contribution from poorly measured tracks and secondary vertices. These are divided into samples corresponding to each tape written by the DAS ($\sim$ 200 hadronic events in 1994). For each sample a fit is performed, assuming independent Gaussian beam profiles in all three coordinates, and the primary vertex position and size in x and z is determined. The beam size in y is too small to measure for this sample size. Since the beamspot position determination is critically dependent on (and relative to) the detector alignment (particularly that of the VD), it is performed separately for each DST and shortDST production. The mean beamspot position is typically measured to an accuracy of $(\sigma_x, \sigma_y, \sigma_z) = (15, 5, 1500)$ μm for each sample.

2.11.4 Muon Identification

Similar algorithms are used for muon identification [73] in DELANA (the EMMASS package [74]) and afterwards (the MUCFIX [75] and MUFLAG [76] packages). The

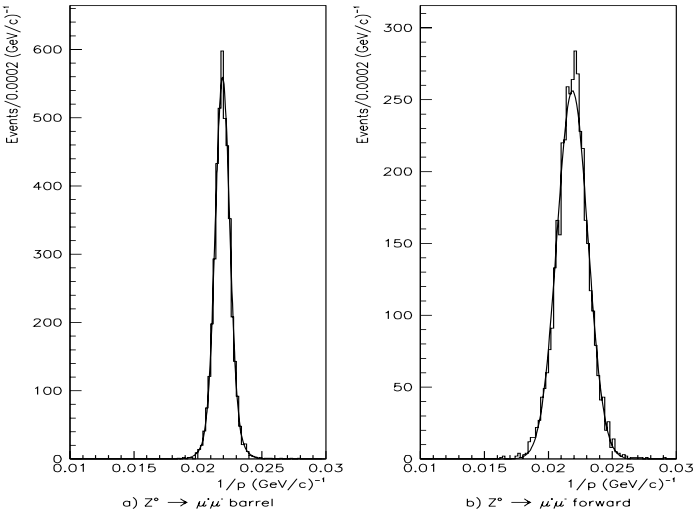

Figure 2.14: Inverse momentum distribution of 45.6 GeV/c ($1/p = 0.0219$) muons seen in (a) the VD, ID, TPC, and OD; or (b) the VD and FCB.

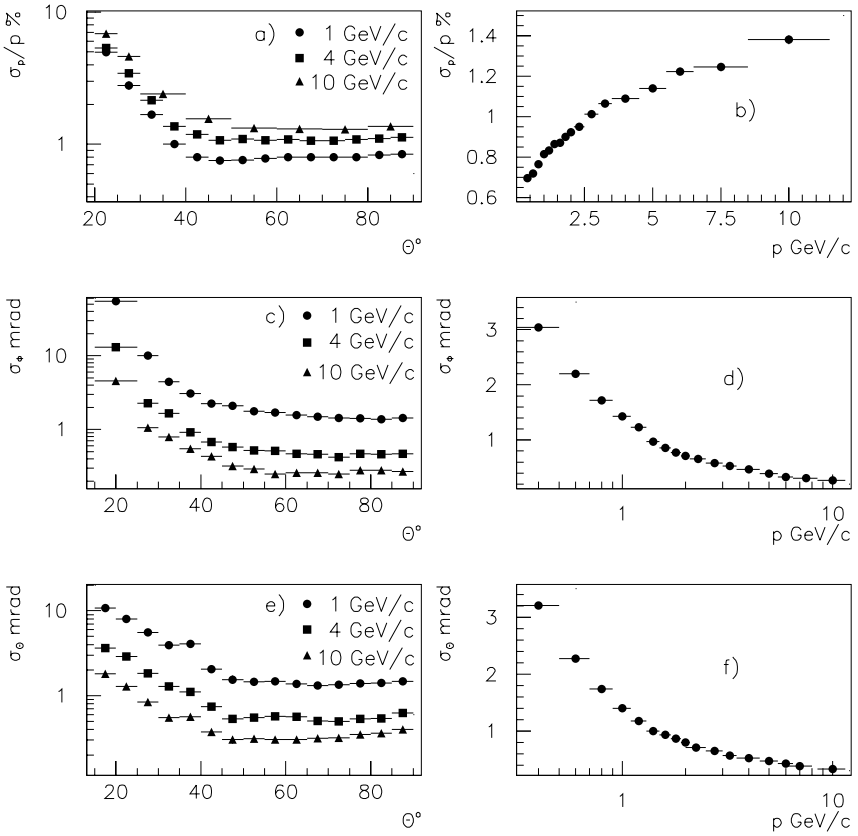

Figure 2.15: Track momentum precisions estimated by comparing simulated and reconstructed parameters. The errors in momentum (a,b), azimuthal angle ϕ (c,d), and polar angle θ (e,f) are shown. The variation of each parameter's precision with respect to θ is shown on the left; with respect to momentum on the right.

difference is that **EMMASS** employs extremely loose selection criteria (useful for producing dimuon ($Z^0 \to \mu^+\mu^-$) samples for checking and alignment), whereas **MUCFIX** allows for variable cuts, specifically those defined in **MUFLAG**, which are optimized for identifying muons in hadronic jets. MUCFIX can also take advantage of the improved tracking available after DSTFIX and, as is the case with all post-DELANA reconstruction, allows corrections to be implemented more rapidly.

Hadron contamination in the set of tracks selected as muons in jets is due to

Sail-through: About 0.3% of hadrons pass through the calorimeters without interacting.

Sneak-through: Hadrons that pass down the cracks between HAC sectors have a lower chance of interaction.

Punch-through: The dominant source of background is due to secondary particles produced by hadronic interactions, particularly in the outer layers of iron, which themselves penetrate to the muon chambers.

Decays in flight: Muons produced from pion or kaon decay are an additional source of background to muons produced closer to the production vertex.

Since the particles seen in the MUC from punch-through and decays in flight are not the same as the originating hadron, they will tend to have a slightly different trajectory. Their contribution can thus be reduced by requiring that the extrapolated trajectory of the supposed muon match the MUC hits within the accuracy expected from multiple scattering and measurement errors.

Contamination can be further reduced by requiring hits in muon chambers outside the iron, where they will have had to pass through an additional interaction length of iron.

EMMASS/MUCFIX perform a fit for the particle's trajectory at the MUC, using the MUC hit coordinates (and errors) and the extrapolated track position and direction (and full error matrix, including multiple scattering). χ^2s from this fit are used to

select the best association, drop bad hits, and reduce the contamination from punch-throughs and π/K decays.

MUFLAG provides four predefined selections, the results of which are written to the ShortDST. The **Very Loose** tag (intended for $Z^0 \to \mu^+\mu^-$ studies) has no cut on the χ^2, so the best association made (after the very loose preselection and bad hit rejection made by EMMASS) is used. The other three tags (intended for studies of muons in hadronic jets) use a tighter bad-hit cut and progressively tighter χ^2 cuts. The **Loose** tag aims to maximize efficiency. As well as tighter χ^2 cuts, the **Standard** and **Tight** tags require at least one hit in the chambers outside the iron.

The muon identification efficiency for the standard tag is shown in figure 2.16. The overall efficiencies and misidentification probabilities for all four tags are summarized in table 2.4. In both cases, particles only contribute if their momentum is greater than 3 GeV/c and their polar angle is within $20° < \theta < 42°$ (MUF) or $52° < \theta < 88.5°$ (MUB). These selections exclude regions of poor track reconstruction ($\theta < 20°$ and $88.5° < \theta < 91.5°$) or limited coverage (also $42° < \theta < 52°$). The MUS (only installed during 1994) is not used here.

2.12 Detector Simulation

Simulated events are of great importance in checking and/or correcting for non-trivial or unforeseen detector or physics effects, as well as comparing detector performance with expectations. With the possible exception of the effect being studied, simulated events should be as close as possible to real data events. Hence the primary goal of the simulation programme is to model closely the physical interactions involved, the detector performance, and the event reconstruction.

The DELPHI simulation program, **DELSIM** [77], is composed of three main components: generators, tracking, and detector response.

1. The primary physics processes can be modelled using a variety of generators. For Standard Model hadronic production, the **JETSET** [78] generator is most

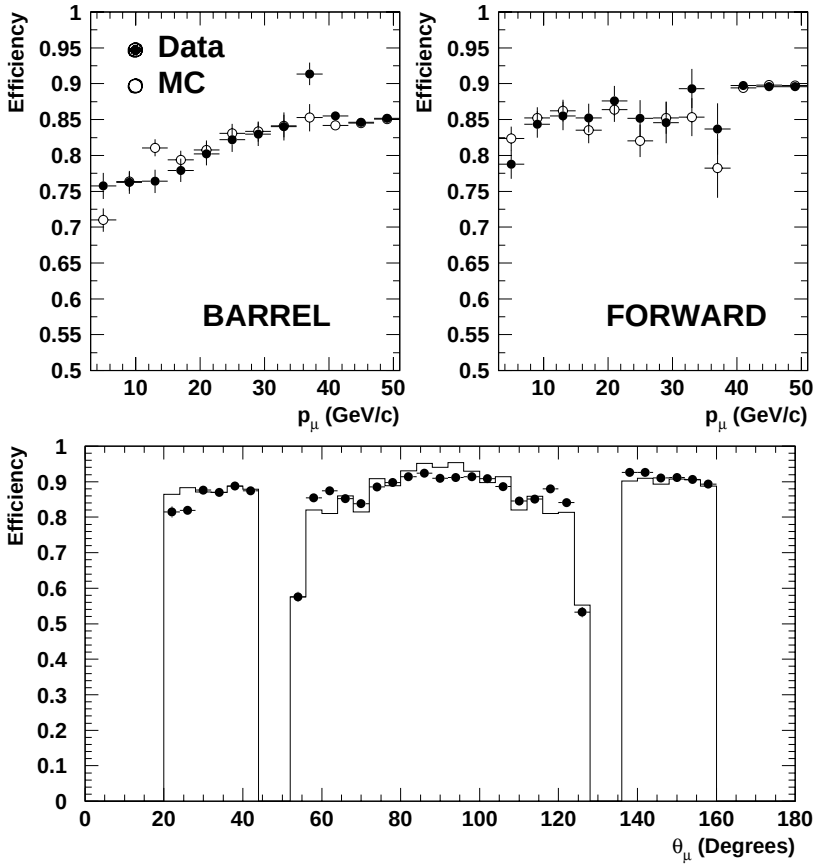

Figure 2.16: Identification efficiency in 1994 of standard muon tag as a function of momentum (above) and polar angle (below, where the solid line shows the efficiencies from simulation).

Tag			Very Loose	Loose	Standard	Tight
Efficiency (%)	MUB	Data	95.6±0.2	91.4 ±0.3	79.9 ±0.5	65.9 ±0.6
		MC	96.3±0.2	92.6 ±0.3	79.7 ±0.4	65.8 ±0.6
	MUF	Data	94.4±0.4	92.4 ±0.5	84.5 ±0.7	67.9 ±1.0
		MC	94.0±0.4	92.5 ±0.4	83.8 ±0.6	67.7 ±0.9
Misidentification probability (%)	MUB	Data	4.9±0.2	1.3 ±0.1	0.65±0.07	0.42±0.06
		MC	2.9±0.1	0.66±0.06	0.27±0.04	0.16±0.03
	MUF	Data	7.9±0.6	2.3 ±0.3	0.9 ±0.2	0.55±0.16
		MC	6.2±0.4	1.8 ±0.2	0.7 ±0.1	0.36±0.10

Table 2.4: Muon identification efficiencies and misidentification probabilities for the four MUFLAG tags on 1994 data. The **data** efficiencies and misidentification probabilities are determined using $\tau^- \to \mu^- \bar{\nu}_\mu \nu_\tau$ and $\tau^- \to \pi^- \pi^- \pi^+ \nu_\tau$ (and charge-conjugate) events respectively. These can be compared with the equivalent numbers from the simulation (**MC**).

commonly used. This simulates $e^+e^- \rightarrow Z^0 \rightarrow q\bar{q}$ and hadronization, producing a set of four-vectors for the next stage. JETSET model parameters are tuned using LEP data.

2. In DELSIM, particles are tracked through the detector, accounting for weak decays, curvature in the magnetic field, ionization energy loss, multiple scattering, the photoelectric effect, delta ray emission, bremsstrahlung, positron annihilation, pair production, Compton scattering, and nuclear interactions.[11]

3. Subsequently, the response of each part of the detector is simulated, producing a set of simulated electronic signals.

Since the output of DELSIM closely models the real raw data produced by the DAS, DELANA can be used directly, thus well-modelling the real data reconstruction. Like DELANA, DELSIM uses CARGO to store the detector geometry, material descriptions, and sensing device parameters (e.g. noise and efficiency). In principle, this allows simulated events to be produced for the current or any previous detector configuration.

[11] Note that unlike most other LEP and planned future detectors, the DELPHI simulation program is not based on GEANT [79], though GEANTH is used to simulate nuclear interactions.

Chapter 3

Slow Controls

3.1 Introduction and Overview

The DELPHI detector has been equipped with an automated system for monitoring and controlling technical aspects of the experiment, such as high voltages and gas supplies, for reporting and acting on changes in the status of the detector or its environment, and for maintaining the safety of the equipment.

This **Slow Controls** system should be distinguished from the **Data Acquisition** system (DAS; see section 2.10), which is responsible for the digitizing and recording of each physics event — the products of the electron–positron collision. The emphasis of the Data Acquisition system is on efficient triggering and fast readout, since the electron and positron bunches cross every 11 μs. In contrast, the Slow Controls reacts to events that can take from seconds to hours to develop, but is more concerned with reliability, particularly due to its safety requirements.

The overall structure of the DELPHI Slow Controls system is summarized in figure 3.1. As can be seen, the system is highly modular and highly distributed with many programs running on both high-level (VAX) and front-end (G64) processors.

The DELPHI Slow Controls operator makes use of two main graphical displays, shown in VAXstation windows. The status display gives a colour-coded representation of the state of the various detector partitions. These states are defined in the **State**

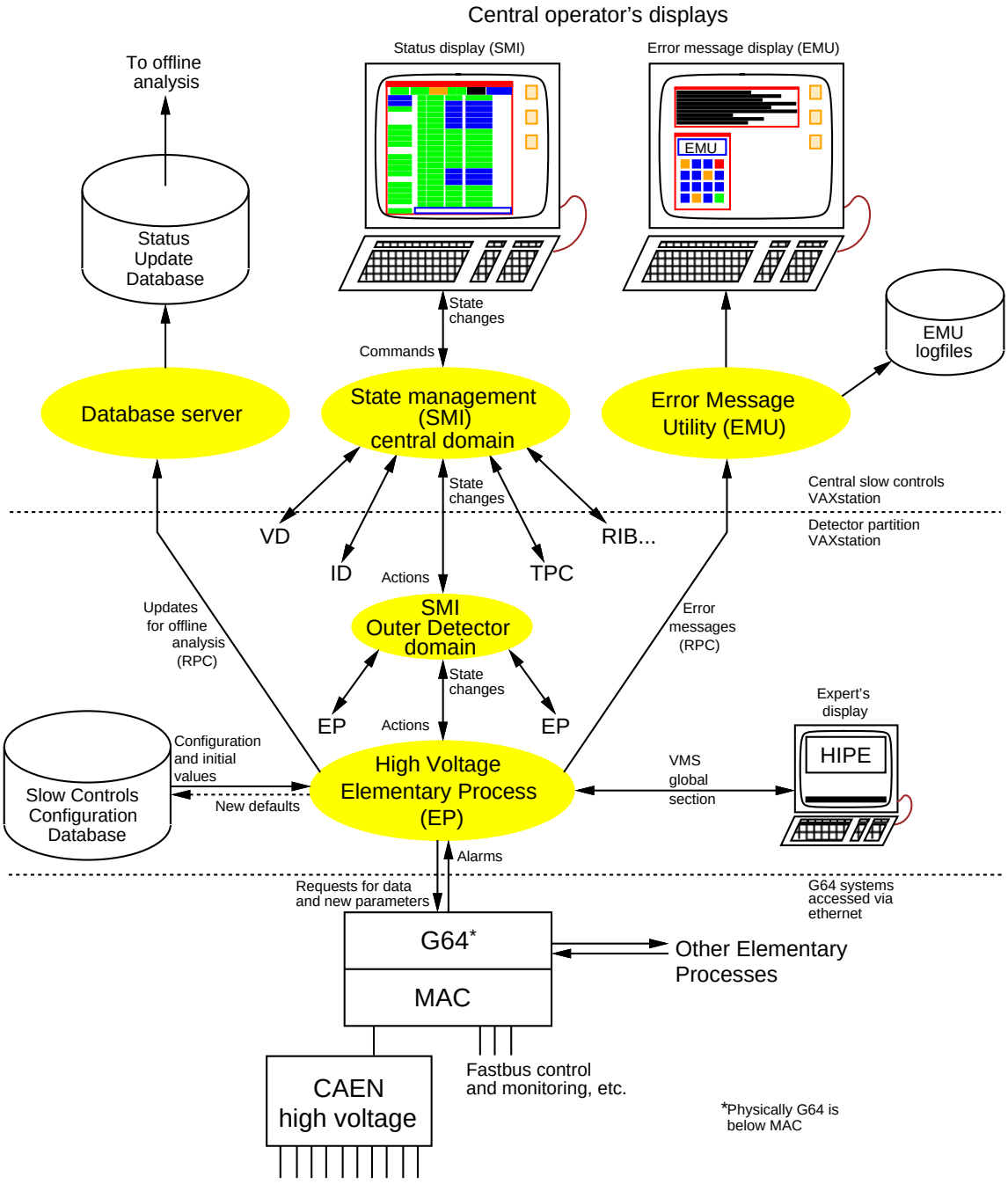

Figure 3.1: Diagram of the overall structure of DELPHI Slow Controls system represented by the example of the high voltage control of the Outer Detector.

Management Interface (SMI) (see section 3.8.1), which is a hierarchical set of objects representing different aspects of the detector as seen by the Slow Controls system. SMI is also responsible for passing commands (either to the whole of DELPHI or to a particular detector partition) down to the appropriate subsystems which act on them. During 1994 an even higher level of SMI-based automation, called **Big Brother** (see section 3.8.3), was added to coordinate the actions of the Slow Controls and the Data Acquisition systems with the states of the LEP machine. The error message display shows outstanding anomalies in a textual form, grouped according to detector partition. These messages are handled by the **Error Message Utility (EMU)** (see section 3.6).

Both SMI and EMU show conditions determined by the **Elementary Processes (EP)** (see section 3.5.1), which are the lowest-level VAX control programs. The Elementary Processes are also responsible for handling SMI commands, logging state changes to the **Status Update Database** (see section 3.7.2) for use by the off-line analysis, and providing a route for occasional expert intervention, using a user interface, **HIPE** (section 3.5.2).

The Elementary Processes communicate over ethernet (using the **Remote Procedure Call (RPC)** protocol) with the front-end control and monitoring microcomputers, the **G64** crates (see section 3.3). The G64s monitor and control a variety of different types of hardware using digital and analog monitoring and control devices. Most high voltage supplies are controlled by an intelligent **CAEN** high voltage unit [80] (see section 3.3.1), which is in turn controlled and monitored by the G64.

The unified **gas system**, which controls and monitors the flows and mixtures of gases supplied to various parts of the detector, and the **GSS** safety system, which monitors the detector and its environment for hazardous conditions, use different structures (see sections 3.9.1 and 3.9.2), but are integrated with the rest of the Slow Controls at the SMI and EMU level. These software links are complemented by a system of hardwired interlocks.

A brief description of the DELPHI Slow Controls system has been given previ-

ously [81]. In this chapter I give a detailed and considered description of the systems employed. A less technical version has also been published [82]. For detailed descriptions of the gas and safety systems the reader is referred to separate publications [83, 84]. The slow controls of the other three LEP experiments have been described elsewhere [85, 86, 87].

3.2 Detector Requirements

The various detector partitions exploit different techniques to achieve their aims of identifying or measuring the position, momentum, or energy of the products of electron–positron collisions. Consequently they have different requirements for their Slow Controls. Here only those aspects relevant to the Slow Controls are detailed. Full details of the detector itself may be found in chapter 2 and the references given therein.

3.2.1 General Principles

Most modern particle detectors rely on the detection of charged particles by their ionizing effect on the material they pass through. The charged particles are either those from the physics interactions or part of a shower of particles formed when either charged or neutral particles pass through a dense medium. The electrons (or ions) liberated by this ionization are drawn to an electrode by an electric field. These signals can then be amplified, digitized, and recorded for subsequent analysis.

To control and monitor the provision of these conditions is one of the major tasks of a slow controls system. Different types of detector use different ionizing materials, usually gases. Careful monitoring is required of the gas supply, mixing, and distribution, particularly as a number of the gases are flammable. To provide sufficiently strong electric fields, high voltages of thousands of volts are often required. The electronics used to process the detected signals requires carefully controlled (low) voltages. All these systems must be capable of being switched off quickly in the event

Partition	Gas	%	Gas	%	Gas	%	Gas	%
ID (jet)	CO_2	94.65	iC_4H_{10}	4.7	C_3H_7OH	0.65		
ID (trigger)	Ar	70	CO_2	30				
TPC	Ar	80	CH_4	20				
OD	Ar	49.7	iC_4H_{10}	49	C_3H_7OH	1.3		
FCA	Ar	49	iC_4H_{10}	48.5	C_2H_5OH	2.5		
FCB	Ar	50			C_2H_6	48	C_2H_5OH	2
RIB	CH_4	75	C_2H_6	25				
RIF	C_2H_6	100						
HPC	Ar	80	CH_4	20				
HAC/MUS	CO_2	59	iC_4H_{10}	30	Ar	11		
MUB	Ar	84.6	CO_2	6.5	CH_4	8.9		
MUF	CO_2	68.3	Ar	15	iC_4H_{10}	15	C_3H_7OH	1.7

Table 3.1: The gases used by each DELPHI detector partition. In addition, argon and a hydrogen–argon mixture (7%/93%) are used for regeneration of the active copper purification columns; and nitrogen and carbon dioxide are used for cooling and purging. The RICH Fluids (C_6F_{14} liquid, C_5F_{12}/C_4F_{10} gas, and TMAE vapour) are supplied by a separate system, described briefly in section 3.2.5.

of a dangerous condition. Finally, the environment has to be monitored carefully for conditions, such as a high temperature, which could damage equipment or indicate burning electronics.

There are thousands of these quantities which require monitoring or control — far far too many to oversee manually. Hence the need for computer control.

3.2.2 General Features

Apart from the RICH fluids, all gases used in DELPHI, despite the different compositions required by differing detection techniques, are provided by a unified gas system, summarized in section 3.9.1. The gases used in the various detector partitions are summarized in table 3.1.

Most high voltages are supplied by the CAEN high voltage unit, described in section 3.3.1. When large numbers of stray particles are produced by LEP (i.e. while filling the machine), high voltages of a number of detector partitions have to be ramped to a lower value to prevent excessive currents due to large amounts of ionization. This is necessary for the Inner Detector, Time Projection Chamber (TPC), Outer Detector, forward tracking chambers, Barrel and Forward RICHes, barrel electromagnetic

calorimeter (HPC), Forward Muon Chambers, and STIC. Consequently, speed and reliability of ramping for these detector partitions is particularly important.

Except for the HPC, the voltages and currents of the Fastbus Data Acquisition crate power supplies are all monitored, and can be switched on or off under computer control. Most detector partitions provide similar monitoring and control for their front-end electronics.

Temperature monitoring inside the detector is performed by the DELPHI Slow Controls. In the electronics counting rooms, the environment (including rack temperatures) is monitored by the GSS system, summarized in section 3.9.2.

A summary of the general requirements for each detector partition is shown in the Elementary Process function columns of table 3.2 on page 63 and, in more detail, in table C.1 on pages 155–161. Specific details of each detector partition, as they relate to the Slow Controls, are given below.

3.2.3 Barrel Tracking Detectors

Vertex Detector (VD)

The VD requires a bias voltage of about 60 V, and detector cooling. The Slow Controls hardware is described in [88], although the dedicated VAX software described therein is now supplemented by standard Elementary Processes.

Monitoring of temperature is vital, both in order to prevent damage to the detectors due to overheating, and to keep track of temperature variations which can lead to movement and consequent degradation of the precise alignment. These movements relative to the Inner Detector are monitored both by capacitive probes [89][1] and by lasers.

[1] Until the end of 1993.

Inner Detector (ID)

The ID uses LeCroy power supplies to provide high voltages for the drift field (not sensitive to LEP conditions), the anodes, and the MWPC. They are controlled using RS232–C connected to the ID VAXstation (via a terminal server), where a special process emulates a G64 system controlling a CAEN. This allows standard VAX software to be used with only minor changes. For more precise measurement of the detector voltages than can be provided by the LeCroys, a digital voltmeter is used.

Time Projection Chamber (TPC)

Both drift field and sense wire high voltages (25.3 and 1.435 kV respectively) are provided by CAEN units. Only the sense wire voltages need to be lowered during LEP filling. Special modules are used to measure the current in each sector. High voltage channels are 'daisy-chained' together in the CAEN in such a way that if one channel trips, then all channels of the same polarity trip. Trips are minimized by automatically lowering the volts if the current becomes too high.

Due to the proximity of the heated Barrel RICH, the temperatures are monitored and, if they are too high, the preamplifiers are switched off.

Outer Detector (OD)

High voltages are required for the OD anode wires. Since the OD is attached to the outside of the heated Barrel RICH, the temperatures and positions of the planks are monitored to check that the alignment does not change.

3.2.4 Forward Tracking Chambers

The high voltage systems of both FCA and FCB provide automatic trip-recovery. When a channel trips (due to a large current being drawn by excessive ionization in the chamber), this system automatically ramps the channel up again (after a short delay to allow the chambers to recover). If this occurs repeatedly, then the system gives

up, leaving further action to the operator (who is kept informed via SMI and EMU).

In addition, the software ensures that ramping is always done in groups of channels so that there are no delays between the start of ramping for different channels within an endcap (FCA) or module (FCB).

These functions were implemented by changes to the standard Elementary Process, which treats all channels independently.

Special precautions are taken to prevent the possibility of significant voltage differences between the FCB wire planes, which are only 1 cm apart. The CAEN high voltage channel for each plane is daisy-chained with the others in the same module in such a way that if one channel trips, then they all trip.

Monitoring of the FCB preamplifier low voltages is required to maintain a balance between sufficient amplification of the signals and noise reduction.

3.2.5 Ring Imaging Cherenkov Counters (RICH)

The RICH fluids [90] (C_6F_{14} liquid, C_5F_{12}/C_4F_{10} gas, methane and ethane used as drift gases, and TMAE vapour) are supplied by a special system controlled by five Siemens process controllers, which perform the particularly careful control and monitoring required by these sensitive detectors. The radiator ultraviolet transparency is checked with a monochromator controlled by G64.

Barrel RICH (RIB)

The Barrel RICH gases are heated to 40°C. This allows the normally liquid C_5F_{12} to be used as a gas radiator, and a greater quantity of TMAE vapour to be present.[2] The temperature has to be controlled and monitored very carefully to prevent condensation of the TMAE by cooling, damage to the detector by overheating, or expansion or contraction which would destroy the detector alignment.

[2]The elevated temperature was originally intended to also allow a higher gas radiator pressure (which would otherwise condense), providing improved pion/kaon differentiation at intermediate momenta. However this option has been ruled out for mechanical reasons.

An 80 kV Heinzinger very high voltage unit (controlled, via an IEEE bus, by G64) provides the electric field to drift photoelectrons to multiwire proportional chambers (MWPC), which are supplied by CAEN units.

Forward RICH (RIF)

The Forward RICH uses C_4F_{10}, which has a lower boiling point than C_5F_{12}, as its gas radiator, and thus does not require the elevated temperature used in the barrel, considerably simplifying the Slow Controls. A 35 kV FUG very high voltage unit (controlled via a CAEN unit) provides the drift fields, and CAENs are used for the MWPCs. The temperatures of the gas radiator, drift gas, front-end electronics, and fastbus crates are monitored by G64s, which can cut the TMAE flow or crate power in the event of problems.

3.2.6 Calorimetry

High-density Projection Chamber (HPC)

Due to the fairly large number of HPC CAEN channels (144) and to particular features of the switching on/off procedure, special software has been developed for the high voltage control. This optimizes the time needed to ramp up the chambers' high voltages and performs extensive checks on the power supply hardware to ensure safe operation of the chambers.

Since energy and position measurements depend critically on the gas mixture, continuous monitoring of the drift velocity and chamber gain is performed on external drift tubes connected to the gas system [91]. These measurements are performed using CAMAC devices, which are then read out by a G64 acting as a crate controller.

Forward Electromagnetic Calorimeter (EMF)

All phototriode high voltages on each side of the EMF are supplied by a single Kepco high voltage unit. A splitter allows the voltage and current for each quadrant to be

individually controlled and monitored directly by G64, and the 2560 currents drawn by individual groups of phototriodes are also monitored. A water cooling system is employed and temperatures are monitored, allowing the detector to be automatically switched off if the temperature rises too high.

Hadron Calorimeter (HAC)

The high voltage [92] for each HAC tower is provided by a single CAEN channel, for which automatic trip-recovery is provided. Each of the 1872 layers can be disconnected separately by relay. This prevents a single short putting an entire tower out of action. To achieve this, the current drawn by each layer is monitored [93]; if it is too high, the relay is switched off directly by the G64 (for speed). The front-end electronics supplies are also controlled [94]. Test streamer tubes are used to monitor the gas mixture quality and drift velocity.

3.2.7 Muon Chambers

Both Barrel and Forward Muon Chamber high voltage control includes automatic trip-recovery, similar to that described for the Forward Tracking Chambers in section 3.2.4 (though without the form of channel grouping used there).

Barrel Muon Chambers (MUB)

The Barrel Muon Chambers' high voltages are applied to both the anode wires (6150 V) and the cathode (grading) strips (graded with voltage between 4000 V and ground). Hardware interlocks ensure that both anode and grading will trip if the current drawn by either is too large. The voltage difference between anode and grading is further protected by automatically ramping the voltages in 500 V steps. Special conditioning logic automatically comes into operation for sectors tripping repeatedly. This reduces, for a time, the target voltages to find a level where the chambers can operate without tripping. The voltages are ramped down if the gas supply is stopped or the mixture is bad (in addition to the general switch-off in the event of a gas loss).

Forward Muon Chambers (MUF)

The Forward Muon Chambers' anode wire voltages are provided by CAEN and the cathode strips by FUG power supplies, which are controlled directly by the G64s. The anode voltages are varied (by the Elementary Process) as a function of atmospheric pressure in order to maintain a constant efficiency. The drift velocity is monitored [95] with a special chamber supplied with the same gas mixture as the detector.

Surround Muon Chambers (MUS)

Since the MUS streamer tubes are of the same design as those of the Hadron Calorimeter, the same gas supply can be used for the two detectors. However, the smaller number of planes allows each one to be provided with high voltage by a single CAEN channel.

3.2.8 Scintillators

Scintillator Trigger Counters (SCI)

High voltages for the SCI photomultiplier tubes are provided by non-standard CAEN voltage dividers, controlled using the HPC G64 system and special VAX software.

Time of Flight Counters (TOF)

High voltages are used for the photomultiplier tubes.

Forward Scintillator Hodoscope (HOF)

The HOF Slow Controls are considered a subsystem of the Forward Muon Chambers (section 3.2.7), which provides high voltages for the photomultiplier tubes.

3.2.9 Luminosity Monitors

The Slow Controls of the SAT and VSAT are described in [97]. Bias voltages for both detector partitions are provided by special low voltage crates, which are connected via

RS232–C to a shared G64. The G64 Skeleton program and the Elementary Process have been adapted to control these bias channels. This system is also used for the bias voltages of the STIC, which replaced the SAT at the start of 1994.

Monitoring is performed on the currents drawn by each of the 320 STIC phototetrodes, which are supplied by a system based on that of the EMF (see section 3.2.6). Control is performed on each endcap as a whole: this is emulated in the G64 as a 2-channel CAEN crate. The veto hodoscope photomultiplier high voltages are provided by a CAEN SY403 high voltage unit, at present controlled by hardwired signals. The STIC fastbus monitoring and control are provided by the old SAT system.

3.2.10 Other Systems

Monitoring is also performed for the central Data Acquisition and Trigger system fastbus crate power supplies, temperatures at various places round the DELPHI barrel, cavern temperature and humidity, and the detector cooling water temperatures, flows, and vessel condition.

3.3 Front-end Systems (G64)

The lowest level of computer functionality (excepting intelligent devices such as the CAEN high voltage units described in section 3.3.1) is vested in the G64 systems. These are located in the electronics counting rooms adjacent to the detector in the experimental cavern. The number of G64s used by each detector partition is shown in table 3.2. A full list of G64s and Elementary Processes and a summary of their functions is given in table C.1 on pages 155–161. In total 88 G64 crates are used: 50 for the detector monitoring and control, 34 for the gas systems,[3] and 4 for the magnet.

[3]Of these, 7 (6 supervisors and one supply monitoring) are not included in table 3.2.

Partition	Number of G64s		Number of SC Elementary Processes					Comments
	SC	gas	HV	LV	temp	FB	other	
VD	2	–	–	2	1	1	–	
ID	1	3	1,2[m)]	1	1	1	–	High voltages supplied by LeCroy units and directly controlled by VAX processes which emulate G64s/CAENs.
TPC	7[p)]	3	1[p)]	2[p)]	1[p)]	2[p)]	2[p)]	
OD	2	2	1	1	1	1	–	
FCA	1[m)]	2	1[m)]	–	–	1	–	
FCB	2[m)]	3	2[m)]	1	–	2	–	
RIB	2,1;[m)] 5[p)]	1	2;[m)] 1[p)]	–	1[p)]	1	4[p)]	RICH fluids are overseen by five Siemens process controllers.
RIF	2,2[m)]	1	4	–	2	2	1[p)]	
HPC	2,4[p)]	3	1[p)]	1[p)]	1	1[p)]	2[p)]	
SCI	–	–	1[p)]	–	–	–	–	HPC G64/CAEN crates used.
EMF	2[p)]	–	2[p)]	2[p)]	2[p)]	2[p)]	–	
HAC	1,4;[m)] 1[p)]	4	4,4[m)]	4	–	1	3[p)]	
MUB	2	2	2[m)]	2	–	2	–	
MUF	2[m)]	3	2[m)]	2	–	2	–	
HOF	–	–	2[m)]	–	–	–	–	MUF G64/CAEN crates used.
MUS	1	–	2	–	–	–	–	HAC gas supplies used. LV and FB control to be implemented.
TOF	1	–	1	–	–	1	–	
SAT	1[m)]	–	–	1,1[m)]	1	1	–	The STIC replaced the SAT in 1994. SAT/STIC and VSAT bias G64 crates are shared.
STIC	1[m)]	–	3	1[m)]	1	1	1	
VSAT	–	–	–	1,1[m)]	–	1	–	
Sol	4[p)]	–	–	–	–	–	4[p)]	The Solenoid is described in section 3.9.3.
Misc	1	–	–	–	3	2	–	FCA G64 crate also used.
Total	54	27	39	23	15	25	17	

Table 3.2: A summary of the G64 crates and Elementary Processes used by each detector partition. The numbers of Slow Controls detector-monitoring (SC) and gas-system G64s are given, as well as the numbers of Elementary Processes for high voltages (HV), low voltage electronics (LV), temperature monitoring (temp), fastbus power supply monitoring (FB), and others.

[m)] indicates that the G64 Skeletons or VAX Elementary Processes (EP) have been modified (often only slightly) for functions specific to a particular detector partition.

[p)] indicates that partition-specific programs, not based on the G64 Skeleton or standard Elementary Process, are used.

Note that the gas-system G64s run a different program from the detector-monitoring G64s. The functions of the individual G64s and Elementary Processes enumerated here are detailed in table C.1 on pages 155–161.

Figure 3.2: The MAC–G64 and CAEN crates. The MAC–G64 crate (on top) consists of a G64 bus below a MAC bus. The G64 bus contains, from left to right, a double-card CAEN interface, two digital input/output cards, a G64–ethernet interface connected to thinwire ethernet, a CPU card with two RS232–C connectors, and a disk controller and drive. The MAC bus contains a double-card CAEN interface, two digital input/output adapters, and the power supplies on the right. Below the MAC–G64 crate is a CAEN high voltage crate, connected to the G64 by CAENnet.

3.3.1 G64 Hardware

G64 is a simple 64-line microprocessor bus developed by the Gespac company [98], though the term is often used to designate the entire computer system. Its simplicity has led to the production of a number of cheap input/output cards, and is thus well suited to an experiment, such as DELPHI, with a requirement to monitor and control a very large number of channels, without particular emphasis on speed.

The **MAC–G64** chassis [99], designed by CERN ECP division initially for ALEPH, has also been used by DELPHI (figure 3.2). It contains two card frames; the lower has a G64 bus, whilst the upper is used to hold the **MAC** (monitoring and control)

cards [100] which are tailored to specific input or output functions (such as multiplexing analog signals). These cards are read out using a small selection of G64 cards (typically analog-to-digital converter (ADC) and digital input/output cards) in the lower cardframe. This separation enables a small number of cards to be used for a variety of functions, simplifying the software and the maintenance of the hardware. In addition, the electrical separation of the MAC and G64 buses reduces noise problems by allowing the MAC cards to be separately grounded.

G64 cards

The G64 system was designed with the 6800-series of 8-bit microprocessors in mind. The CPU card [101] used by DELPHI includes the Motorola 6809E [102] microprocessor, 256 kilobytes of RAM, 32 kilobytes of ROM, two serial (RS232–C) interfaces, and a real-time clock. Peripherals on the G64 bus are memory-mapped, normally into a 1-kilobyte region, the Valid Peripheral Address space, which is decoded on the CPU card.

Since the 6809 has a 16-bit address bus, it can only directly address a maximum of 64 kilobytes. Additional memory (either RAM on the CPU card or RAM/EPROM on other G64 cards) can be addressed by using a paging facility on the CPU card, which allows, in our case, different 32-kilobyte sections of memory to be brought into use under program control.

Communication with the VAX systems is effected using a G64–ethernet interface [103]. This contains a 68000 processor, onboard RAM and EPROM, and the LANCE ethernet chip. The G64 CPU has access to a window of the 68000's RAM, and the 68000 can access all of the 6809's address space, allowing DMA transfers.

Two broad configurations of G64 cards have been used by DELPHI. 'Development' systems contain a CPU card, EPROM card containing parts of the operating system, floppy disk controller card and $3\frac{1}{2}''$ disk drive, ethernet card, and various input/output cards. Once the system is considered stable, the EPROMs are filled [104] with the application program and the floppy disk drive and controller are removed. This

'production' system can run with or without a terminal connection.

Input/Output cards

The main input/output G64 cards used are a Parallel Input Adapter (PIA) card for reading digital statuses, analog-to-digital converter (ADC) cards (10- and 12-bit resolution) for reading analog voltage levels, and an Output Register card to control digital states. The output register card is preferred to the PIA card for control, as all its outputs go to the same (off) state when the G64 crate is switched on or reset. Each ADC card has 16 channels; the digital input/output cards have 32.

Many of the required ranges accepted by the G64 input cards, or voltages produced by the output cards, are not suitable for direct connection to the detector. The conversion and electrical isolation is performed by the MAC cards: input adapters, relay cards, platinum resistance thermometer (PT100) temperature adapter cards, etc. Multiplexer cards, coupled with a PIA card, allow a single ADC channel to monitor 32 input voltages, albeit more slowly. The type of each MAC card can be read out by a special G64 card, allowing a crosscheck between program configuration and the actual hardware installed.

CAEN High Voltage Unit

Most high voltages required by DELPHI are provided by the CAEN SY127 system [80] (figure 3.2). Each crate can control up to 40 channels, divided into modules of 4 channels each. Different modules can be fitted for different channel characteristics, such as maximum voltage or current resolution.

The CAEN crates can be accessed by a front-panel keypad and LED display, by terminal (using a menu-driven system), or from the G64. Normal operation in DELPHI relies on the link to the G64, which is effected via a G64–CAEN interface and then CAENnet to the CAEN crate. CAENnet allows up to 100 crates to be daisy-chained together, allowing a total of 4000 channels to be controlled and monitored from a single G64–CAEN interface.

CAEN channels are normally maintained at a constant voltage (VO) unless the current drawn exceeds a preset limit (IO). In this case, the CAEN can be set either to trip (switch off) that channel immediately, or to enter a constant-current mode for a prespecified time before tripping (unless the load is reduced in the meantime). When voltages are changed, they ramp up or down at a preprogrammed rate. After the command to start ramping has been given, the CAEN is free to accept other commands for the same or different channels. All these parameters can be individually set or read (for each channel) from the G64. The channel statuses (i.e. whether on, off, tripped, etc.) and actual voltages (VMON) and currents (IMON) can also be read from the G64.

In the event of a computer failure, the operator can initiate a hardwired central ramp-down of all CAEN high voltages; this ramps the CAEN to an alternate set of voltages (preset to zero in the CAEN), and subsequently triggers a 'kill'.

3.3.2 G64 Software

System Software

The G64 'operating system' is extremely primitive, and contains no facilities for multitasking.

The 4 kilobyte **monitor** program in EPROM handles the initialization, and provides basic routines for terminal and disk input and output. When the system is switched on or reset, the monitor either bootstraps the operating system from disk (in the development systems) or loads the application program from EPROM.

The **FLEX** disk operating system [105] allows the editing, compilation, and running of programs from disk.

Most application programs for the G64 have been written in Omegasoft Pascal [106]. As well as standard Pascal features, this compiler allows the program to be split into separate modules, and allows direct addressing of memory-mapped peripherals.

The size of the DELPHI standard application program is considerably larger than the 64-kilobyte address space can hold. A mechanism has been developed to allow different modules of a program to be placed on different pages in memory, overcoming this problem [107]. Calls between Pascal routines on different pages are made in a transparent fashion.

Communications

Communications between the VAX and G64 systems [108] use the OSI transport protocol over ethernet (IEEE 802.3). The protocols are handled by the Marben Osiam product [109], running in the G64–ethernet card. An interface to this, CATS/TP4 [110], has been implemented on the G64–ethernet card, using the **CATS** (common access to transport service) calling standard developed at CERN [111]. CATS attempts to standardize calling sequences to different transport protocols and implementations. A simple protocol allows CATS calls on the G64 to be executed by CATS/TP4 on the G64–ethernet card, using the shared-memory window.

Remote Procedure Calls (RPC) [112] are used both on VAX and G64 to communicate commands and data. RPC is based on a client–server model, and allows network calls (i.e. calls to CATS) to be hidden from the application. The client application calls an application-defined routine, which is implemented on the server. The RPC system takes care of transmitting the request, along with the input parameters of the call, to the server. The server RPC system then calls the requested routine with the parameters decoded from the received message, and, upon its completion, sends back the return parameters to the client RPC system, which returns them as output parameters to the client application. RPC also handles the translation between different number representations, such as the different floating point representations used by the VAX and Omegasoft Pascal on the G64.

Application Program (G64 Skeleton)

Most G64 systems run a standard program, the **G64 Skeleton** [113], though a few use dedicated programs (marked [p)] in the *SC G64* column of table 3.2).

The G64 Skeleton, being at a low level and running on a comparatively slow computer, was designed for greatest simplicity. Essentially it tries to hide from the VAX the details of accessing the hardware, providing little 'intelligent' control, while at the same time minimizing the amount of communications necessary with the VAX.

Control and inquiry functions are implemented as remote procedures callable from the VAX (i.e. RPC with VAX as client, G64 as server). For efficiency, a single remote procedure call can read or set a number of channels if desired.

The G64 Skeleton executes a continuous program loop, monitoring all input channels. Any status change is flagged by calling a reporting routine on the VAX via RPC (i.e. G64 as client, VAX as server). Again, for the sake of efficiency, if the G64 detects several status changes within one monitoring loop, up to 10 of these are buffered into a single call.

The RPC/CATS/OSI connections are initiated from the VAX and repeatedly checked with application-watchdog messages from both sides.

A simple model of the hardware is presented to the VAX: channels are classified either as digital input, digital output, analog input, analog output, or CAEN. Except for CAEN channels, all values are represented as integers at this level: `0` or `1` for digital channels, or ADC counts (e.g. `0` to `1023` for a 10-bit ADC) for analog channels. Since the CAEN communicates voltages and currents in units of the resolution of the relevant module (whose type need not be known to the VAX), the G64 Skeleton program applies appropriate scale factors so that the VAX can use volts and microamperes for all CAEN channels, regardless of their type.

Digital and analog input channels are monitored continuously. The error status of analog channels is determined using a desired value and two error limits. If the monitored value differs from the desired value by more than the first error limit, then the channel goes into error. In order for the error to be cancelled, the value must

return to within the (narrower) second error limit. This hysteresis prevents frequent state changes when the value hovers around the limit. State changes in either direction (going into, or out of, error) cause a notification to be sent to the VAX.

CAEN channel statuses are monitored continuously, and any changes are reported to the VAX. While the actual voltages and currents are readable by command from the VAX, these are not continuously monitored by the G64, since any faults here will be signalled by the CAEN with a status change.

Digital *setting,* analog *setting,* and CAEN channel *settings* are only accessed by explicit initialization or changes requested from the VAX.

The channels to be monitored and their desired ranges are defined by RPC commands from the VAX. In addition, the G64 Skeleton program can be cleanly tailored for the few systems with special needs, such as those with special hardware or with a requirement for fast or particularly reliable intervention at the G64 level. (For example the Forward RICH stops TMAE flow immediately if the temperature drops below 25°C.) This allows most systems to be run from a standard EPROM, while maintaining flexibility.

3.4 VAX Systems

3.4.1 Hardware

The higher level control, overseeing, and logging is performed from various VAX systems in a single VAXcluster, located in the surface control room.

A VAX 6000 is used for the central Data Acquisition, a VAX 4000 for user access, and a VAXstation 4000 for the central Slow Controls. There are also a number of general-purpose VAXstations. In addition each major detector partition has one or two VAXstations (mostly VAXstation 4000s — 17 in all), which perform local Data Acquisition, monitoring, and Slow Controls. In this chapter, the term **VAX** is used to refer to any of these systems — they are all binary-compatible.

Ethernet is used for the connections between the VAXen, and for the link to the

detector G64s and front-end Data Acquisition crates in the cavern. However, the main (Fastbus) data flow between the cavern and the VAX 6000 on the surface goes via an optical link. An FDDI optical link is used to connect the DELPHI ethernet to the main CERN site, 7 km away.

3.4.2 VAX System Software

The **VMS** operating system is used. This provides multitasking, virtual memory, a networked filestore, and a rich set of system routines. From amongst them, the Slow Controls software has made heavy use of event flags, mailboxes, interrupts (VMS ASTs), global sections, and logical name translation services [114].

For communications with the G64s using the OSI protocols, the VOTS package was used at first. This has subsequently been merged with the native VMS networking system as DECnet Phase V. Except for the main dataflow, TCP/IP is used for communications between the VAXen and Fastbus Data Acquisition crates.

A variety of programming languages is used for the Slow Controls software. For its natural interfacing with VMS system services, and due to its familiarity to physicists, VAX/Fortran [115] — essentially Fortran 77 [116] with extensions such as structures — is used for the Elementary Processes, the error message display, and the databases. To allow a comparatively easy porting to the G64, we have benefitted from the implementation of the Remote Procedure Calls system in Pascal [117]. For its interfaces to X products, and familiarity to software engineers, C [118] is used for most of the software related to operator interaction and information exchange (HIPE, DUI, and DIM, which are described later). For its rich real-time and multithreaded capabilities, Ada [119] is used for the Error Message Utility and the State Management Interface. While this profusion of languages has had the disadvantage of compartmentalizing expertise, the definition of clear interfaces between the various systems has meant that in practice this has produced few problems.

Traditionally ASCII terminals have been used, and many of the user-interaction programs were originally written with a user interface based upon simple VT100-

style menus (using either VMS's SMG [120] or CERN's MHI [121] menu packages). More and more, however, the online programs are being converted to use the X-Windows/Motif [122, 123] graphical user interface. As well as allowing more detailed colour displays, there is no doubt that its use is more intuitively obvious for the operator. Since it can be used over the network (unlike many other graphical user interfaces), X-Windows allows experts to check up on many aspects of the detector operation without leaving the main CERN site, or even their foreign institutes. The disadvantage of this system is that it requires access to an X-terminal. For this reason many of the old ASCII-based user interfaces continue to be maintained in parallel.

3.5 VAX Monitoring and Control Programs

3.5.1 Elementary Process (EP)

G64s communicate with the Elementary Processes, which in general run in the detector partitions' VAXstations. Most Elementary Processes either use standard software or are closely based on it, and work with the G64 Skeleton program described in section 3.3.2. A few are dedicated programs (marked $^{p)}$ in the *Elementary Process* column of table 3.2), including those which handle the less standard applications. It is the standard program that will be described here.

Each elementary process oversees one subsystem of a detector partition, and is represented in SMI by a single object, whose state indicates the condition of that subsystem. For example, the temperatures on one side of the Hadron Calorimeter are monitored by one EP and are represented by one SMI state (indicating whether they are within an acceptable range).

The Elementary Process provides the connection between, on the one hand, the G64s and, on the other, the State Management Interface (SMI, described in more detail in section 3.8), the Error Message Utility (EMU, section 3.6), and the expert user interface (HIPE, section 3.5.2). It also updates the Status Update Database (section 3.7.2). These connections are represented diagrammatically in figure 3.1. In

order to handle interrupts from many of these sources, as well as to perform periodic monitoring, the EP is by necessity event driven, using the mechanism of VMS event flags [114].

Each Elementary Process communicates with one or more G64s, and each G64 can communicate with up to eight EPs (though each channel reports its status changes only to one EP). Thus an Elementary Process can control, monitor, and accept status changes for a large number of channels. Status change reports call an RPC routine as an interrupt (VMS AST level), allowing immediate timestamping and reporting to EMU. Other actions, such as recomputing the SMI state, are queued for subsequent execution. Analog values sent or received from the G64 can have a linear transformation applied to allow for conversion from the integer ADC count to the physical parameter being measured (e.g. temperature or voltage).

Channel definitions, normal settings, and conversion factors are read from the Slow Controls Configuration Database (section 3.7.1). This also defines names for each channel, to make any error messages (sent via EMU) helpful to the operator. The overall program configuration is defined by VMS logical names. 'Hooks' are provided in the code to allow for special requirements (e.g. the automatic trip-recovery used by the forward tracking and muon chambers, described in section 3.2.4[4]).

The Elementary Process can accept commands from, and report state changes to, SMI. At any time a single SMI state is evaluated to represent the status of all channels overseen by an Elementary Process: these states are listed in table 3.3 on page 82. SMI commands, which act on all relevant channels, perform actions such as switching apparatus on, off, or to an intermediate (standby) level (normally only used for high voltages).

State changes in each channel, reported by the G64, are sent to EMU. These generally indicate an error condition being either raised or cancelled, though computer problems, such as communication errors, also generate EMU messages.

[4]A general-purpose automatic trip-recovery system, drawing on experience from these modificaions, is now implemented in the standard Elementary Process.

Changes in channel statuses reported by the G64, and in parameter values determined by periodic monitoring are written onto the Status Update Database for use by the offline data analysis. Multiple changes occurring together (within a few seconds) are combined in order to reduce the number of updates to the same database record (timestamped according to the time of receipt from the G64). Database updates are usually inhibited when no data is being taken in order to minimize the number of updates due to the raising and lowering of the high voltages at the start and end of datataking. Outstanding changes are then written (backdated to their last change) when datataking commences. These updates are sufficient because the offline programs only require the detector status at the time of the events being analysed. Since this task is of lower priority than others, a block of database updates may be temporarily interrupted, for instance to respond to an operator command.

Special procedures are included for the CAEN. When a command to change the voltages is given, all parameters (ramping rates, etc., as well as voltage values) are downloaded from the Elementary Process to the G64 and thence to the CAEN. If defined in the configuration database, a special ramping current limit is used in order to prevent trips due to the higher currents drawn during ramping. When completion of the ramp is signalled by the G64, the normal current limit is downloaded. The Elementary Process also has to recognize CAEN crate-wide conditions, such as the disabling of high voltages by manual intervention.

3.5.2 Expert Interaction (HIPE)

Display and control of individual channels by detector experts can be effected via the Elementary Process using the HIPE [124] user interface (see figure 3.3). This allows, for example, high voltages to be adjusted for problem channels. At a command from HIPE, these modified values can then be written by the EP to the Slow Controls Configuration Database, to become the new standard values. HIPE uses a VMS global section to retrieve information directly from the EP's datastructures in memory. This keeps interactive access from interrupting the work of the Elementary Process, though

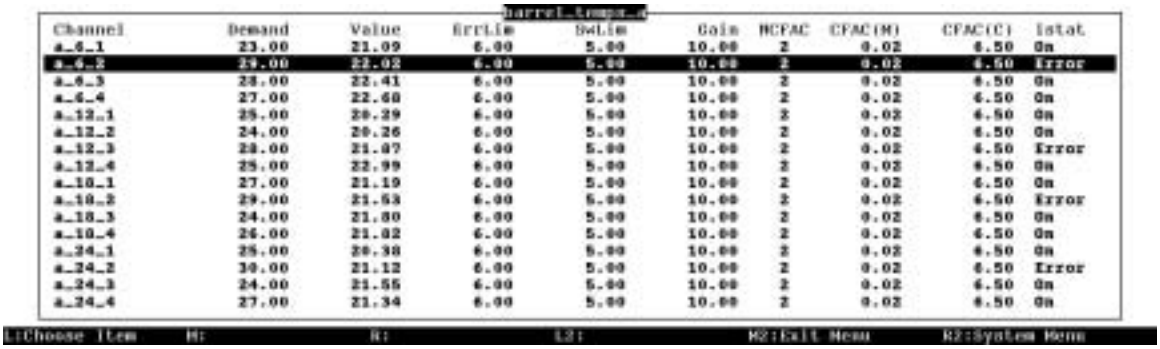

Figure 3.3: A typical screen from the HIPE Expert Display. Each row shows information for a single channel (it could also show a summary of a group of channels). In this case, some of the temperatures from the DELPHI environmental monitoring are shown. `Channel` gives the sensor name, `Demand` the nominal desired temperature, `Value` the actual monitored value, and `Istat` the channel status (i.e. whether it is in error — in this case a number of channel values are out of range, as the detector is switched off). Other monitoring parameters are also shown, and further details can be requested by selecting a channel.

commands (such as the adjustment of channels) can be left for the Elementary Process to perform when it is free.

HIPE user interaction is based on the MHI [121] menu package. The definition of the Elementary Processes to which HIPE must connect, the channels and groupings, and the menu structure is made by configuration file. Special channel types or requirements can usually be accommodated by changing the default menu structures.

3.6 Error Message Handling (EMU)

The Error Message Utility (EMU) [125] is a CERN product which provides a unified system for handling alarm, error, warning, and informational messages from the Slow Controls and Data Acquisition systems. Messages, which can be injected anywhere on the network, are formatted by the EMU system according to a message description file. They are then sent to one of a number of logfiles or destination processes according to a message routing file.

Application programs inject messages into EMU using a short message name (i.e. `set_error` or `clr_error`) and usually some parameters (e.g. the channel name).

The EMU system consists of three processes, which in DELPHI all run on the central

Slow Controls workstation, though in general they could each have many instances on different machines. The EMU DECnet server acts as an RPC server for the application programs, simply sending the messages without change via a mailbox to the EMU Decoder.

The Decoder attaches a **description** and **properties** to the message according to those listed in the message file for the given message name. The description will be used in the logfile and EMU display to clarify the message. The parameters sent by the application program are inserted at appropriate points to make an 'English' sentence. The properties are used for routing the message, and for selections by the EMU display (see section 3.6.2).

The Decoder passes the message on to the EMU Router, which decides where to send the message: into one of a number of logfiles, or on to an application process. The routing can be based upon the name, properties (as attached by the decoder), or source of the message, as specified by logical expressions given in the routing file for each destination.

3.6.1 Use of EMU in DELPHI

Each Elementary Process or Data Acquisition program injects messages into EMU. The standard EPs use a limited set of message names (and hence they all can be associated with a single message description file). The message parameters are used to send specific information such as the channel name or the newly-read value.

In order to allow the EMU display to match an error message with its cancellation, an additional convention is observed [126]. The message names start with `set` (for raising) or `clr` (for cancelling messages), and significant text (such as the channel name, which clearly must be the same if the two messages are to refer to the same condition) is enclosed in square brackets. If these, the injecting program, and some additional properties match, then the EMU display is able to remove the message from the list of outstanding errors when the cancellation message is received.

Each detector partition (or other system, such as the central gas system) has one

EMU logfile, which is normally only of interest to detector experts. All messages from that partition, or messages relevant to that partition from the gas or safety system, are sent to this logfile. Warning, error, and alarm messages are also sent into central logfiles (one for the Slow Controls and one for the Data Acquisition), which are watched by dedicated EMU displays on the operators' workstations. New versions of the logfiles are created every midnight, while the old versions are kept available for inspection by detector experts.

EMU messages corresponding to conditions that require rapid intervention from a detector expert are routed to a 'beep-caller' program [127]. This uses the auto-dial facility of a modem to dial the telephone number that activates the pager carried by the appropriate detector expert.

3.6.2 EMU Display

The EMU Display [128] is a general configurable utility for showing outstanding conditions reported by EMU. It is based on the X-Windows/Motif graphical user interface (figure 3.4), though a VT100-style terminal interface based on MHI is also provided.

The program watches for updates that EMU makes to a logfile (signalled by the VMS file system) and displays them according to category (e.g. by detector partition or severity), which may be selected for display separately. If not currently displayed, a new message is indicated by a colour change (according to its severity) on the button corresponding to its category. Cancelled messages are removed from the display, though they remain in the logfile. A logfile browsing facility is also provided.

In normal operation EMU displays are used by both Data Acquisition and Slow Controls operators to monitor warning, error, and alarm conditions.

The program is highly configurable (both by configuration file and interactively), allowing it also to be useful for detector experts to monitor or browse the partition-specific logfiles.

Figure 3.4: A typical screen from the EMU Display. On the left are the controls, with a button to select each partition's messages. Those that have unseen messages are coloured according to the highest severity of message. Above the controls are the messages for the Outer Detector (selected by clicking on the OD button). These show a number of trips of CAEN high voltage channels.

3.7 Databases

The DELPHI databases are based on the CARGO [129] hierarchical database system, which in turn uses a modified version of CERN's KAPACK [130] keyed-access file management routines.

CARGO provides facilities for creating, updating, and interrogating the database, either interactively or from a program. Its special features are the timestamping of updates to a record, and the ability to create a formatted **ASCII file**. Each update has a **period of validity**, which is usually from the time of the update until the next update. This allows an analysis program to read the data item that was valid at any past time, such as at the time that a particular physics event was recorded. The ASCII file contains a representation of all of, or a selected subset of, the binary database file. This is particularly convenient for the periodic transport of database updates from the online to the offline computers, which also use CARGO to store the detector calibration and alignment.

Each of the main CARGO databases used in the online system (Slow Controls

configuration, Slow Controls status update, and LEP machine parameters) has an **access package**, which provides a set of routines through which all database accesses are performed. Application programs can either call these routines directly to access a private database file, or can make a remote procedure call to a database server process to access the common database files. The use of RPC provides automatic protection against conflicts, such as two programs attempting to write to the same record at the same time, since the server executes only one command at a time. It also greatly simplifies the task of coordinating the export of update ASCII files to the offline computers, since all updates go through the same process.

3.7.1 Slow Controls Configuration Database

The Slow Controls Configuration Database [131] lists characteristics, physical addresses, default values and error limits for each channel associated with an Elementary Process. It also defines the correspondence between G64 channel number and the Status Update Database word or words where changes will be recorded, and the tolerance on the readings before an update is made.

Since updates to this database are only made at experts' request (normally only when the detector hardware or default running values are changed, i.e. via HIPE), it is usually found to be more convenient for each detector partition to have an individual database file.

3.7.2 Status Update Database

The Status Update Database [132] is used by the offline analysis to determine the state of the different parts of DELPHI as each physics event is analysed. The granularity of description depends on the detector partition concerned (see [96] for an example).

Updates are written by the Elementary Processes using the database server, called via RPC. These updates are periodically exported to the offline computers. During datataking, the frequency of updates from each detector partition is checked online

using time-development plots integrated into the quality checking system.

3.8 High-level Representation (SMI)

The State Management Interface (SMI) [133] describes the various subsystems of the experiment in terms of a set of **objects**.

Each object has a predefined set of **states** in which it can be, and for each state a set of allowable **actions** that can be requested of it. The state of each object is determined either by the state of other objects or, for **elementary objects**, by the state set in its associated Elementary Process. Similarly, actions requested of an object are either passed on to other objects or to an Elementary Process.

The definition of possible states, allowed actions, and the relationship between objects is made in a dedicated SMI language. In non-elementary objects it allows conditions to be specified which will result in an automatic state change or set of actions. For example, the state of a higher-level object can be determined by the states of lower-level objects, or commands can be issued when a state change occurs.

A group of related SMI objects forms an **SMI domain**, which is implemented in a single process. Communication between an SMI domain and other domains, or with the Elementary Processes or the user interfaces, is effected using the **DELPHI Information Management (DIM)** [134] system. This system allows SMI states to be directly viewable by the DELPHI User Interface (see section 3.8.2). It replaces SMI's native communication system [135], providing greater reliability, since it does not require all states to be held by a central server.

3.8.1 Use of SMI in DELPHI

SMI provides the primary high-level control and reporting mechanism for both the Slow Controls and Data Acquisition systems. Each detector partition is mapped onto an SMI domain, which contains an object for each Elementary Process, which oversees a single well-defined subsystem. Some of the possible states of these objects

and the actions that can be performed on them are listed in table 3.3. The states of all Elementary Objects in an SMI domain are combined into summary objects `SC` and, where relevant, `LEP_RELATED`.

The `SC` object gives the detector partition's overall status. Its states are summarized in table 3.4a.

Since LEP activity (such as injection or coarse tuning) can produce a significant number of stray particles in the detector, it is advisable to reduce the high voltages of the more sensitive partitions during this time. The `LEP_RELATED` object shows the state of these high voltages, and can be used to ensure that they are all lowered before giving LEP the go-ahead for the operation.

Conditions in the ancillary gas and GSS systems (see section 3.9) relevant to each detector partition are relayed to that partition's SMI domain and can be used to switch off voltages when a serious condition is indicated. They can also contribute to the partition's `SC` summary state, giving the possibility of an `ALARM` state.

The summary states for each detector partition are relayed to a central SMI domain, which composes overall `SC` and `LEP_RELATED` summary states for DELPHI.

The main commands used for the control of each detector partition are summarized in table 3.4b. These commands can be received by the partition from one of two sources: during data taking, they normally come from the central operator via the central SMI domain; during setting up, they (and other commands designed for the control of specific detector partitions) are issued by detector experts from a local SMI display. A switch from local to central control and vice versa is provided so that central switch-on commands can be inhibited during the intervention of detector experts.

3.8.2 SMI Display

Operator display and control is provided by the DELPHI user interface (DUI) [136] to SMI. DUI is a general-purpose X-Windows/Motif graphical user interface. It is used to show information as varied as the Slow Controls statuses and the LEP collimator

(a) SMI state	Condition
OFF	All channels are off.
HELD_OFF	Same as OFF, except that an explicit RELEASE command is required before any control is possible.
ON	All are on and OK.
STANDBY	All CAEN channels are at their intermediate level.
RUN	Same as ON, except that an explicit RELEASE command is required before any control is possible.
CHANGING	At least one channel is ramping up or down and at least one is above its STANDBY level.
CHANGING_LO	At least one CAEN channel is ramping up or down, and all are at or below their STANDBY levels.
ERROR	At least one channel is in error (e.g. reading outside limits or tripped CAEN channel) and at least one other CAEN channel is above its STANDBY level.
ERROR_LO	At least one channel is in error, and all CAEN channels are at or below their STANDBY level.
NOT_READY	No channels are ramping or tripped, but they are not all at the same stable state (e.g. some on and some off).
NO_CONTROL	No communications with the G64, or between G64 and CAEN.
DEAD	The Elementary Process is not running.

(b) SMI command	Action
START	Default settings from the Slow Controls Configuration Database are downloaded to the G64, and control channels are switched on.
STANDBY	Equivalent to START but sets intermediate values.
REPAIR	Equivalent to START/STANDBY but only for CAEN channels that have tripped.
STOP	Control channels are switched off.
MONITOR	Performs an additional read of all channel values.
HOLD	If the state is ON or OFF, inhibits further commands (either from SMI or HIPE). The SMI state goes to RUN or HELD_OFF.
RELEASE	Cancels the HOLD command.
ABORTIT	Tells the Elementary Process to commit suicide.

Table 3.3: SMI states (a) and commands (b) of the standard Elementary Process. These correspond to the states and commands of the associated object in the detector partition's SMI domain. For high voltage subsystems, the states STANDBY, CHANGING_LO, ERROR_LO, and OFF indicate that the volts are no higher than the standby level. The states of the LEP_RELATED object (ALLOW_BEAM_CT_DUMP_INJ, DISALLOW_CHANGE, etc.) are set according to the states of the high voltage objects.

(a) SMI state	Condition
READY	Everything is on and can take data.
NOT_READY	One or more subsystems is not ready to take data (e.g. at standby level).
ALARM	Unsafe condition (e.g. gas leak).
AL_CANCEL	A previous alarm condition, now gone, requires explicit clearing.
ERROR	One or more Elementary Objects is in ERROR.
CHANGING	High voltages are ramping up or down.
NO_CONTROL	No communications with one or more G64s or CAENs.
EP_DEAD	One or more Elementary Processes are not running.
DEAD	SMI domain is not running.

(b) SMI command	Action
Prepare_For_Run	All subsystems are STARTed to prepare for datataking.
Respond_To_Background	Lowers the voltages of subsystems which are sensitive to 'dirty' beam conditions.
Prepare_For_Dump	Lowers the voltages of subsystems which are sensitive to conditions following physics beam.
Prepare_For_Injection	Lowers the voltages of subsystems which are sensitive to the beam conditions which occur during LEP injection.
Prepare_For_Coarse_Tuning	Sets the voltages of subsystems which are sensitive to the beam conditions which occur during LEP coarse tuning.
Switch_On_Fastbus	Ensures that all Fastbus crate power supplies are switched on in preparation for datataking.
Prepare_For_Shutdown	Switches off all subsystems.
Clear_Cancelled_Alarms	Clears a previous alarm condition, now gone, subsequently allowing apparatus to be brought back into operation.
Set_Central	Switches the detector partition to central operator control.
Set_Local	Switches to local control.

Table 3.4: SMI states (a) and commands (b) of a typical detector partition summary object (SC).

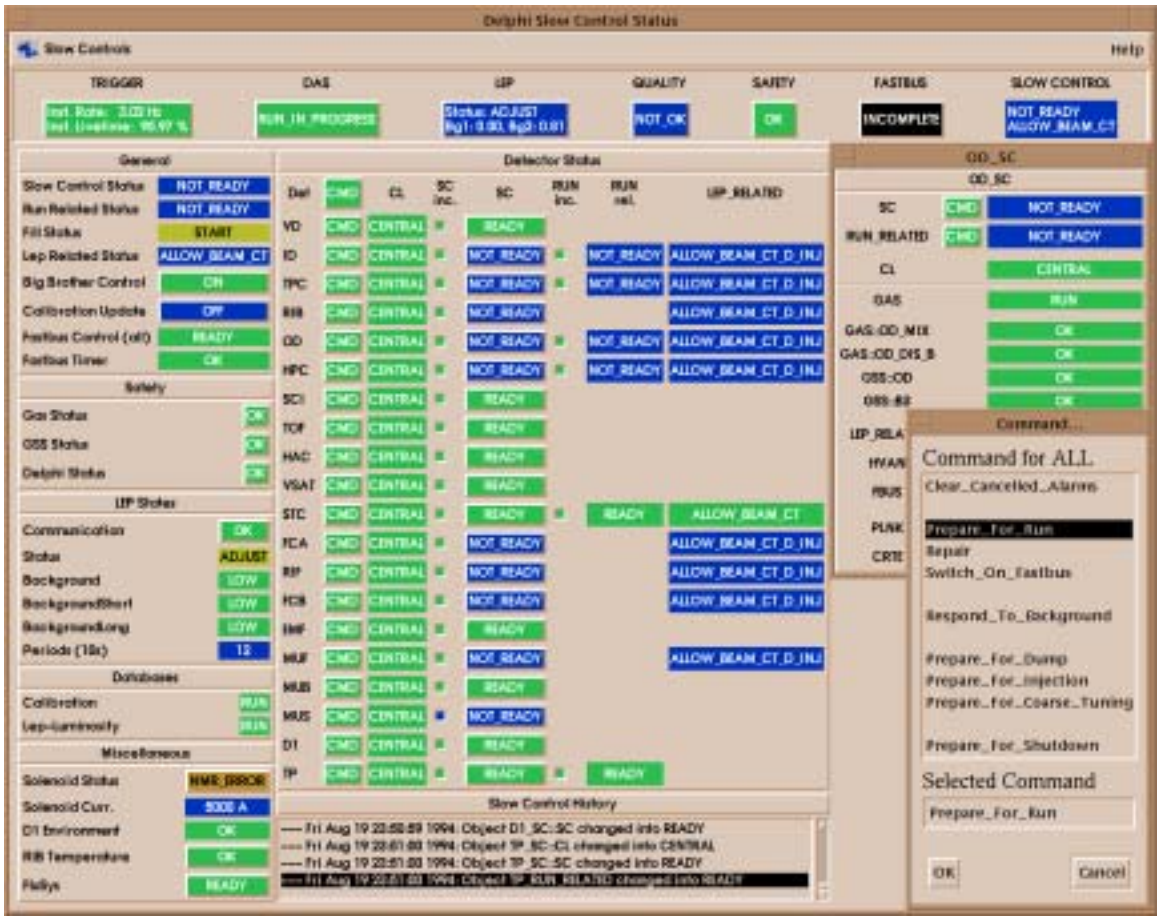

Figure 3.5: A typical screen from the SMI display. The LEP-sensitive high voltages are currently lowered (hence the states indicating that any LEP activity (beam coarse tuning, dump, or injection) is permitted). The local SMI for the Outer Detector (OD), obtained by selecting the `OD SC` button, is shown at the top right. The command menu for all detector partitions, obtained by selecting the top `CMD` button, is shown bottom right with the `Prepare_For_Run` command (see table 3.4b) selected.

positions. DUI interfaces naturally to SMI due to the latter's use of the DIM system.

The SMI display program may be used to inspect and, when necessary, issue commands to individual detector partitions by local operators, or to the whole of DELPHI by the central operator.

The central Slow Controls SMI display, shown in figure 3.5, allows the operator to see the summary states of the central SMI, of each of the detector partitions, and of various ancillary systems. Details of the component states of each partition or ancillary system can also be presented from this display; an example is also shown in figure 3.5. The display can be used to send commands to all or part of DELPHI, or (where authorized) to an individual object within a detector partition. The available

global commands are similar to those for an individual detector partition (table 3.4b); an example menu is also shown in figure 3.5.

A help facility is also available from the display to give advice to the operator on the diagnosis and cure of problems occurring in each detector partition.

3.8.3 Big Brother

After several years of operator experience, it was decided to further automate the system in order to provide the fastest-possible response to changes in the state of the LEP machine, Slow Controls, and Data Acquisition. This became possible once a reliable determination of the LEP machine condition was available to the DELPHI SMI [137]. It fitted smoothly into the existing software since the Data Acquisition controls are also based on SMI.

This system, dubbed Big Brother [138], was implemented entirely in SMI during the 1994 run. It introduces the following automatic actions based on correlations between the three hitherto independent systems.

- Once LEP acceleration is complete, and following confirmation from the Slow Controls operator, a `Prepare_For_Coarse_Tuning` command is issued to raise the STIC high voltages. This gives an additional measure of the background while the beams are adjusted.

- When the LEP collimators are closed, and an additional confirmation is provided by the Slow Controls operator, the remaining LEP-sensitive high voltages are raised with the `Prepare_For_Run` command.

- When all Slow Controls systems required for successful running are on, the Data Acquisition system is started.

- If any of these Slow Controls systems has a problem, the run is automatically paused. When the problem is resolved, the run is restarted.

- If the LEP backgrounds become too high, the run is paused. If they remain high for some time, then LEP-sensitive voltages are lowered with the `Respond_To_Background` command. When conditions are better and confirmation has been obtained from the SC operator, the volts are raised with `Prepare_For_Run`. Once enough are up, the run is restarted.

- After LEP dumps the beam or declares a machine development period, a `Prepare_For_Injection` command is issued to lower the high voltages.

In order to maximize the amount of usable data taken, the run is only paused for Slow Controls problems that would seriously impair the subsequent data reconstruction or analysis. Similar conditions are used at the start of a fill to determine when to start datataking. There are a number of conditions which, from the point of view of the Slow Controls, are considered errors (and yield, for example, an `ERROR` state) but for which datataking remains nonetheless profitable. In order to distinguish these cases, a set of `RUN_RELATED` SMI objects, in parallel to the ones described in section 3.8.1, are defined for the relevant detector partitions (ID, TPC, OD, HPC, STIC, and Trigger Partition). These can differ from the normal SMI states at the Elementary Process level (to distinguish, for example, a high voltage trip of a single wire from that of an entire sector) or at the detector SMI level (for example, temperature warnings, while requiring expert intervention, rarely affect or are affected by the state of the Data Acquisition, and so should not cause a pause of the run). The detector `RUN_RELATED` states can be excluded from the global `RUN_RELATED` state by the operator. This allows the run to be resumed if the error condition is determined to be less serious than the SMI state indicates.

As well as speeding detector operations (particularly when one of the operators is temporarily absent from the control room — for example performing checks in the cavern), with a consequent improvement in the overall datataking efficiency, this system has the additional advantage of standardizing the conditions that determine whether data is is taken.

Prerecorded, digitized, audio messages are used to keep the shift crew aware of Big Brother's actions, to request confirmation of high voltage increases, and to alert sleepy operators to serious problems such as safety alarms, high LEP backgrounds, or Slow Controls or Data Acquisition errors. Inevitably the controlling process has been called 'Big Sister'.

3.9 Ancillary Systems

The system described in sections 3.3–3.8 oversees and controls technical aspects of the detector and its readout electronics. However, it does not operate alone. The gas supplies, environmental monitoring for unsafe conditions (GSS), the solenoidal magnet, and the LEP machine have been developed independently of the detector Slow Controls system. In order to allow the Slow Controls operator easy access to the condition of these systems, and to allow automatic actions in serious situations, these systems have been interfaced with the DELPHI Slow Controls at the EMU (see section 3.6) and SMI (section 3.8) levels.

The gas and Solenoid control systems were developed within the DELPHI collaboration and both use a combination of G64 and VAX computers. However, in contrast to the detector control described in section 3.3.2, much more intelligence is vested in the G64s, while the VAX is used only for user interaction, logging, and interfacing with other systems. This has the advantage of allowing each system to operate independently. This was necessary as these systems were required before the rest of the detector controls were needed or implemented, and in any case could be run outside normal datataking periods when the other systems may be subject to frequent downtime. It did, however, lead to comparatively inflexible systems as program development on the G64 is painful, and (even using paged RAM) the program size is limited. Despite the different design philosophies, both these systems use the same G64 system software (FLEX, Pascal, etc.), the G64–ethernet card for communication with the OSI protocols, and (for the Solenoid) the RPC protocols.

The environmental surveillance and LEP monitoring systems were developed by independent groups at CERN and, like the gas and Solenoid monitoring, were interfaced *a posteriori* with the detector Slow Controls.

3.9.1 Gas Systems

All detector gases are provided by an integrated system of supplies, mixers, distributors, and purifiers [83], the state of which is monitored and controlled by 28 G64 systems. A further 6 G64s, which act as supervisors, are equipped with graphical displays and can control equipment and show the results of measurements throughout the system. The flow rates and compositions are carefully monitored, as anomalies could indicate a gas loss or a dangerous mixture.

Serious conditions are reported to a server on the VAX, which can set an `ALARM` SMI state for the parts of the detector affected, and injects an EMU message describing the problem for the operator. The `ALARM` state causes detector high voltages to be ramped down. This provides a backup to the hardwired connection directly from the gas system to the CAEN high voltage units.

An RPC server on the VAX is used to translate requests for information into commands for the gas system G64s. This facility is used to log the main gas parameters (as well as the atmospheric pressure) to the Status Update database. It is also used by certain detector partitions which base their high voltage control on the values of these parameters.

3.9.2 General Surveillance System (GSS)

The safe environment of all four LEP experiments is monitored independently by the General Surveillance System [84]. It monitors the ventilation, cooling water, temperatures, and flammable gas and smoke detectors. If problems are detected, it can alert the operator or the fire brigade; it can switch off gas supplies, high voltages, or mains power; and it can activate fire extinguishers. A graphical interface to GSS

is provided.

The DELPHI Slow Controls system is linked to GSS by both hardwired signals and computer messages. Hardwired signals are generated in the case of many serious conditions and are used to switch off high voltage and other potentially hazardous equipment independently of any decision made by the software systems. Conditions detected by GSS that are relevant to DELPHI are sent to a server process on the DELPHI VAXcluster, which translates them into EMU messages and maintains the state of SMI objects for each detector partition and electronics barrack. The SMI state changes can provoke automatic actions such as switching off high voltages, before the condition becomes serious enough to force a hardwired switch-off from GSS.

Hazardous conditions detected within DELPHI, such as a gas loss detected by the gas system, are forwarded from EMU to GSS. This allows GSS to take independent action, such as performing a hardwired switch-off of gas supplies and high voltages before the possibility of a buildup of flammable gas in the environment.

3.9.3 Solenoidal Magnet

The solenoidal magnet [50] produces a field of 1.2 tesla by using a superconducting coil carrying a current of 5000 A, maintained at a temperature of 4.5 K. Monitoring is required for the temperature, pressure in the cryostat, current, mechanical strain, and magnetic field in a number of places round the coil. Detailed computer control of the power supplies is required.

These functions are performed by four G64 systems: for the power supplies, vacuum systems, data logging, and NMR magnetic field measurement. A standalone VAXstation 4000–VLC provides user interfaces and logs the time-variation of monitored values onto an independent database (implemented with CARGO; see section 3.7).

Anomalous conditions detected by the G64 systems are sent to an alarm server on the VAX. A few of these conditions, for example a severe fault in the cooling system, can provoke automatic action, such as running down the magnet currents. All messages are injected into a local EMU system, which can forward the more serious

to the main cluster, thus notifying the Slow Controls operator in the usual manner.

3.9.4 LEP Accelerator

A typical LEP fill can last up to 24 hours, though background problems seen in the detectors may require intervention. During filling and high background conditions, when large numbers of stray particles can be thrown into DELPHI, the high voltages must be lowered for the Inner Detector, TPC, Outer Detector, forward tracking chambers (FCA, FCB), Barrel and Forward RICHes (RIB, RIF), barrel electromagnetic calorimeter (HPC), Forward Muon Chambers (MUF), and STIC.

Since 1994, these actions are performed automatically by Big Brother (see section 3.8.3). Prior to this it was necessary for all these interactions to be made by hand, with the Slow Controls operator lowering the high voltages when indicated by LEP conditions or planned actions, and keeping the LEP operators informed of the state of DELPHI's high voltages.

3.10 Operations

DELPHI is normally operated by three people, concerned, respectively, with the Data Acquisition, data quality, and Slow Controls. In addition to controlling the detector, the Slow Controls operator (or '**SC Maestro**') has official responsibility for the safety of the detector and personnel during her shift (functioning as shift leader in matters of safety, or **SLIMOS**), and performs periodic tours round the cavern and gas barracks. Continuous SLIMOS cover is required whenever flammable gases are present in the detector, even if LEP is not running at the time. The user interfaces available in the control room are the SMI, EMU, GSS, and gas supervisor displays.

3.10.1 Normal Operations

The SMI display (shown in figure 3.5) gives the primary indication of the state of each detector partition, allowing the operator to coordinate with LEP conditions.

At the start of a LEP fill, when beams are injected into the machine, the operator must ensure that high voltages of sensitive detector partitions are lowered (normally to their standby levels). This is indicated for each partition (and DELPHI as a whole) by the `LEP_RELATED` objects shown on the SMI display. When LEP declares 'physics' conditions (colliding beams with collimators closed to reduce background), the voltages must be raised in order to allow the detector to take data. When all the voltages have reached their required levels, the run may be started. This is indicated for each detector partition (and DELPHI as a whole) by the `SC` objects showing `READY`.

3.10.2 Dealing with Problems

Problems shown on the SMI display may be followed up using the help facility provided there (see section 3.8.2) and using more detailed information from EMU (figure 3.4) or HIPE (figure 3.3). These are typically detector equipment problems (e.g. high voltage channels tripping, which can often be cured by ramping up again), or safety-related problems reported by GSS or the gas system.

Safety-related conditions are indicated on the GSS or gas supervisor displays, as well as on the EMU display, and in addition alert the operator by telephone pager. Many alarm conditions provoke automatic actions, initially by software in a controlled manner via SMI (and hence also shown on the SMI display), and then, in the case of severe alarms, by hardwired actions such as turning off gas supplies or high voltages, or by cutting the power to part or all of DELPHI. Some of the less critical actions may be modified by the Slow Controls operator acknowledging the alarm.

3.11 Example

By way of an illustration of how the system works, we consider the operations performed over one LEP fill. This exemplifies all the components shown in figure 3.1 and their interrelations.

1. While particles are injected into the LEP ring, accelerated to 45 GeV per beam,

and the beams are adjusted for collisions, the high voltages of sensitive detector partitions (ID, TPC, RIB, OD, HPC, FCA, RIF, FCB, MUF, and STIC[5]) must remain lowered. Figure 3.5 shows the SMI display in this state. Once the collimators are closed, reducing the number of stray particles in the detector, and physics conditions are declared, the high voltages have to be raised in order to take data. This is only done if the background measured by DELPHI is acceptable; if it is not, the LEP operators are encouraged to improve the beam conditions.

2. The Slow Controls operator (or Big Brother, after confirmation from the Slow Controls operator) issues the global `Prepare_For_Run` command from the SMI display. This command is forwarded to each detector partition's SMI domain, but will only affect those partitions not already on (normally just those which were lowered for LEP setup) and under central control. Their Elementary Processes will be given the `START` SMI command.

3. This causes the EP to download the default running values to its G64s. For the high voltage EPs, the new voltages relayed by the G64s to the CAENs cause the channels to start ramping. This new state is detected by the G64, which reports it to the EP, which, in turn, reports its state to SMI as `CHANGING`.

4. This state is visible to the operator until all voltages for that detector partition reach their final values. Note that during this time, the EPs, G64s, and CAENs are not blocked, and can respond to other commands (for example to ramp down again if LEP has problems). As each CAEN channel reaches its final value, the new state is detected by the G64's monitoring loop, and reported to the EP. When all channels have come up, the EP sets the state of its associated SMI object to `ON`, and the detector partition's SMI becomes `READY`. When all partitions are ready, the central SMI shows `READY` and the Data Acquisition running may be started in order to collect data.

[5]The STIC can in fact be switched on after acceleration is complete, but before the collimators are closed. Doing this makes an additional measure of the background conditions available to the LEP and DELPHI operators.

During this run, we now imagine a trip of a single CAEN high voltage channel.

5. The anode high voltage for plank 10 of the Outer Detector (OD), normally held at 4400 V, is detected by the CAEN to be drawing more than the specified maximum current (50 μA; normally it might be expected to be drawing 15 μA). This could generate a separate `over-current` message, which would eventually be sent to EMU, but we assume at this point that the trip time is set to zero, so the channel trips immediately.

6. When the G64 next monitors this channel (normally within 10 seconds) by reading its status byte, it will notice the change. This prompts it to make a remote procedure call to the reporting routine in the Elementary Process defined for this channel, in this case `EP_OD_HVAN`.

7. This EP immediately sends an EMU message, `set_error`, with parameters giving the channel type ('`CAEN`'), channel name ('`Plank 10`'), physical address ('`G64 crate 0800300010ac, slot 1, chan 10`'), and current state ('`ramping down, over-current, tripped, off`'), which is formatted into a readable message like those shown in figure 3.4, and is sent to a partition-specific logfile and to the Slow Controls operator's EMU display. Since the channel name is unique for this EP, it is enclosed in square brackets to allow the EMU display to match it up with the cancelling message (see section 3.6.1).

8. The Elementary Process marks this channel as being in error. If the number of channels now in error passes a (partition-dependent) threshold, then the EP changes its associated SMI state to `ERROR` (assuming the other channels are at their full voltages; if they were at their standby values — but maybe still high enough to be prone to a trip — then the state would be `ERROR_LO`).

9. The change in the state of the high voltage object (`HVAN`) in the OD's SMI domain (`OD_SC`) causes the detector partition's summary state (`SC`) to go to `ERROR` (but

the LEP_RELATED state remains unchanged, since the other voltages remain at their previous values), and the DELPHI summary state changes to NOT_READY.

10. The change can also result in an update of the Status Update Database. Either the new status or the changed voltage (assumed to be zero after the trip) will be written. The details of the update depend upon definitions in the Slow Controls Configuration Database for the specific subsystem. The database update is important for the subsequent analysis of the data being taken. However, if the trip had occurred when physics data was not being taken then the database update would have been inhibited.

11. The Outer Detector high voltages make use of the EP's automatic trip recovery system, which will automatically try to restore the tripped channels, after a minute's delay (during which the SMI state will be shown as ERROR_WAITING). However if the channel trips more than three times (never staying on for longer than 10 minutes), the automatic procedure gives up and an SMI state of ERROR (along with an EMU message) warns the operator to contact a detector expert. All the parameters (in this case, 3 retries, 1 and 10 minute times) are configurable. Throughout this process, the operator is kept informed with EMU messages, and database updates are made to indicate the state of the high voltages at all times. To see what might happen next, we imagine that the three attempts to raise the high voltages failed.

12. The lack of voltage on Plank 10 will produce a reduction to zero in the efficiency of this part of the Outer Detector. If the problem were to go uncorrected for long enough, this would become statistically significant and be noticed by the data quality checker. Normally, however, the Slow Controls operator will see the trip on the SMI and EMU displays long before this occurs, and will be alerted to the change of SMI state by Big Sister. The problem could be due to an increase in LEP background (in which case many high voltages throughout DELPHI will probably have tripped) or a momentary spike in detector background. Once

the operator judges that it is safe to try to raise the voltage again, the SMI command `REPAIR` can be given from the central SMI display.

13. The `REPAIR` command is relayed via the Outer Detector SMI control object (`SC`) to the EP controlling the Outer Detector high voltage, which switches on Plank 10 (and any other tripped channels), resetting its voltage to the default values using a Remote Procedure Call to the routine in the G64 for setting CAEN values. (The `REPAIR` command is ignored for non-CAEN or untripped channels.) The channel starts ramping up. This change of status is reported back to the Elementary Process, which sets the SMI state to `CHANGING` (or `CHANGING_LO`). This change is reflected in the central SMI domain.

14. When the channel reaches its desired final voltage, that condition is reported to the EP, which generates an EMU message, `clr_error`, cancelling the initial report of the trip, and (if enough channels are now OK) sets the SMI state `ON` for object `HVAN`, and the detector partition state (`OD_SC`) goes to `READY`.

15. The new OK-status can be written to the Status Update Database, and (if required) a read of the actual voltage will be triggered so that this too can be written.

When finally we reach the sad time when the LEP beam currents are too low to give sufficient luminosity to make continued running worthwhile, LEP will either dump the beam or perform some machine studies, and the Data Acquisition run will be stopped.

16. Before filling starts again or LEP machine studies are started, the high voltages of the sensitive detector partitions must be lowered to their standby levels in an analogous manner to their raising at the start of the fill. This is done with the `Prepare_For_Injection` command,[6] issued either by Big Brother or the operator.

[6]Prior to the autumn of 1993 the high voltages were lowered before the beam was dumped using

17. After obtaining permission from the shift leader, the Slow Controls operator can now go and make some tea (if English) or get some coffee (otherwise) while she waits for LEP to prepare a new fill. Of course, as soon as the vending machine has delivered its elixir the operator returns immediately to her post to continue to watch for any problem with the detector or ancillary systems.

3.12 Experience

3.12.1 Particular Strengths of the System

Many advantages have stemmed from the design of the system in a highly modular fashion, with different subsystems on different platforms or in different processes, and with well-defined interfaces between them.

This modular construction renders the overall system robust against problems in any one area, so that a crash of a G64, an Elementary Process, or an SMI domain only affects those systems which it oversees. The levels above make the problem visible to the operator, allowing for a more rapid cure.

Modularity has allowed a general system to be designed and implemented for many different detector partitions, while still allowing certain parts of the system to be tailored to specific requirements with comparative ease. As we have seen, these modifications can be made at all levels: at the G64 level to cater for special hardware or for rapid reaction to specific changes; at the Elementary Process level to allow for special handling of the hardware, or to alter the determination of SMI states, EMU messages, or status updates to the database; and at the SMI level to allow for different actions during different phases of running and to amalgamate the states of detector partitions' subsystems in different ways.

Except for SMI, for which the SMI-language description for each detector partition

the `Prepare_For_Dump` command. We have since determined that the beam dump procedure does not produce any additional background radiation, so `Prepare_For_Dump` is now only used prior to a period of LEP machine development following a physics run.

has to be tailored for different sets of subsystems, the standard programs have proved sufficient for the majority of subsystems. This is due to the high level of configurability of most of the software.

As described in section 3.9, the modularity has also simplified the interfacing of the detector Slow Controls with the ancillary gas, GSS, Solenoid, and LEP systems.

The provision of such a modular system has been closely influenced and significantly helped by the adoption of the RPC communications and the SMI state-machine models (sections 3.3.2 and 3.8 respectively).

3.12.2 Problems and Solutions

The implementation of the system in the 'dirty' environment of DELPHI as compared to the development laboratory has resulted in previously underestimated difficulties due, for example, to problems with the heavily-loaded ethernet. In such circumstances, the importance of fast error recovery, robust programs that do not hang or crash if cooperating processes crash or restart, and good procedures for reconnecting them, becomes paramount.

A general problem of all monitoring systems is limiting spurious (and sometimes 'flooding') messages without ignoring important conditions. At various times, DELPHI has had particular problems with too frequent EMU messages or status updates to the database. When extreme, these can block the server processes against more important messages, and fill up the disks. No specific solution has yet been developed to suppress repetitive error messages for the Slow Controls, where a single problem can result in many error messages for all the affected channels. In these cases it would be preferable if all were combined into a single message. The database status update floods, which can also slow down the subsequent analysis programs, have been solved by allowing for the inhibition of updates when not taking data — the period when such updates are by far the most frequent and yet are not required. Due to this change, and improvements in the efficiency of both the EMU and database servers, floods of both types are now rarely a problem.

A related problem is how to deal cleanly with known problems that have been determined to be not serious, such as a faulty sensor. Obviously the long-term solution is to fix the underlying problem, but it is not always practicable to do this immediately. Detector channels can be disabled with HIPE (short-term) or within the Slow Controls configuration database (long-term); gas alarms can be inhibited; and GSS alarms acknowledged or inhibited. These temporary work-arounds require careful documentation and communication between detector experts and the operators, and can thus be subject to human error.

Since DELPHI was designed to operate over a period of more than ten years, it is important to maintain a base of expertise and supplies of spare equipment to last the lifetime of the experiment. This highlights the importance of choosing widely-used hardware and software, ensuring that support for these is maintained, and of carefully documenting systems produced within the collaboration.

3.12.3 Re-evaluation of Past Decisions and Possible Future Improvements

The near-inevitable consequence of working in a large collaboration of independent groups is that complete standardization does not always occur, even where this is technically possible. As described above, the system has been designed to minimize the impact of this fact of life. However, the long-term ease of maintenance, in particular, would be improved by reducing the number of such special systems to a minimum. In software, this can often be done by generalizing the standard software to handle these specific cases in a configurable way. In hardware, where, originally, reductions in cost favoured the adoption of a solution tailored to a particular part of the detector, it is often desirable to replace these systems with more standardized ones when funds become available.

The G64 system was widely adopted at CERN and elsewhere to provide monitoring and control of a large number of disparate channels at low cost. The G64–MAC systems

remain cost-effective, but the 6809 8-bit processors originally chosen for the system — although physically robust — are now to be regarded as archaic, and any similar Slow Controls system designed now would certainly use the 68000 family of 16-bit processors (for which CPU cards are available for G64, e.g. [139]).

3.13 Summary

The DELPHI Slow Controls system has been in operation since the LEP pilot run in August of 1989, though the system has been improved significantly since then, culminating in the system described in this chapter.[7] Over this time, as higher and higher level systems have been added, the Slow Controls system has taken over the functions previously performed manually by detector experts. Along with analogous improvements in the Data Acquisition system, this has reduced the number of people required on shift from around twenty to three, allowing detector experts more time to spend on physics analysis.

By the end of 1993, DELPHI had recorded the results of about two million Z^0-decays, as well as Bhabha events used to measure the luminosity. The automation of the Slow Controls system (particularly the reduction in high voltage ramping times at the start and end of LEP fills) has made a significant contribution to improving the efficiency (live-time) of datataking, which in 1993 reached an average of 90% over 1500 hours of datataking.[8]

[7] The majority of the improvements were in operation at the start of datataking in 1992.

[8] *Buy your Slow Controls system from DELPHI! Washes whiter than white!* (i.e. Whitewashes all known problems).

Chapter 4

A Measurement of the Mean B-Hadron Lifetime

Calvin You can't just turn on creativity like a faucet, you have to be in the right mood.
Hobbes What mood is that?
Calvin Last-minute panic.

Calvin and Hobbes, Bill Watterson

4.1 Overview of Method

This analysis uses data from electron–positron collisions at LEP with centre of mass energies at or near the Z^0 pole, recorded by the DELPHI detector. The detector is described in chapter 2. The data capture and its subsequent analysis common to all DELPHI measurements are detailed, respectively, in sections 2.10 and 2.11 and references therein.

From this reconstructed data, hadronic events were selected and $J/\psi \to \mu^+\mu^-$ candidates were searched for in these events. Initially, very loose J/ψ cuts were applied in order to provide samples of both signal and background candidates, as well as allowing for easier tuning of cuts later on. Detailed information on each of these candidates (both muon parameters and tagging information as well as the

reconstructed parameters of the putative J/ψ) was written to disk for interactive analysis.

By selecting candidates with reconstructed mass close to the J/ψ mass, $M_{J/\psi}$, a fairly pure sample of J/ψs was obtained. By parameterizing the distribution of reconstructed masses over a larger range, the purity of the signal sample was measured. Samples of events with the 'wrong' mass or charge were used to model the background in the signal sample.

Since the distance the J/ψ travels over its lifetime is negligible compared to our experimental resolution, the J/ψ decay point, measured from the crossing point of the two muons' (extrapolated) trajectories, was used to determine the J/ψ's production point. If this is significantly removed from the electron–positron collision point (coincident with the Z^0 decay point), the presence of a relatively long-lived intermediate in the decay chain is indicated. Assuming this is a B-hadron (see chapter 1) and that its momentum can be determined, estimates of the B decay times can be made. Their distribution should be near-exponential, but for the experimental resolution, after correcting for the background contamination. The expected similarity of the different B-hadron lifetimes allows us to assume a single exponential. The decay constant allows us to measure the mean lifetime of B-hadrons decaying to J/ψs. Any excess near zero decay time indicates the presence of J/ψs produced directly (or via short-lived intermediaries) from the Z^0 decay.

4.2 Analysis Program

All physics events recorded between 1992 and 1995 inclusive were studied. The vertex detector configuration was significantly different before 1991 (see section 2.3.1) and the data prior to 1992 has so far not been processed with more recent versions of the DELANA/DSTFIX reconstruction code. Since the additional statistics that could be gained by inclusion of these years is minimal (as can be seen from table 2.1), the 1990 and 1991 data (initially studied for this analysis) were not used.

The shortDST data, both real and simulated, were copied from the CERN Computer Centre robots onto 10 gigabyte DLT2000[1] tapes and transported to the Rutherford Appleton Laboratory, where the data were read into the Atlas Data Store.[2]

Three stages of J/ψ candidate selection were used: event preselection, J/ψ candidate reconstruction and n-tuple creation, and n-tuple analysis. The first two stages were performed together in batch jobs (each reading, typically, around one million events) running on the Rutherford Computing Department's Digital OpenVMS/Alpha service (a 4 processor DEC 7000). To process the shortDST datasets for 1992–5 means reading a total of $\sim$ 90 gigabytes (for the real data alone — not counting the simulated data), which typically takes several days.

Considerably longer processing times would have been required but for the use of event preselection. This uses information written to the shortDST event header, allowing hadronic event selection and initial lepton identification to be performed. Events that fail these cuts do not need to be further read into memory, significantly speeding the overall processing time. The hadronic event selections (performed entirely at the preselection stage) are described in section 4.2.1. The initial lepton identification merely requires two tracks to be identified as muons by any of the identification algorithms, and is thus guaranteed to select all events that pass subsequent cuts. Checks were performed by repeating the preselection procedure for small samples of events. Although minor discrepancies were found (and the bugs identified and reported to the shortDST production team for correction in subsequent processings), these fortunately did not affect the events selected by the combination of cuts used here.

Pairs of tracks, in events selected as hadronic, that pass the J/ψ candidate selections described in section 4.2.3 cause an entry to be written to disk (in n-tuple format) for subsequent analysis. Information on the event, the two selected tracks,

[1] digital linear tape

[2] The Atlas Data Store is a facility to store large amounts of data, logically accessed as tape volumes of user-specified size, independently of their physical location in the Atlas Centre robots. Data can be accessed from on-site or from anywhere in the United Kingdom via SuperJANET.

Year	1992	1993	1994	1995	Total
Processing version	92E2	93D2	94C2	95D2	
Integrated Luminosity (pb^{-1})	24.1	36.3	46.3	31.7	138.4
ShortDST data size (Gb)	16.5	16.8	36.6	20.2	90.1
Events on shortDST	2482495	2766589	5753343	3661917	14664344
Hadronic events	717880	721410	1416289	682448	3538027
Events after muon preselection	108437	104692	206324	101346	520799
Events with ≥ 1 candidate	9713	9175	19008	9477	47373
J/ψ candidates output	11684	10901	22988	11397	56970
Output n-tuple size (Mb)	3.7	3.5	7.4	3.7	18.3

Table 4.1: Initial J/ψ candidate selection statistics. The hadronic events are those passing the section 4.2.1 selections. It is comparable with the counts given in table 2.1, though the slightly higher numbers there reflect the very loose hadronic cuts performed in the online. The muon preselection (section 4.2) requires that the event have two or more muon-tagged tracks. The J/ψ candidates listed here are passed on for additional cuts, described in section 4.3

and the reconstructed putative J/ψ is saved (see section 4.2.5). By performing the candidate reconstruction at this stage and writing out only the information relevant to this analysis, the final candidate selection and analysis needs only ~ 18 megabytes of data, and can consequently be performed interactively. Table 4.1 summarizes the results of the event selections.

The same analysis program is used for simulated data, though additional information on the generated B, J/ψ, and muon parameters is also extracted [1, section 3.9]. Hadronic events are generated with the LUND Parton Shower (PS) Monte Carlo, JETSET 7.3, and the DELSIM detector simulation (see section 2.12). A B lifetime of 1.6 ps is used for all species of B-hadron. 7,082,380 hadronic (about twice the data sample) and 2,190,147 $b\bar{b}$ events were simulated (detector simulations for each of the four years, 1992–5, were used for different parts of the sample). Between them, these samples contained 3835 $B \to J/\psi \to \mu^+\mu^-$ events, but only 22 prompt $J/\psi \to \mu^+\mu^-$. A dedicated sample with a similar number of J/ψs helped with cross-checking, but was processed with an old version of the reconstruction software (93C without fixing), so was not used for detailed studies.

In fact the program that was developed for this analysis is considerably more general than this, a number of additional studies having been described in [1]. It

has options for using a variety of algorithms for lepton identification (electrons [1, section 3.6] as well as muons), charged track refitting (normally the shortDST track parameters are used without refit), jet assignment [1, section 6.2.3], charged + neutral energy summation, vertex fitting (e.g. mass-constrained fit [1, section 5.2]), as well as selecting different two-body ('V^0') decays ($K^0_S \to \pi^+\pi^-$ and $\Lambda^0 \to p\pi$). As well as muon identification and track reconstruction studies, these facilities were used to compare selections, check different DST and shortDST processings, and provide cross-checks of the candidate reconstruction. Other options can be used to search for some specific decay modes of the J/ψ parent: $\psi(2S) \to J/\psi\,\pi^+\pi^-$ and $\Lambda_b \to J/\psi\,\Lambda^0$ [1, chapter 5]. Finally, options are present to identify and work around bugs found (and reported!) in various prior and current DST and shortDST processings.

4.2.1 Event Selection

Standard 'open' hadronic cuts were used to select tracks and events as follows. For a charged particle track to be used, it was required to have

- momentum, $p \geq 0.1$ GeV/c,
- track length, $L \geq 30$ cm,
- transverse impact parameter, $|\epsilon| \leq 8$ cm,
- longitudinal impact parameter, $|z| \leq 8$ cm, and
- reconstructed energy uncertainty, $\mathrm{d}E/E \leq 100\%$,

where ϵ and z are two of the track's perigee parameters (defined in appendix B). These cuts are intended to reject tracks that were poorly reconstructed, from long-lived particle decays (e.g. K^0_L), or not from the primary vertex (e.g. cosmic rays or beam–gas events).

Hadronic Z^0 decays were selected with

- number of charged tracks, $N_{ch} \geq 5$,

- charged energy as a fraction of the LEP centre of mass energy, $E_{\mathrm{ch}}/E_{\mathrm{CMS}} \geq 10\%$, and

- thrust [141] axis z-component magnitude, $|\cos\theta_{\mathrm{thrust}}| \leq 0.95$.

All three event selections use only charged tracks as defined above. They remove, in turn, leptonic decays, two photon interactions, and events where a significant proportion of the tracks are likely to be lost down the beampipe. Distributions of these track and event selection parameters are shown in figure 4.1.

4.2.2 Muon Identification

Although only $(6.02 \pm 0.19)\%$ [2, page 41] of J/ψs decay to muons, these decays can be identified with high purity and reasonable efficiency. Decays to electrons (which occur just as often as decays to muons) can in principle also be identified. However, the lower electron identification efficiency of DELPHI, combined with the increased probability of significant energy loss from ionization and bremsstrahlung (which hinders reconstruction of the J/ψ mass) significantly reduces the efficiency of $\mathrm{J}/\psi \rightarrow \mathrm{e}^+\mathrm{e}^-$ selection. More critically, since in our subsequent analysis we are interested in the decay position, which requires accurate measurement of the tracks' position, the increased error in this measurement due to scattering of electrons conspires against a useful measurement in the $\mathrm{e}^+\mathrm{e}^-$ channel.

The standard set of MUFLAG muon identification algorithms (described in section 2.11.4), performed by DSTFIX and written to the shortDST, were used. It should be noted that the very loose tag was not intended for selection of muons in jets. However, in order to allow flexibility in choice of selection criteria at a later stage, candidates where one track was identified by only the very loose tag were included in this initial selection.

As noted in section 2.11.4, there is no coverage by the barrel and forward muon chambers (MUB and MUF) in the region $42^\circ < \theta < 52^\circ$. The surround muon chambers (MUS) which bridge this gap were not fully operational until the end of 1994 (partially

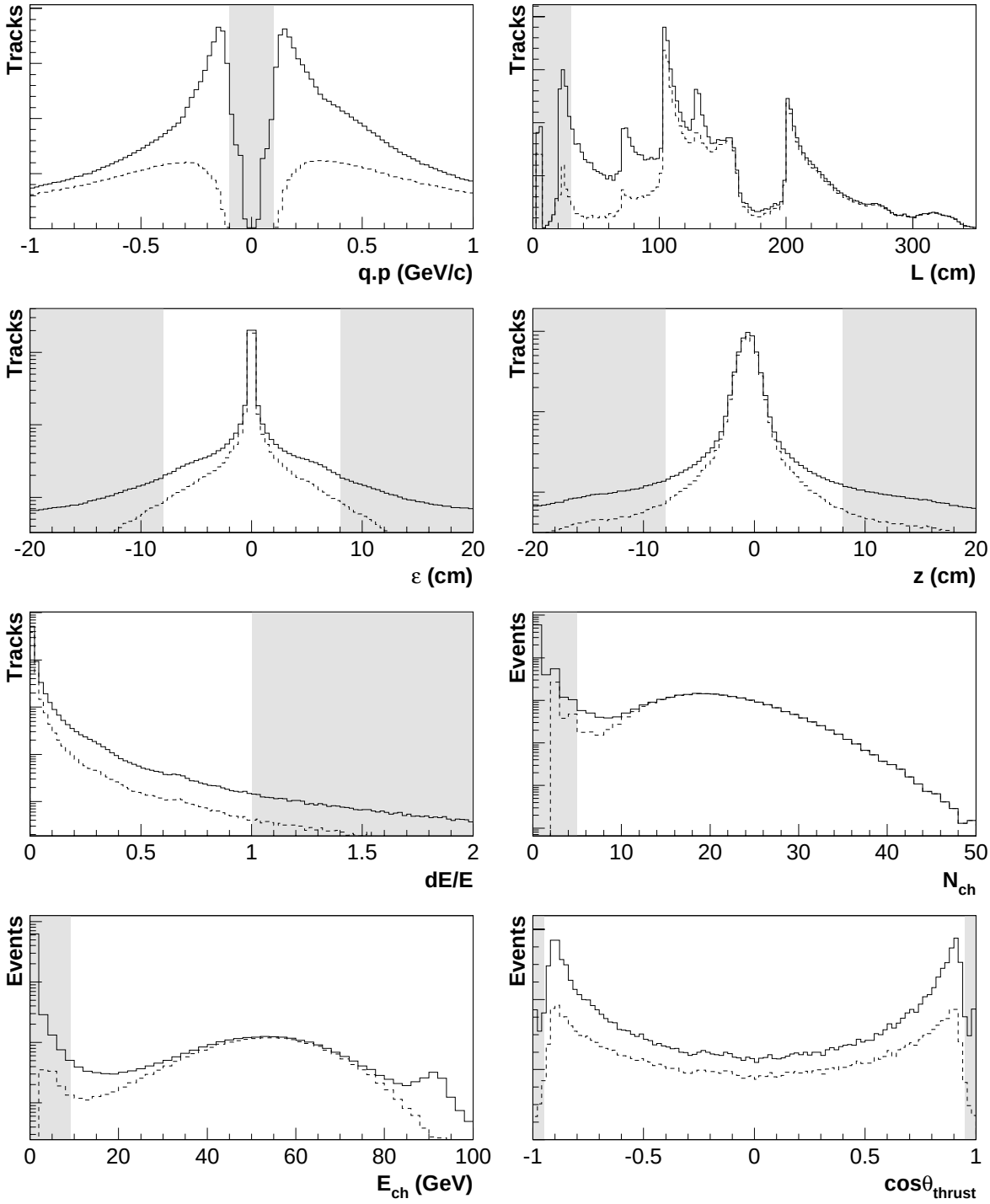

Figure 4.1: Distribution of parameters used in the hadronic event selection. The shaded regions show the cuts detailed in section 4.2.1.
The first five histograms show particle momenta (with charge sign; qp), track lengths (L), transverse and longitudinal impact parameters relative to the origin (ϵ and z), and energy measurement errors ($\mathrm{d}E/E$). The solid lines show all 7.4×10^6 reconstructed charged tracks in a sample of 951807 shortDST events (1994 DST OR stream). The dashed lines show tracks in hadronic events passing the other variables' cuts.
The remaining three histograms show the charged track multiplicity (N_{ch}), the total energy from charged tracks (E_{ch}), and thrust axis z-component ($\cos\theta_{\mathrm{thrust}}$), calculated using the selected tracks. The solid lines are for all events, while the dashed lines are only for events that passed the other hadronic cuts.
The number of tracks in the ϵ, z, and $\mathrm{d}E/E$ plots; and events in the N_{ch} and E_{ch} plots are shown on a log scale.

for $\sim 40\%$ of the 1994 data, fully for $\sim 25\%$) and DAS problems prevented them being read out in 1995, so we have full coverage for only $\sim 10\%$ of events. They are, however, used when available.

One final tag, PXHAID, uses the Hadron Calorimeter (HAC) which, while less efficient, has no gap in coverage between the barrel and endcap. Unfortunately, unlike the muon chamber algorithms which have been continuously developed to take account of changes in the detector and reconstruction, PXHAID has not been tuned since 1992, probably because it is poorly modelled by the simulation and so is not widely used. Nevertheless, again for flexibility, candidates that are selected by PXHAID are included in the initial selection. Studies of its performance on 1991–2 data are described in [1, section 3.5].

4.2.3 Initial J/ψ Candidate Selection

Pairs of charged tracks passing the section 4.2.1 cuts, that are identified as muons by at least one of the muon identification algorithms (see sections 2.11.4 and 4.2.2), are considered as J/ψ candidates. However candidates where both tracks are identified as muons by only the very loose tag are rejected.

A vertex fit is performed for each of the remaining candidates (see section 4.2.4), and the track parameters are adjusted accordingly. Candidates are selected according to

- $\mu^+\mu^-$ opening angle, $\omega \leq 90°$, and
- reconstructed parent (putative J/ψ) mass, $M_{\mu\mu} \geq 1.5$ GeV/c^2.

The opening angle ($\cos\omega \equiv \hat{\mathbf{p}}_{\mu^+} \cdot \hat{\mathbf{p}}_{\mu^-}$) cut removes muons from opposite jets (e.g. $Z^0 \to b\bar{b}$ with both B-hadrons decaying semileptonically) with, says the Monte Carlo, negligible loss of J/ψs.

The number of background events falls near-exponentially with $M_{\mu\mu}$. The $M_{\mu\mu}$ cut was chosen to remove the majority of the background, while leaving a reasonable range of masses for background estimation. Obviously any true J/ψs (for which we

hope for $M_{\mu\mu}$ close to $M_{\mathrm{J}/\psi} \approx 3.1$ GeV/c^2) removed by this cut are much too poorly measured to be of any use.

All candidates so selected are written to disk. Distributions of $M_{\mu\mu}$ and ω are shown in figures 4.2 and 4.3. For simulated events, true J/ψs are written (flagged) even if they are not selected.

4.2.4 Vertex Reconstruction

The track parameters of the two muon candidates are used to reconstruct the parameters of their parent. If both particles do in fact come from the same parent and they have no other siblings, the distribution of reconstructed masses should give a peak around the parent's true mass. Other combinations produce a continuous background.

The DELPHI-standard `PXFVTX` routine [142] is used to fit a vertex from the track perigee parameters, $(\epsilon, z, \theta, \phi, \kappa)$ (see appendix B). In order to allow for the curvature of the track between its perigee to the origin (the initial perigee parameters' reference point) and the vertex position, the fit is iterated, each time relative to the previously fitted vertex position. The iteration normally terminates when the last change in vertex position is less than 100 μm. Typically a couple of iterations are sufficient.

With two tracks, this three-dimensional fit has one degree of freedom, which can be thought of as the requirement that the two tracks have the same z-coordinate at their xy crossing point. Since the tracks' trajectories are measured at some distance from the vertex position (expressed as correlations between their position and trajectory at the vertex), the vertex constraint can in principle improve the trajectory measurement. However, it should be noted that with the single-sided vertex detector (i.e. prior to 1994) which only measured the azimuthal coordinate, the z-coordinate is relatively poorly measured and so the vertex fit constraint is rather weak.

This procedure gives a fitted vertex position, (x, y, z), and particle momenta at this point, (θ, ϕ, κ), as well as covariance matrices for these parameters. The track parameters are updated with these new values. The parent's parameters and their

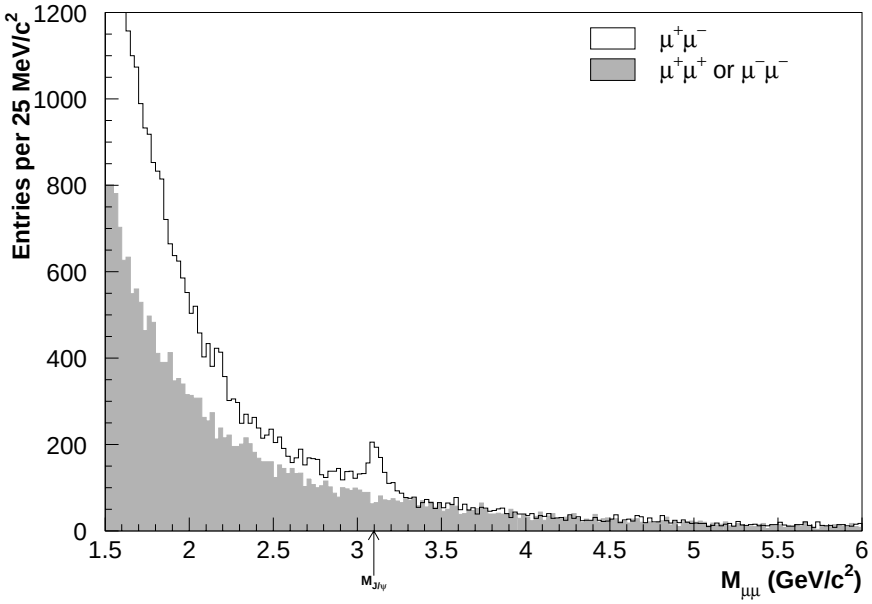

Figure 4.2: Reconstructed masses of all J/ψ candidates passing the initial cuts (1992–5). Candidates with like-signed (shaded histogram) and unlike-signed (unshaded) track charges are shown. The signal at $M_{J/\psi} \approx 3.1$ GeV/c^2 can already be seen (corresponding to 472 ± 29 J/ψs or $(27.7 \pm 1.7)\%$ of the candidates in $2.95 \leq M_{\mu^+\mu^-} < 3.25$ GeV/c^2).

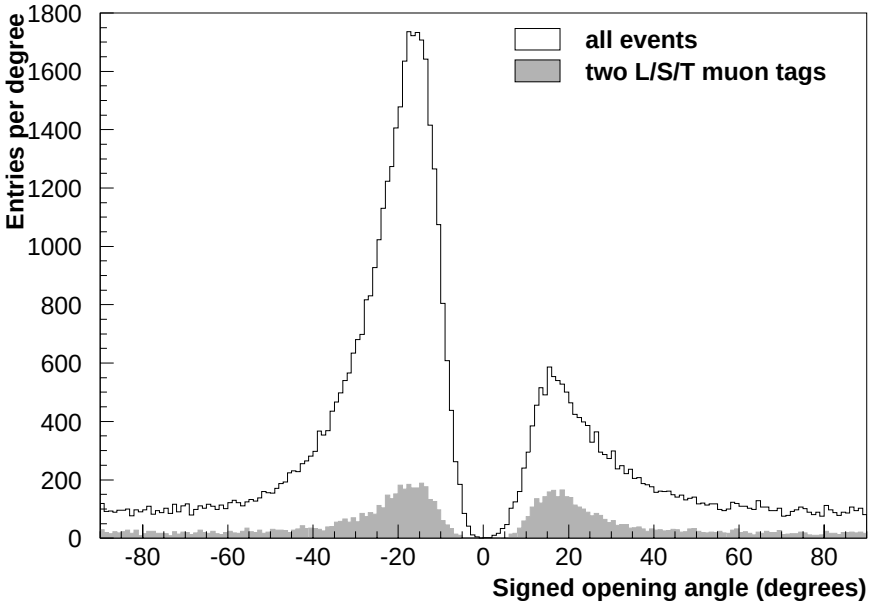

Figure 4.3: $\mu\mu$ opening angle for all J/ψ candidates passing the initial cuts (1992–5), signed according to the topology of the muons: 'cowboys' (where the effect of the magnetic field is to bend the tracks towards each other in the xy plane) have $\omega < 0$, and 'sailors' (tracks bent away from each other) have $\omega > 0$ (see the description of `OANGF` in section 4.2.5). The shaded histogram shows the subset of candidates where both tracks were selected by the loose, standard, or tight muon tags. The remainder had at least one track identified only by the Hadron Calorimeter or very loose muon tags. The clear asymmetry in this latter sample is well-described by the Monte Carlo.

errors are then calculated, ignoring the effect of track–track correlations.[3] This is done by converting the geometric track parameters, (θ, ϕ, κ), (and their 3-by-3 covariance matrices) to Cartesian four-momenta, (p_x, p_y, p_z, E), (and 4-by-4 covariance matrices). The muon mass (with zero error) is assumed for both particles. Then applying energy and momentum conservation, the parent's four-momentum (and its error matrix) is just the sum of that of the daughters. Finally the mass, momentum, and azimuthal direction (and errors) of the parent are calculated.[4]

The vertex position gives the putative J/ψ production point. The primary vertex position is estimated from the beamspot position (see section 2.11.3) and the decay position relative to this is calculated. The errors on the relative decay coordinates are quadrature-sums of the vertex reconstruction error, the beamspot size, and the uncertainty in the beamspot centre.

4.2.5 Intermediate Candidate Parameters

Candidates passing the initial selections described above are written to disk in 'row-wise' n-tuple [144] format. This allows the interactive study of derived variables (e.g. various decay time determinations) and complex cuts (e.g. combinations of cuts on many variables) without the need to reread the entire shortDST dataset each time. To allow for detailed crosschecks to be made on the analysis methods and code, and also to allow for flexibility in the choice of selection criteria and measurement variables, many more variables than were eventually used in this analysis were written. The variables written to the n-tuple are as follows:

[3] By constraining the two tracks to go through the same point, the errors on the two particles' momenta become correlated. In principle this should be taken into account when combining them to form the errors on the parent's mass and momentum. A procedure for using the track–track correlations was developed. Since the change in the calculated errors turned out to be small ($\sim 3\%$ on the $M_{\mu\mu}$ error) and not noticeably better, for simplicity this procedure was disabled.

[4] Routines developed for this analysis are now part of the DELPHI-standard DSTANA library [143]. They allow one to iterate over the vertex fit (`VDF2ND`), convert the track parameters to Cartesians (`VDPE2E`), calculate the parent's parameters (`REC2ND`), and from them its mass, momentum, and direction (`VDMPER`). Although only two daughters of equal mass are considered in this analysis, the code allows for an arbitrary number of tracks with individually assigned masses. At each stage the parameter errors are calculated, along with their correlations (though only optionally for the track–track correlations).

Event Variables.

`RUN` run number

`EVT` event number

`BEAM` beam energy

`TAPE` input tape identifier

`BSX` beamspot x-coordinate

`BSY` beamspot y-coordinate

`BSZ` beamspot z-coordinate

`JTHE` polar angle of the jet containing the two candidate tracks, $\theta_{\rm jet}$

`JPHI` azimuthal angle of the jet, $\phi_{\rm jet}$

`ENE1` charged + neutral energy in the sphericity [141] hemisphere containing this candidate (zero if daughters are in different hemispheres)

`ENE2` hemisphere energy (`ENE1`) after applying 4-momentum conservation constraint

`NUMB` candidate number in this event (in decreasing order of `MF`). `NUMB`=0 for a Monte Carlo generated J/ψ that was not reconstructed or did not pass the initial candidate cuts.

`Q` charge sum of the two daughters (e.g. `Q`=0 for $\mu^+\mu^-$)

`RSEL` run selection flag (specifies operational detector components)

Track variables. The following variables (`EPS1` etc.) are for track 1. They are repeated for track 2 (`EPS2` etc.). Track 1 is taken as the one with the higher tag (`TAG1` below) or, if they are equal, with the higher momentum (|`P1`|).

`EPS1` signed impact parameter with respect to beamspot, ϵ

`THE1` track direction polar angle, θ

`PHI1` track direction azimuthal angle, ϕ (at perigee to beamspot)

`P1` particle momentum, signed with the charge

`CHI1` muon chamber total χ^2 per degree of freedom

`HIT1` muon chamber hit pattern (with bit 8=MUF, bit 9=MUF, else MUS)

`MSC1` DELANA particle-id mass code

`NVD1` number of VD hits associated with track

`TAG1` muon selection flag. Each bit indicates whether a tag has selected this track as a muon.

bit 0 very loose

bit 1 Hadron Calorimeter (PXHAID)

bit 2 loose

bit 3 standard

bit 4 tight

`AMB1` track shortDST mass ambiguity code

Reconstructed parameters of the putative J/ψ**.** These parameters are from the standard vertex fit described in section 4.2.4. The results of other vertex fit options (e.g. 2D unconstrained, or mass-constrained) can be stored in the same format with names ending in `B` or `P` rather than the `F` used here.

`MF` mass, $M_{\mu\mu}$

`PF` momentum, $p_{\mu\mu}$

`PTHEF` polar angle of momentum vector, $\theta_{\mathrm{J}/\psi}$

`PPHIF` azimuthal angle of momentum vector, $\phi_{\mathrm{J}/\psi}$

`CTHEF` μ^+ polar angle in the J/ψ CMS, $\theta^*_{\mu^+}$

`CPHIF` μ^+ azimuthal angle in the J/ψ CMS, $\phi^*_{\mu^+}$

`OANGF` opening angle, ω, with the sign of the z-component of $\mathbf{p}_{\mu^+} \times \mathbf{p}_{\mu^-}$.[5] I.e. 'cowboys' have `OANGF` < 0 and 'sailors' `OANGF` > 0.

`PANGF` pointing angle (angle between the momentum and decay vectors) in the xy plane, $\zeta \equiv \phi_{\mathrm{J}/\psi} - \phi_V$ $(-\pi < \zeta \leq \pi)$

`LXYF` decay length from the beamspot in the xy plane, l_{xy}. A negative sign is assigned if the decay point is behind beamspot position with respect to the J/ψ momentum direction, $\phi_{\mathrm{J}/\psi}$ (i.e. `LXYF` has the sign of $\cos\zeta$).

`LZF` z-coordinate of vertex relative to the beamspot

`CHIFF` fit χ^2. If the fit failed, `CHIFF` < 0 and the number gives an error code.

`MEF` error on mass, $\mathrm{d}M_{\mu\mu}$

`PEF` error on momentum, $\mathrm{d}p_{\mu\mu}$

`PANEF` error on pointing angle, $\mathrm{d}\zeta$ (includes the effect of the beamspot size)

`LXYEF` error on xy decay length, $\mathrm{d}l_{xy}$ (includes the effect of the beamspot size)

Monte Carlo truth information. These variables are calculated from the particles' generated parameters. This set of variables and those that follow are only written out for simulated events.

`EVTM` Monte Carlo event type (a code specifying the 'most interesting' decay chain in the event, as specified in `MC1` and `MC2`). To this is added 10000× the initial state code (e.g. flavour of $\mathrm{q\bar{q}}$).

`JTHM`, `JPHM`, `QM`

parameters analogous to `JTHE`, `JPHI`, and `Q`, but calculated using the true track parameters

`ENEM1` charged + neutral energy in the sphericity hemisphere containing this candidate (zero if daughters are in different hemispheres)

[5] Actually $\mathbf{p}_{\mathrm{S}} \times \mathbf{p}_{\mathrm{L}}$ is used, where $\mathbf{p}_{\mathrm{S}}$ ($\mathbf{p}_{\mathrm{L}}$) is the momentum of the track with the smaller (larger) geometric curvature ($-qB/p_{xy}$) in the magnetic field. This definition works for both like- and unlike-sign candidates.

ENEM2 charged + neutral energy in the other hemisphere

Generated parameters of selected tracks. The following variables (MC1 etc.) are for track 1. They are repeated for track 2 (MC2 etc.).

MC1 code (same encoding as EVTM) specifying the particle's type and the decay chain that produced it.

EPSM1, THEM1, PHIM1, PM1

parameters analogous to EPS1, THE1, etc., but specifying the true track parameters.

Generated candidate parameters.

MM, PM, PTHEM, PPHIM, CTHEM, CPHIM, OANGM, PANGM, LXYM, LZM

parameters analogous to MF, PF, etc., but calculated using the true track parameters and primary vertex position (as opposed to the beamspot).

MCERR error code for simulation parameters' determination

Grandparent's true parameters (e.g. of the B for $B \to J/\psi$).

MMB mass, M_B

PMB momentum, p_B

PTHEMB polar angle, θ_B

PPHIMB azimuthal angle, ϕ_B

All variables are stored in REAL format (even integers and bit masks). Energy, momentum, mass, charge, distance, and angle are specified in units of GeV, GeV/c, GeV/c^2, e, cm, and radians ($0 \leq \theta < \pi$ or $0 \leq \phi < 2\pi$), respectively.

The following analysis was performed using these variables.

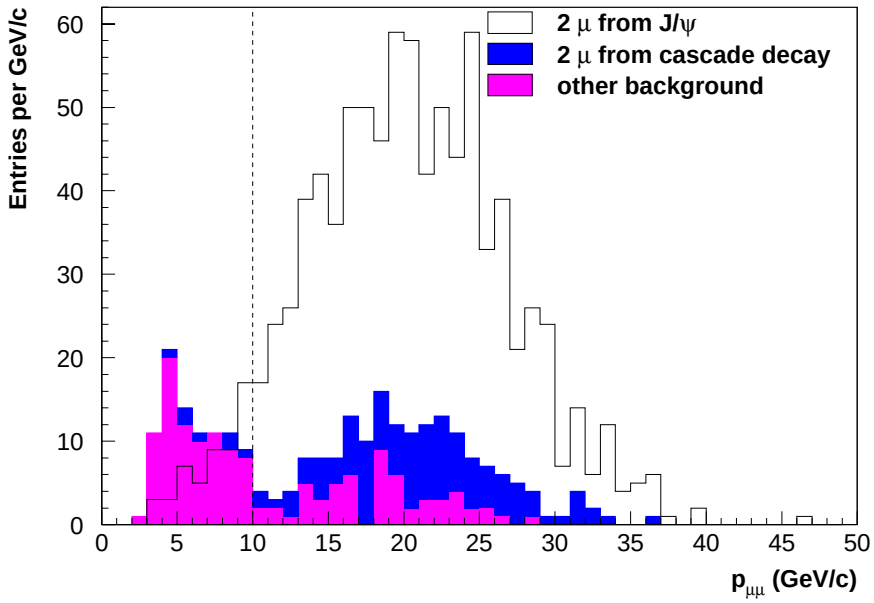

Figure 4.4: Variation in the sample composition with reconstructed momentum in simulated candidates that pass the other cuts and are in the mass window $2.95 \leq M_{\mu^+\mu^-} < 3.25$ GeV/c^2. The line histogram shows $J/\psi \to \mu^+\mu^-$ (or occasionally $\psi(2S) \to \mu^+\mu^-$), while the shaded histograms show the background, with candidates with two muons from cascade decays (see section 4.6) on top. The dashed line shows the limit of the chosen $p_{\mu\mu} \geq 10$ GeV/c cut.

4.3 J/ψ Candidate Selection

Subsequent analysis is performed interactively on the n-tuples using PAW [145].

A set of fairly loose cuts was chosen for the final selection, since efficiency is all, and a reasonable purity can still be obtained. Only candidates passing the section 4.2.1 and 4.2.3 cuts are considered.[6] Tighter muon identification is now performed: both daughter tracks must be identified as muons by the loose, standard, or tight tags (candidates previously selected with the very loose tag or Hadron Calorimeter tag (PXHAID) are dropped here). Since the reconstruction errors will be used in subsequent fits, candidates for which the standard vertex fit did not converge are rejected.

Figure 4.4 shows the value of cutting on the reconstructed momentum at rejecting misidentified muon background, so a selection

- reconstructed momentum, $p_{\mu\mu} \geq 10$ GeV/c

[6] Simulated J/ψs that failed those cuts are nevertheless stored on the n-tuple, so must be rejected here (NUMB > 0).

is applied. Although of little value anyway, momentum cuts much above 10 GeV/c start to significantly constrain the kinematically allowed range of B decay parameters, reducing the average ratio of B to J/ψ momenta and consequently increasing the required Monte Carlo correction to the decay time (c.f. equation 4.12). Note that this momentum cut is likely to remove more direct J/ψs (not shown in figure 4.4) than J/ψs from B decays, since direct J/ψs are expected to be softer.

In order to use the same sample as will eventually be used in the lifetime fit we require that the measured decay time (described later, in section 4.5) be within the fit range

- measured decay time, $-4 \leq t < 10$ ps.

The distribution of reconstructed masses of candidates selected by these cuts is shown in figure 4.5.

Various samples dependent on the relative charge of the daughter particles and on the reconstructed mass are used for background studies. The signal sample requires opposite daughter charges and

- reconstructed mass window, $2.95 \leq M_{\mu\mu} < 3.25$ GeV/c^2.

One event from this signal sample is shown in figures 4.6 and 4.7.

4.4 Fit Techniques

Two principal types of fit are used in this analysis. The background contamination is measured using fits to reconstructed masses ($M_{\mu\mu}$) and the lifetime is measured using fits to proper times (calculated from l_{xy}). In both cases an unbinned maximum likelihood fit is performed using the reconstructed parameters and their errors (which are calculated for each event).

Appendix D gives some of the formalism of maximum likelihood fitting and shows the relationships between the (normalized) maximum likelihood, extended maximum likelihood, binned maximum likelihood, and binned χ^2 fits. The extended maximum

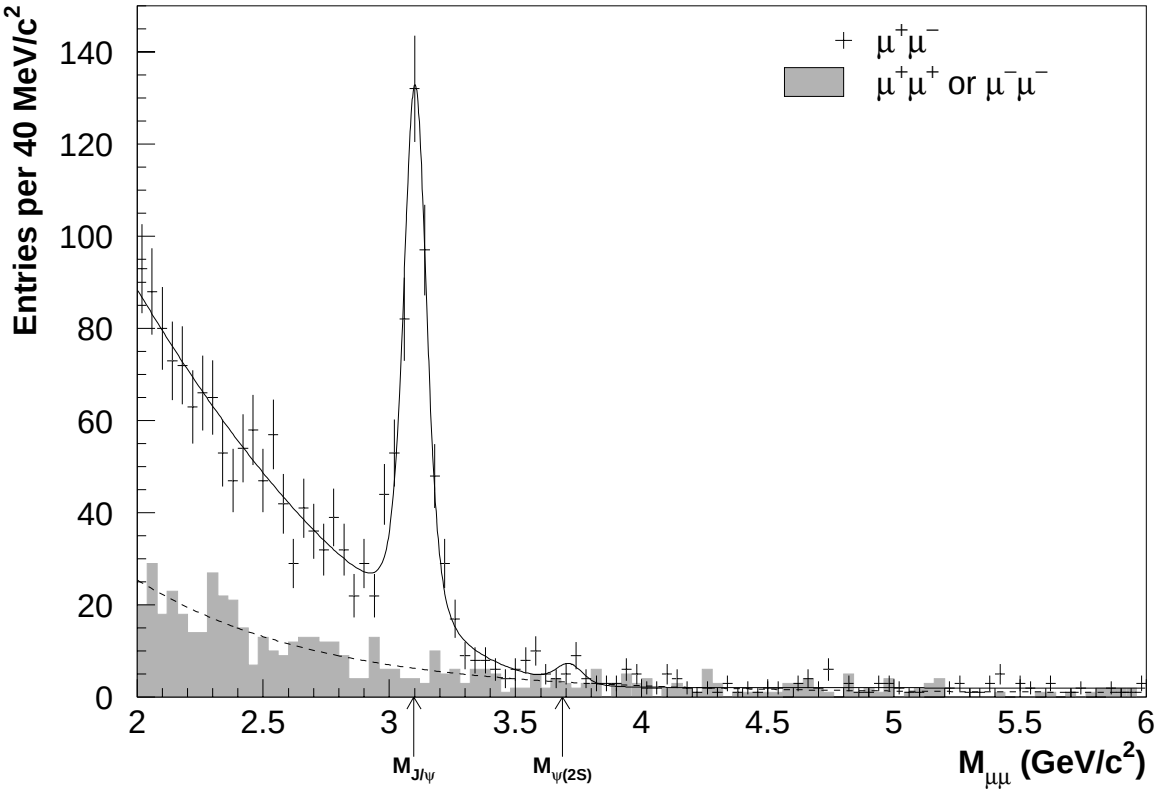

Opposite-sign fit (1941 candidates; 495 in $2.95 \leq M_{\mu\mu} < 3.25$ GeV/c^2 window)

J/ψ fraction in window	$f_{J/\psi} =$	(73.3±2.1)	%
hemiparabola fraction	$P_N =$	(69.9±1.6)	%
total ψ(2S)s	$N_{\psi(2S)} =$	16.7±6.6	
J/ψ mass	$M_{J/\psi} =$	(3102.3±3.4)	MeV/c^2
ψ(2S) mass	$M_{\psi(2S)} =$	(3713±24)	MeV/c^2
hemiparabola root	$x_0 =$	(3868±62)	MeV/c^2
error scale factor	$\alpha_\sigma =$	1.34±0.09	
function vs. histogram	$\chi^2 =$	52.5	(55 d.f.)
χ^2 in window	$\chi^2_w =$	8.9	(5 d.f.)

Like-sign fit (532 candidates; 41 in $2.95 \leq M_{\mu\mu} < 3.25$ GeV/c^2 window)

total in window	$N_w =$	47.0±2.4	
exponential parameter	$\kappa =$	(1.40±0.13)	(GeV/c^2)$^{-1}$
function vs. histogram	$\chi^2 =$	58.6	(51 d.f.)
χ^2 in window	$\chi^2_w =$	6.9	(5 d.f.)

Figure 4.5: Fit to the reconstructed masses of J/ψ candidates passing the section 4.3 cuts (1992–5). Candidates with opposite-sign (error bars) and like-sign (shaded histogram) track charges are shown. The solid curve shows a (2 × Gaussian + hemiparabola+constant) fit to the opposite-sign candidates. The dashed curve shows an (exponential + constant) fit to the like-sign candidates. The fit parameters are described in more detail in section 4.4.3; their values and errors are listed here above.

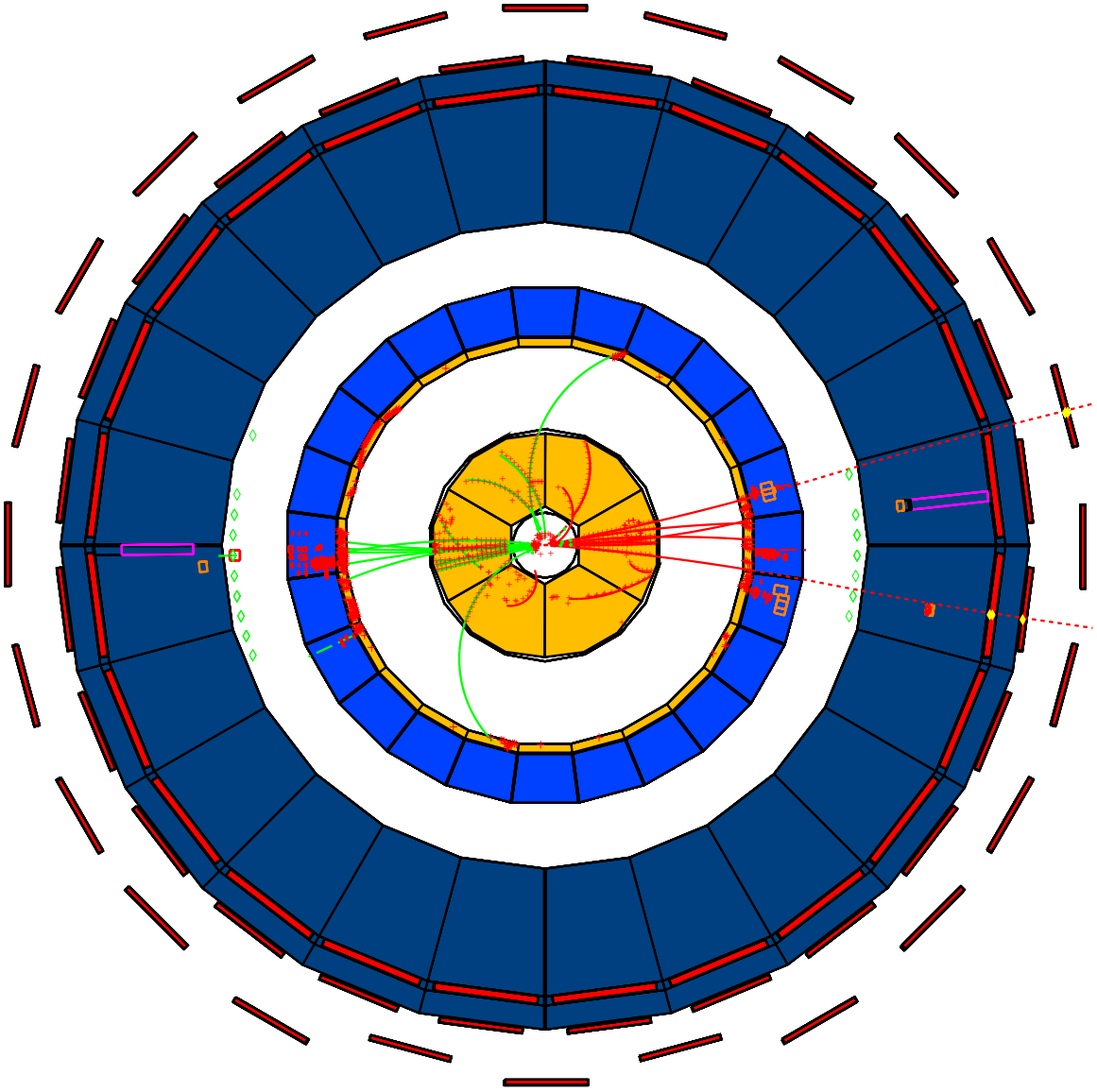

Figure 4.6: Display of a candidate J/ψ event.
The outer barrel tracking detectors (TPC and OD) are shown in orange, the barrel calorimeters (HPC and HAC) in blue, and the barrel muon chambers (MUB) in red. The two jets are coloured red and green. The two tracks identified as muons (both pass the tight selection) are extrapolated to the muon chambers: one (μ^-) gives two hits in the peripheral modules, the other (μ^+) two in the inner and one in the outer modules.
This event (run 49286 event 1261) was recorded on 12th July 1994. See figure 4.7 for a closeup of the central region.

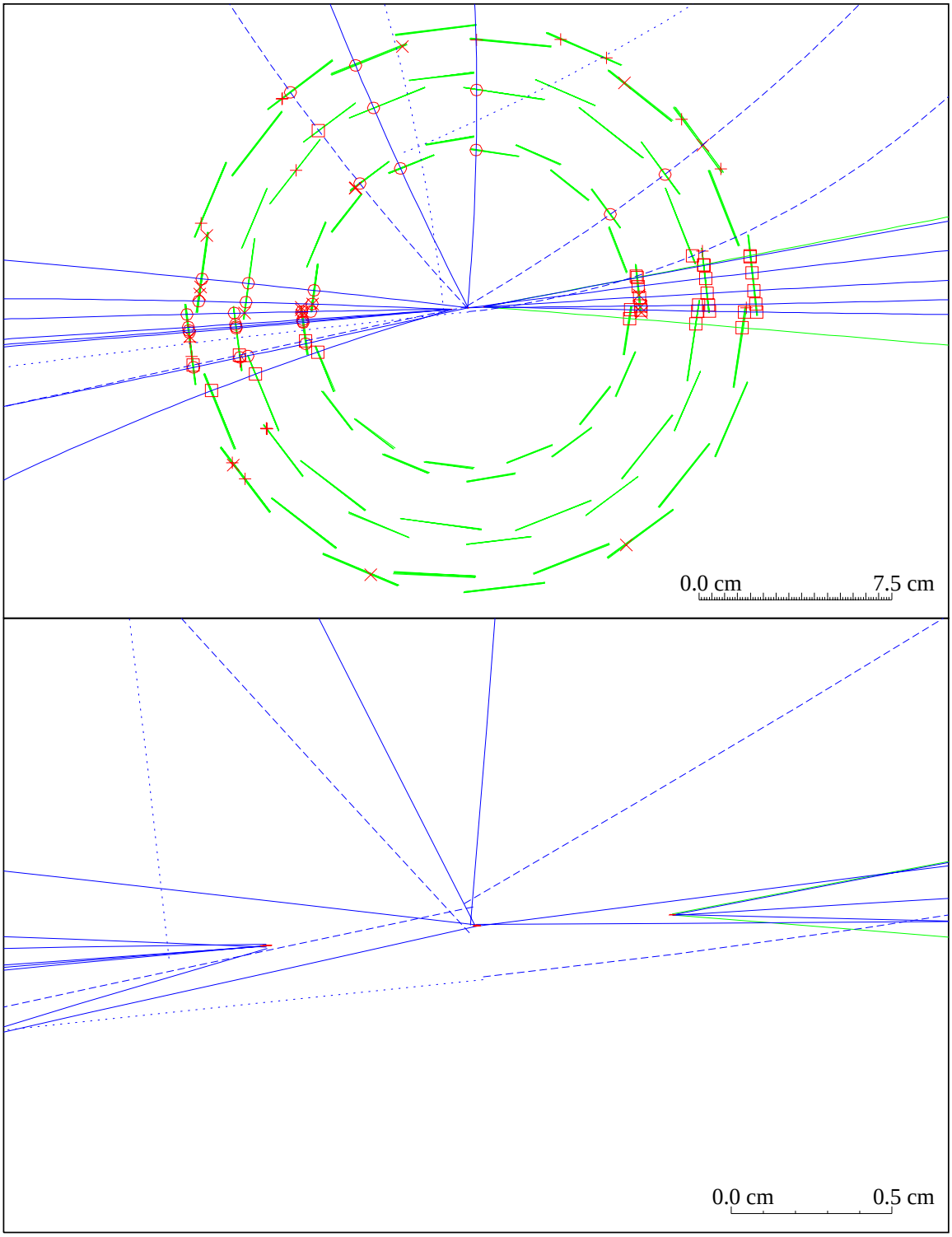

Figure 4.7: Vertex Detector views of a candidate J/ψ event. The upper diagram shows the VD plaquettes in green and VD hits as red circles ($+z$), squares ($-z$), or (for hits not associated with a track) crosses.
The lower diagram shows a blowup of the vertex region. Tracks that could not be (unambiguously) associated [63] with a vertex are shown dashed; those with no associated VD hits are dotted. Reconstructed vertices and the beamspot are shown in red by their (just visible!) error ellipses.
This event is one of the 495 signal events passing the section 4.3 cuts. The two muons (shown in green) give a reconstructed J/ψ mass of 3.067 ± 0.031 GeV/c^2, xy decay length of 0.605 ± 0.015 cm, and estimated decay time of 3.65 ± 0.78 ps.
The other (6-track) vertex is 0.653 ± 0.019 cm (xy) from the primary vertex.

likelihood fit was, in the end, not used in this analysis: it is unnecessary as the parameters of interest are only weakly dependent on the total sample size, and the function normalization is calculable. Significant variation in the reconstruction errors of different decay times requires that these be taken into account in the fit. An unbinned likelihood fit is the optimal method for doing this.

This is not of such overriding importance for the fit to the reconstructed masses, but here the rapid changes in the fit function round the J/ψ peak makes the choice of binning problematic (as shown in section D.3, the binned fit requires that the function not vary much over each bin), especially when the number of events per bin is small. This requires a difficult trade-off between having a reasonable number of entries per bin (required for a χ^2 fit) and a reasonably small bin size. This was a major problem in [146], which required rather dubious hand-adjustment of the binning to line up the bin positions with the peak position.

Fits on n-tuple data can in principle be performed within PAW. Unfortunately this is prohibitively slow using the tools currently available,[7] so instead the selected data points and their errors are written to a file and a separately compiled fitting program is run as a subprocess. The results of the fit (and function representation) are written to another file, read into PAW, and displayed. A single fitting program, based on the MINUIT [148] fitting package, is used for both the mass parameterization and the lifetime fit. The fit function is specified entirely with MINUIT parameters, allowing changes to be made from within MINUIT itself or specified when the subprocess is launched from PAW.

Since during the minimization process the fit function (which is interpreted as a likelihood, $\mathcal{L}$) cannot be constrained to remain positive for all of its range (although the overall normalization remains constant) giving an undefined log-likelihood, a cut-off is applied at $\mathcal{L} \leq 1 \times 10^{-10}$. Below that limit a polynomial is used instead of

[7] To perform the fit within PAW on VMS, the Fortran fit function would have to be calculated using the COMIS [147] interpreter. While a wonderful tool for simple routines, it is considerably slower than a compiled program, making it impracticable as an interactive tool for unbinned fits with many data points.

logarithm (with value and first two derivatives matched at the cut-off). Note that this is only applied during the minimization process — if the fit minimum (or the range of values on either side used to determine its error) has any data point's likelihood less than this cut-off, then the fit is considered to have failed.

4.4.1 Fit Result Representation

A general problem with unbinned fits is representation of the fit results. A related problem with likelihood fits is the determination of the quality of the fit (i.e. whether the final fit result well-describes the data — a poor fit quality could indicate that the original model or its allowed variation is not a good representation of the data). These problems are related because, if the fit result can be represented in a way that allows comparison with the data, then the quality of fit can be judged — either by eye or using a statistical test such as χ^2 or Kolmogorov.

The fit representation is not just of importance for determining the fit quality. On the mass plot, its area within the selection range is used to determine the background contamination.

This problem is easily solved for a fit to a 1-dimensional distribution (such as $M_{\mu\mu}$ or the lifetime) when we don't allow for any variation on reconstruction errors. The fit function, normalized to the number of events, can be compared directly with a histogram of the data. However, if each event has its own reconstruction error, the likelihood function is a convolution of the true distribution with a smearing function

$$f(x;\sigma) = f_{\text{true}}(x) \otimes G(x;\sigma) = \int f_{\text{true}}(u) \frac{1}{\sqrt{2\pi}\sigma} e^{-(x-u)^2/2\sigma^2} \mathrm{d}u \qquad (4.1)$$

where x is the measured variable, $f_{\text{true}}(u)$ is the distribution before measurement errors are introduced (e.g. the near-exponential distribution of B lifetimes) and $G(x;\sigma)$ is the smearing function: a Gaussian of width σ is used, and indeed the pull distribution $((x_{\text{reconstructed}} - x_{\text{true}})/\sigma)$ for both mass and lifetime in simulated data is

reasonably Gaussian centred on the origin and of unit RMS.[8]

There is usually no ideal method of representing this distribution that allows its comparison with the data on a 1-dimensional plot against x. Of course if the true distribution of errors, $S(x;\sigma)$, were known then we could plot

$$F(x) = \int f(x;\sigma)S(x;\sigma)\mathrm{d}\sigma \tag{4.2}$$

However this is rarely the case. Note that, in general (and often in practice), the reconstruction errors have some dependency on the measured variable, x.

One approximation that is often made is to assume that the true distribution of errors, $S(x;\sigma)$, may be approximated by the distribution of errors seen in the data.

$$S(x;\sigma) \approx \sum_i \delta(\sigma - \sigma_i) \tag{4.3}$$

where σ_i are the errors of each event in the sample. Substituting into 4.2 gives

$$F(x) \approx \sum_i f(x;\sigma_i) \tag{4.4}$$

However it doesn't often seem to be recognized that this is a reasonable approximation only if the dependence of $S(x;\sigma)$ upon x is weak. As shown in figure 4.8 this is not true for our two fits.

For the mass fit, a reasonable approximation is to assume that the errors are proportional to the reconstructed mass, so we replace $f(x;\sigma_i)$ with $f(x;\sigma_i x/x_i)$ in equation 4.4. In fact we need only do this for the Gaussian signal part — the shape of the background is only weakly dependent on the reconstruction errors. This is convenient, as $f(x;\sigma_i x/x_i)$ is difficult to determine for exponential f_{true} (at least no analytic form is known, and calculating it numerically for each event is a heavy burden on computer time). For the signal, where $f_{\mathrm{true}}(u) = \delta(u - M_{\mathrm{J}/\psi})$, it is simply

[8] A better description for the reconstructed mass pulls would be to include a second Gaussian of width 3.5 consisting of 2.6% of the data.

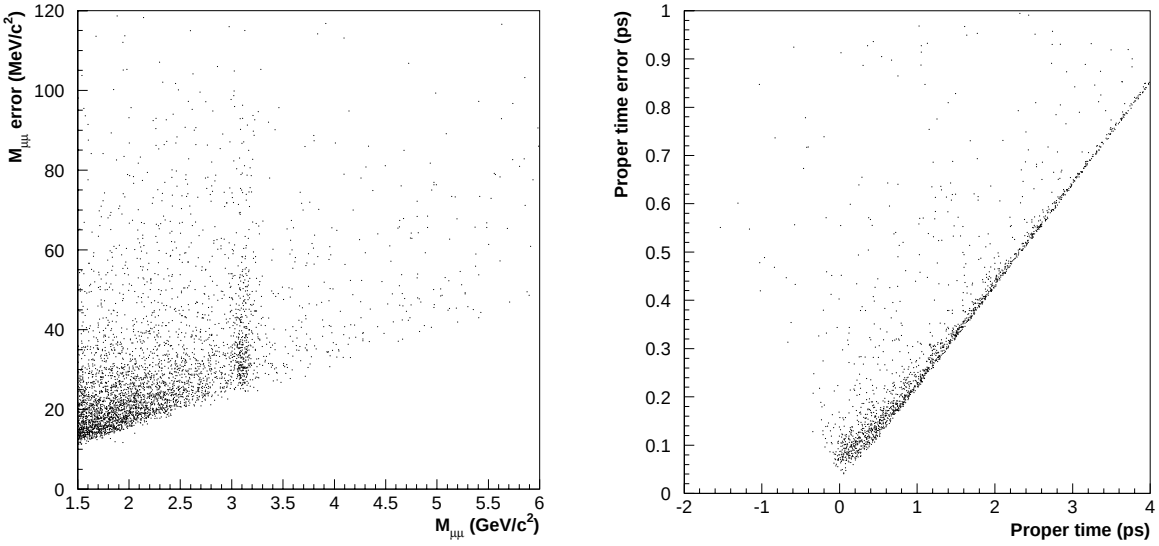

Figure 4.8: Mass and decay time reconstruction errors. The left-hand plot shows the variation in the reconstruction error on $M_{\mu\mu}$ with respect to $M_{\mu\mu}$ for 1992–5 data. The right-hand plot shows the variation in the reconstruction error of the decay times with respect to the measured decay times (cf. equation 4.13) for simulated true J/ψs.

$G(x; \sigma_i M_{J/\psi}/x_i)$. The change this produces can be seen in figure 4.9.

For the lifetime fit we cannot use this method. The errors are obviously not proportional to the decay time near the origin. We could of course attempt to parameterize the dependence on the decay time, but even a simple linear function (which would well-describe the distribution) would produce a non-analytic plot function. For this reason we choose a simpler method. The events are divided into four near-equal samples, ordered according to x_i. Equation 4.4 is used, but the sum is performed only over the events in the relevant sample, chosen such that x is within the range of x_is in the sample (the limits at each end being halfway between the largest x_i in one sample and the smallest in the next). Four samples were chosen as a compromise between allowing a reasonable number of events per sample and reducing the variation of errors within each sample. The normalization of the function within each sample range is adjusted to ensure continuity at the limits and the overall function is normalized to the total number of events. We cannot normalize to the number of events in each sample range, as that would bias the function shape to that of the data. The change this method produces can be seen in figure 4.10.

This perhaps arbitrary technique produces reasonable behaviour. Changing the

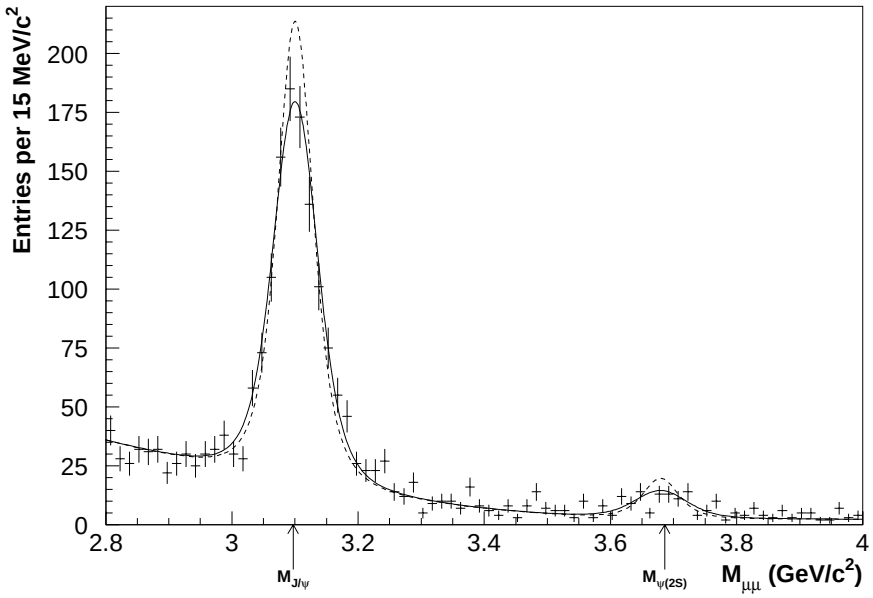

Figure 4.9: Comparison of mass fit representations for simulated data (blown up round the signal region). Both curves are representations of a single fit to the opposite sign candidate masses in the full mass range, $2 \leq M_{\mu^+\mu^-} < 6$ GeV/c^2. The dashed curve shows the simple plot function of equation 4.4, while the solid curve shows the plot function corrected for the variation in errors with mass. In the signal region $2.95 \leq M_{\mu^+\mu^-} < 3.25$ GeV/c^2, the corrected function clearly agrees ($\chi^2/\text{NDF} = 24.2/18$) with the histogram of the data (error bars) better than the uncorrected function ($\chi^2/\text{NDF} = 42.8/18$).

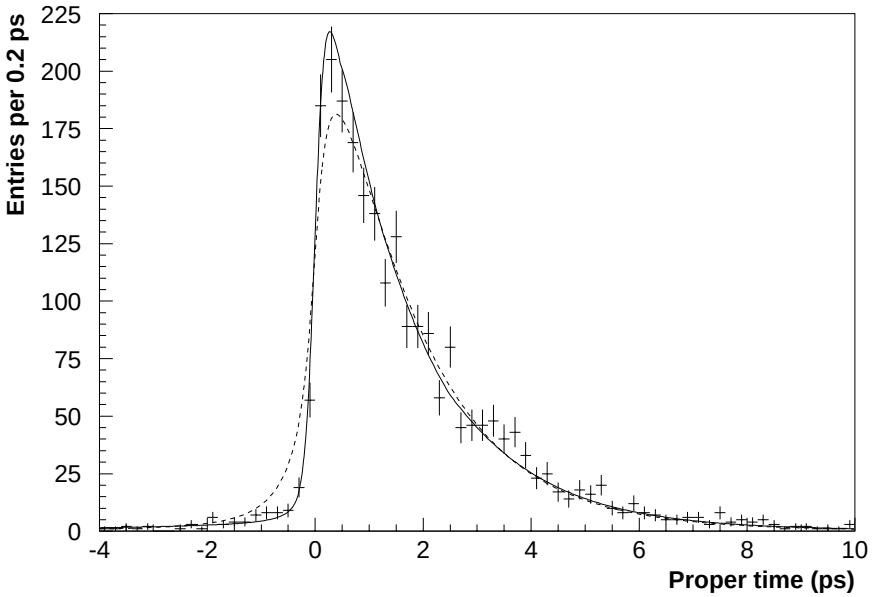

Figure 4.10: Comparison of lifetime fit representations for simulated true B $\rightarrow$ J/ψ events. The dashed curve shows the simple plot function of equation 4.4, while the solid curve shows the four-sample plot function. While not perfect, the latter clearly agrees ($\chi^2/\text{NDF} = 62.8/44$) with the histogram of the data (error bars) better than the former ($\chi^2/\text{NDF} = 114/49$).

fit parameters by 1σ (the errors on the fitted function) causes a change of ~ 1 in the χ^2 between the plot function and a histogram of the data.

For a quantitative comparison of plot function and data histogram, a χ^2 test was used.[9] The plot function was integrated across each bin to determine the expected bin contents, f_b. For the χ^2 test bin errors of $\sqrt{f_b}$ were assumed. Since the Poisson-distributed bin contents only approximate to the Gaussian distribution assumed by the χ^2 test for large f_b, bins with $f_b < 5$ were combined with their neighbours until the total was 5 or more.

4.4.2 Backgroundless Decay Time Fit

The dependence of the errors on the decay time affects the lifetime fit as well as its representation. In the fit to reconstructed decay times of simulated $B \to J/\psi$ (without background or prompt component) shown in figure 4.10, a small but significant bias is seen in the fitted lifetime compared to the mean true lifetime (and generated lifetime). This is solely an effect of performing the likelihood fit with reconstruction errors correlated with the decay times (see figure 4.8), as is demonstrated with a few simple simulations.

First, each event's *true* decay time is smeared with its reconstruction error and then fitted using the same reconstruction error in the fit function. The fitted lifetime shows a bias, but no bias if the reconstruction error used in both smearing and fit function is chosen from a different event. This latter case has the same distribution of errors, but they are uncorrelated with the decay times. Similarly, fits to randomly-generated decay times smeared with non-random or randomly-generated errors only show a bias if the errors are correlated with the decay times (either true or reconstructed).

The bias measured from Monte Carlo is used to correct the fitted lifetime. For-

[9] A Kolmogorov test was also used, but only as a crosscheck. Since the comparison is with the result of a fit rather then some theoretical function, Kolmogorov probabilities very close to 1 were obtained. However this might indicate a problem if a low probability were obtained.

tunately the size of the correction should be relatively model-insensitive, since it is primarily dependent on the distribution of decay time errors, the variation of which depend upon the constants α and σ_α (described in section 4.5), which are applied identically to both Monte Carlo and data. With a generated lifetime of 1.6 ps, the fitted lifetime is (1.52 ± 0.04) ps. Reweighting the generated lifetime to 1.4 ps and 1.8 ps gives $\tau_{\rm B} = (1.33 \pm 0.05)$ and (1.69 ± 0.06) ps respectively. Due to the reweighting process, these cannot be taken as independent estimates of the bias, but their variation over a reasonable range of lifetimes gives a systematic error. The fitted lifetime bias is thus

$$\Delta_\tau = (-0.08 \pm 0.04 \text{ (stat.)} \pm 0.03 \text{ (syst.)}) \text{ ps.} \tag{4.5}$$

4.4.3 Mass Distribution Parameterization

For the fit to the reconstructed masses in figure 4.5, basic fit functions

$$f_{\rm true}(x) = G_N \delta(x - \mu) + E_N \Theta(x) e^{-\kappa x} + C_N \tag{4.6}$$

or

$$f_{\rm true}(x) = G_N \delta(x - \mu) + P_N \Theta(x_0 - x)(x_0 - x)^2 + C_N \tag{4.7}$$

were used.[10] These were convoluted with a Gaussian of width given by each data point's measurement error (equation 4.1) multiplied by a scale factor α_σ. The fit parameters are G_N (fraction of signal events), μ (fitted J/ψ mass), E_N (exponential background fraction) or P_N (hemiparabolic background fraction), κ (exponential decay constant) or x_0 (hemiparabola zero point), and α_σ (error scaling). Overall normalization is ensured by fixing the flat background fraction $C_N = 1 - G_N - E_N$ (or P_N). An extra term $G_N^{\psi(2S)} \delta(x - \mu_{\psi(2S)})$ is added when there is sufficient signal to see the ψ(2S) (i.e. when 1992–5 data are combined). Each term must be normalized

[10] $\Theta(x)$ is the Heaviside step function, which takes a value of zero for $x < 0$ and unity for $x > 0$. Its differential is the Dirac delta function: $\delta(x) \equiv \frac{\rm d}{{\rm d}x}\Theta(x)$.

		Term, $T(x)$	Indefinite integral, $I(x)$
Gaussian	$G(x)$	$e^{-(x-\mu)^2/2\sigma^2}$	$\sqrt{2\pi}\,\sigma\mathcal{P}(\frac{x-\mu}{\sigma})$
Smeared exponential	$E(x)$	$e^{-\kappa x+\frac{1}{2}\kappa^2\sigma^2}\mathcal{P}(x/\sigma-\kappa\sigma)$	$(\mathcal{P}(x/\sigma)-T(x))/\kappa$
Smeared hemiparabola	$P(x)$	$\frac{\sigma(x_0-x)}{\sqrt{2\pi}}e^{-(x_0-x)^2/2\sigma^2}+$ $((x_0-x)^2+\sigma^2)\mathcal{P}(\frac{x_0-x}{\sigma})$	$-\frac{\sigma((x_0-x)^2+2\sigma^2)}{3\sqrt{2\pi}}e^{-(x_0-x)^2/2\sigma^2}-$ $(\frac{1}{3}(x_0-x)^2+\sigma^2)(x_0-x)\mathcal{P}(\frac{x_0-x}{\sigma})$
Flat background	$C(x)$	1	x

Table 4.2: Fit function terms after convolution. The normalized term is given by $G(x)$, $E(x)$, $P(x)$, or $C(x) = T(x)/(I(x_{\rm high}) - I(x_{\rm low}))$, where $I(x)$ is the indefinite integral of term $T(x)$ and $x_{\rm low} : x_{\rm high}$ is the plot range (the flat background is referred to as $C(x)$ despite the fact that it is independent of x, as a reminder that it must also be normalized to the plot range). x and σ are the data points and their measurement errors (after scaling by the fit parameter α_σ) respectively. μ, κ (or $1/\tau$), and x_0 are fit parameters. $\mathcal{P}(x)$ is the Normal Frequency function: $\mathcal{P}(x) \equiv \frac{1}{\sqrt{2\pi}}\int_{-\infty}^{x} e^{-\frac{1}{2}u^2}{\rm d}u = \frac{1}{2} + \frac{1}{2}\,{\rm erf}(x/\sqrt{2})$. Note that the functions listed here are those normally used — in certain limits (e.g. small σ) a simpler approximation (e.g. the unsmeared function) is used in order not to breach the machine's floating point limits in intermediate calculations.

to its fraction (G_N, E_N, etc.) within the plot range $2 \le x < 6$ after smearing (not before — convolution only preserves normalization to $-\infty < x < \infty$). The relevant terms are listed in table 4.2. Using the terms defined there, the fit function is

$$f(x) = G_N G(x;\mu,\sigma) + G_N^{\psi(2S)} G(x;\mu_{\psi(2S)},\sigma) + E_N E(x;\kappa,\sigma) + C_N C(x) \qquad (4.8)$$

or with $P_N P(x;x_0,\sigma)$ instead of the $E(x)$ term.

The fitted J/ψ mass, μ, and error scaling, α_σ, are left as free parameters to allow for systematic reconstruction errors. Their divergence from their nominal values ($M_{{\rm J}/\psi}$ and 1 respectively) relative to their fit errors gives an indication of the scale of these systematic errors.

The other parameters stated above are not directly useful. From this fit we are actually interested in determining the purity of the candidates to be used in our lifetime sample, i.e. those in the mass window $w_{\rm low} \le M_{\mu^+\mu^-} < w_{\rm high}$ (usually $2.95 \le M_{\mu^+\mu^-} < 3.25$ GeV/c^2). This can be calculated from the integral, between $w_{\rm low}$ and $w_{\rm high}$, of the fit representation function described in section 4.4.1 and shown in

figure 4.9, namely

$$f_{\mathrm{J}/\psi} = \frac{\int_{w_{\mathrm{low}}}^{w_{\mathrm{high}}} \sum_i G_N G(x; \sigma_i \mu / x_i) \mathrm{d}x}{\int_{w_{\mathrm{low}}}^{w_{\mathrm{high}}} \sum_i f(x; \sigma_i) \mathrm{d}x} \tag{4.9}$$

where $f(x;\sigma_i)$ is the (normalized) function described above (with terms listed in table 4.2) except that the Gaussian term has σ_i scaled to μ as is done in the numerator.

In order to allow for non-linearities in the calculation of errors on $f_{\mathrm{J}/\psi}$, this procedure is applied in reverse by solution of equation 4.9 for G_N. $f_{\mathrm{J}/\psi}$ is supplied as a fit parameter and G_N is calculated from it for each iteration of the fit. Allowing $f_{\mathrm{J}/\psi}$ to vary in the fit allows its value and statistical error to be determined.

A similar, but simpler, fit is performed on the like-sign candidates. In this case, no J/ψ signal is expected, so we fix $G_N = 0$, fitting for the remaining parameters (excluding μ of course). α_σ also has to be fixed to its nominal value of 1 since, without the J/ψ peak, α_σ is hardly constrained by the mass distribution. From this fit we are interested in extracting the number of like-sign candidates within the mass window as an estimate of the number of opposite-sign misidentified muon candidates in the lifetime sample. Of course we could obtain this most simply by just counting the like sign candidates within the window. However, due to the relatively small number of events involved, a better estimate is made by fitting for this number using the entire distribution. Again we can use the integral of the plot function within the mass window

$$N_w = \int_{w_{\mathrm{low}}}^{w_{\mathrm{high}}} \sum_i f_{\mathrm{like}}(x; \sigma_i) \mathrm{d}x \tag{4.10}$$

where $f_{\mathrm{like}}(x;\sigma_i)$ is the like-sign fit function. Again this procedure is applied in reverse, introducing N_w as a fit parameter replacing E_N or P_N (depending on the fit function in use), which is calculated from N_w for each fit iteration.

4.5 B-Hadron Decay Times

The vertex fit described in section 4.2.4 gives a 3-dimensional vertex position relative to the primary vertex (with errors that include the uncertainty in the primary vertex

position as estimated from the beamspot). The decay length is the magnitude of this relative vertex position, but using the z-component would introduce a prohibitively large uncertainty due to the shape of the beamspot, which is 1 cm long in z, ~ 50 times longer than its width in x. Instead, the decay length in the transverse plane, l_{xy}, is used.[11]

If the decay length were perfectly known, then reducing the (x, y) coordinates to l_{xy} would recover the 1-dimensional transverse decay length. But smearing (x, y) with a 2-dimensional uncertainty (e.g. bivariate Gaussian) gives a reduction (to zero at the origin) in the number of events for $l_{xy} \lesssim \sigma$. Given the complexity of the functional form of the resulting distribution,[12] the component of the decay vector (the measured vector from primary to secondary vertex, with azimuthal angle ϕ_V) along the B momentum vector ($\phi_{\rm B}$), $d_{xy} = l_{xy}\cos(\phi_{\rm B} - \phi_V)$, is used instead. This variable doesn't suffer from a phase space reduction. If $\phi_{\rm B}$ were known, this would be marginally better than using the magnitude of the decay vector as the other component provides no lifetime information.

For $\mathrm{B} \to \mathrm{J}/\psi$, the B (proper) decay times are given by $t = l/c\beta\gamma$, where l is the (3D) decay length, and $c\beta$ is the velocity and γ the Lorentz boost ($\gamma \equiv (1-\beta^2)^{-\frac{1}{2}}$) of the B in the lab frame. $c\beta\gamma = p_{\rm B}/m_{\rm B}$ and $l = l_{xy}\cos(\phi_{\rm B} - \phi_V)/\sin\theta_{\rm B}$, so

$$t = \frac{m_{\rm B} l_{xy}\cos(\phi_{\rm B} - \phi_V)}{p_{\rm B}\sin\theta_{\rm B}} \tag{4.11}$$

In the case of the $\mathrm{B} \to \mathrm{J}/\psi$, we are fortunate to reconstruct a large (and well-known) fraction of the parent's mass. This makes estimation of the B momentum by the method of [149] particularly appropriate: the B and J/ψ velocities are similar, so the former can be estimated from the measurement of the latter: $(\beta\gamma)_{\rm B} \approx (\beta\gamma)_{\mathrm{J}/\psi}$, $\sin\theta_{\rm B} \approx \sin\theta_{\mathrm{J}/\psi}$, and $\phi_{\rm B} \approx \phi_{\mathrm{J}/\psi}$. Absorbing both the statistical and systematic

[11] Another possibility would be to perform a primary vertex fit for each event. However this gives little improvement in the overall lifetime fit (where the number of signal events is of greatest importance) and risks (slightly) reducing the sample size (due to events where no primary vertex fit can be performed) and introducing systematic effects (due to erroneously including secondary tracks in the primary vertex fit).

[12] requiring triple integration using numeric methods to obtain the normalized function

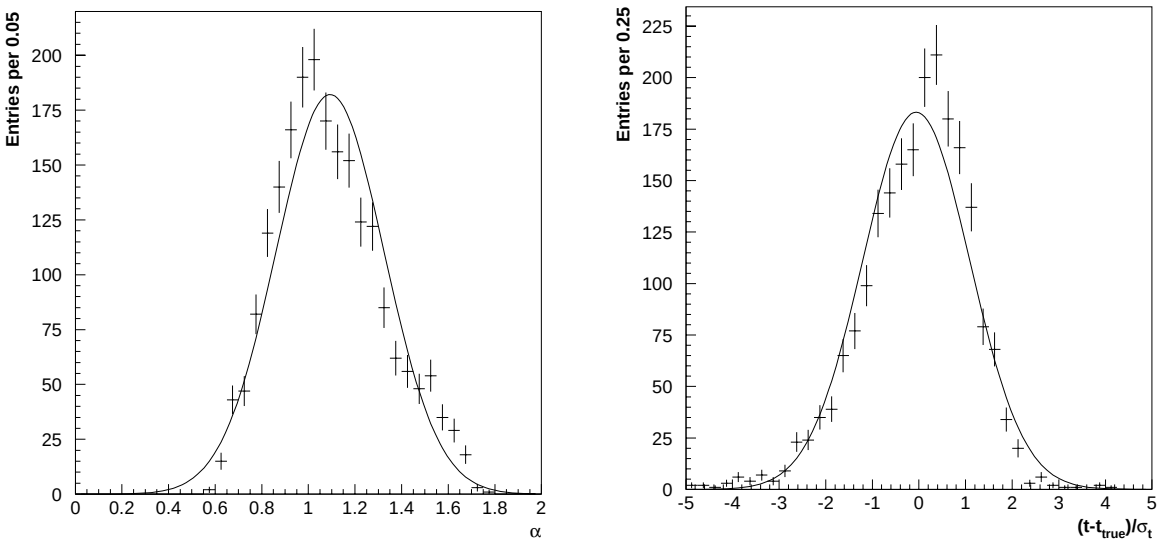

Figure 4.11: Monte Carlo correction for B decay time uncertainty. The first histogram shows α (equation 4.12) plotted for true B $\rightarrow$ J/ψ candidates that pass all cuts (including $2.95 \leq M_{\mu^+\mu^-} < 3.25$ GeV/c^2). It has a central value of $\alpha = 1.094 \pm 0.005$ and width $\sigma_\alpha = 0.232 \pm 0.004$. The second histogram second shows the B decay time pull $((t - t_{\rm true})/\sigma_t)$ distribution when these values are used in equation 4.13. It has a central value of -0.058 ± 0.025 and width 1.150 ± 0.018. The curves show the Gaussian fits to the distributions which were used to determine the central values and widths.

uncertainty of these approximations into a single factor,

$$\alpha \equiv \frac{(\beta\gamma)_{\rm J/\psi}}{(\beta\gamma)_{\rm B}} \frac{\sin\theta_{\rm J/\psi}}{\sin\theta_{\rm B}} \frac{\cos(\phi_{\rm B} - \phi_V)}{\cos(\phi_{\rm J/\psi} - \phi_V)}, \tag{4.12}$$

the B decay times and their fractional errors become

$$t = \alpha \frac{M_{\rm J/\psi} l_{xy} \cos\zeta}{p_{\rm J/\psi} \sin\theta_{\rm J/\psi}} \qquad \frac{\sigma_t}{|t|} = \frac{\sigma_\alpha}{\alpha} \oplus \frac{\sigma_{l_{xy}}}{l_{xy}} \oplus \sigma_\zeta \tan\zeta \oplus \frac{\sigma_{p_{\rm J/\psi}}}{p_{\rm J/\psi}} \tag{4.13}$$

For the signal, $M_{\rm J/\psi}$ is well known. For background 'lifetime' fits outside the mass window, the reconstructed mass, $M_{\mu\mu}$, is used instead to produce 'decay' time distributions that are comparable between different mass ranges. l_{xy}, $p_{\rm J/\psi}$ (i.e. $p_{\mu\mu}$), $\theta_{\rm J/\psi}$, and $\zeta \equiv \phi_{\rm J/\psi} - \phi_V$ (the pointing angle of section 4.2.5) are measured for each event (the error on $\theta_{\rm J/\psi}$ is negligible and not included in the error determination). The mean value of α and its spread (σ_α) are measured from Monte Carlo (see figure 4.11) and used as a constant correction factor and error respectively. These two numbers

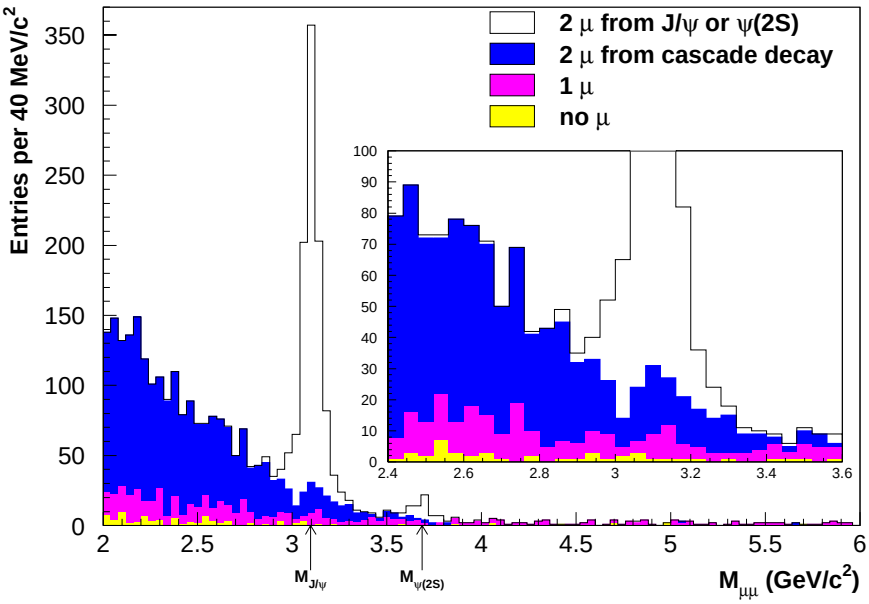

Figure 4.12: Opposite-sign sample composition in simulated data. The components, from top to bottom, are (a) $J/\psi \to \mu^+\mu^-$ or $\psi(2S) \to \mu^+\mu^-$; (b) two muons from cascade decay: $b \to c\mu^-\bar{\nu}_\mu$, $c \to s/d\mu^+\nu_\mu$ (or charge conjugate); (c) one (or occasionally two) muons, not from any of the above sources: mostly semileptonic B decays with a hadron misidentified as a muon; and (d) neither particle is a muon.

are the only significant Monte Carlo contribution to this analysis.

Note that the $\cos\zeta$ term gives $t < 0$ when the decay vector is in the opposite direction to the J/ψ momentum vector. This can occur when measurement errors move the decay vertex to behind the primary vertex. These events are a useful cross-check that the errors (at small decay times at least) are well-understood.

4.6 Sample Composition

Figure 4.12 shows the composition of the opposite-sign sample. The sources of background can be divided into two main groups: other particles misidentified as muons, and cascade decays: involving $b \to c\mu^-\bar{\nu}_\mu$, $c \to s/d\mu^+\nu_\mu$ (and charge conjugate).

As figure 4.12 makes clear, the relative proportions of these two samples is significantly different under the peak compared to either side: there are few cascade decays with $M_{\mu\mu} \gg M_{J/\psi}$, while it is the dominant component for $M_{\mu\mu} \ll M_{J/\psi}$. The off-peak data is required to correct for the background contamination to the signal, but

since the two background components could have different 'decay' time distributions, it is important to correct for the change in their proportions when extrapolating from the off-peak to the peak samples.

This can be done using the like-sign candidates. The quark charges ensure that cascade decays produce muons of opposite charges, while there is no such constraint on misidentified muon background. Thus this is well-modelled by the like-sign candidates, while both are described by the opposite-sign candidates.

4.7 Lifetime Fit

Candidates for the lifetime fit are selected with the section 4.3 cuts and divided into samples according the relative charge of the two muons and the reconstructed mass: $2 \leq M_{\mu\mu} < 2.8$ GeV/c^2 for the sideband and $2.95 \leq M_{\mu\mu} < 3.25$ GeV/c^2 for the signal window (see figures 4.13–4.15).

A single fit is performed on the three samples of events: like-sign candidates in the sideband (**like-sign sample**), opposite-sign candidates in the sideband (**sideband sample**), and opposite-sign candidates in the window (**window sample**, which includes the signal). Each component within these samples (misidentified muons, cascade decays, and J/ψ) is fitted with a smeared exponential + Gaussian + constant (using functional forms listed in table 4.2), except no constant term is included for the J/ψ component. The Gaussian term is centred at the origin ($\mu = 0$).

Candidates in the like-sign sample, assumed to consist entirely of the misidentified muon component, are fitted with the function

$$L(x) = G_m G(x) + E_m E(x;\tau_m) + C_m C(x) \tag{4.14}$$

The sideband sample is assumed to contain the same number of misidentified muon candidates as the like-sign sample (fraction λ_s, modelled by $L(x)$) with the rest being

cascade background. The sideband sample is fitted with

$$\begin{aligned} S(x) =&(\lambda_s G_m + (1-\lambda_s)G_c)G(x) + \lambda_s E_m E(x;\tau_m) + (1-\lambda_s)E_c E(x;\tau_c) + \\ &(\lambda_s C_m + (1-\lambda_s)C_c)C(x). \end{aligned} \tag{4.15}$$

Finally the window sample is assumed to consist of J/ψs (fraction $f_{\mathrm{J}/\psi}$, which was obtained from the fit to the opposite-sign masses, as shown in figure 4.5), the same number of misidentified muon candidates as like-sign candidates in the window (fraction λ_w, this number having been obtained from the fit to like-sign masses), and the remainder cascade decays (fraction $\lambda_c \equiv 1 - f_{\mathrm{J}/\psi} - \lambda_w$). The window sample is fitted with

$$\begin{aligned} W(x) =&(\lambda_w G_m + \lambda_c G_c + f_{\mathrm{J}/\psi} G_\psi)G(x) + \\ &\lambda_w E_m E(x;\tau_m) + \lambda_c E_c E(x;\tau_c) + f_{\mathrm{J}/\psi} E_\psi E(x;\tau_{\mathrm{B}}) + \\ &(\lambda_w C_m + \lambda_c C_c)C(x). \end{aligned} \tag{4.16}$$

In the above formulae, τ_m, τ_c, and τ_{B} are the lifetimes of the misidentified muon, cascade, and $B \to \mathrm{J}/\psi$ components, respectively. These and the G_m, E_m, G_c, E_c, and G_ψ fractions are fit parameters, while fractions

$$C_m = 1 - G_m - E_m \tag{4.17}$$

$$C_c = 1 - G_c - E_c \tag{4.18}$$

$$E_\psi = 1 - G_\psi \tag{4.19}$$

are defined by the requirement for overall normalization within each sample. Interpretations of the fractions are given in table 4.3.

Parameter	Sample	Component	Term	
G_m	like-sign	misidentified muon	prompt	$G(x)$
E_m	like-sign	misidentified muon	decay	$E(x;\tau_m)$
G_c	sideband	cascade decay	prompt	$G(x)$
E_c	sideband	cascade decay	decay	$E(x;\tau_c)$
G_ψ	window	J/ψ	prompt	$G(x)$
C_m	like-sign	misidentified muon	flat	$C(x)$
C_c	sideband	cascade decay	flat	$C(x)$
E_ψ	window	$B \to$ J/ψ	decay	$E(x;\tau_{\rm B})$

Table 4.3: Definition of lifetime fit fractions. Each parameter gives the fraction of candidates in the specified sample and from the specified source component, that are described by the given term. The first set are fit parameters; the second set are derived from the fit parameters using equations 4.17–4.19.

A single log-likelihood is formed from all three samples

$$-\mathcal{L} = \sum_i \ln L(t_i, \sigma_i; G_m, E_m, \tau_m) + \sum_j \ln S(t_j, \sigma_j; G_c, E_c, \tau_c) + \sum_k \ln W(t_k, \sigma_k; G_\psi, \tau_{\rm B}), \tag{4.20}$$

where the sum over i is performed for candidates in the like-sign sample, j for the sideband sample, and k for the window sample. $\mathcal{L}$ is minimized with respect to the fit parameters.

In the mass parameterization of section 4.4.3 it was possible to fit for an overall error scale factor, α_σ. That is not possible in the lifetime fit because the shape of the distribution is most affected by the errors close to the origin, but this is the region least affected by a multiplicative scale (since these candidates have smaller absolute decay time errors). In contrast a correction, Δ_σ, added in quadrature to each error affects the small decay time candidates most, and can thus be determined from the data. To allow for smooth variation round $\Delta_\sigma = 0$, the corrected error is defined as $\sigma' = (\sigma^2 \pm \Delta_\sigma^2)^{\frac{1}{2}}$, with Δ_σ^2 being subtracted for $\Delta_\sigma < 0$ (to a minimum $\sigma' \geq \sigma/1000$).

To allow for a better parameterization of the background components without affecting the signal function, a separate error correction is applied to each component: Δ_m, Δ_c, and Δ_ψ for the misidentified muon, cascade, and signal components respectively. Δ_m is applied to fit functions $E(x, \tau_m)$ and the G_m part of $G(x)$ in

equations 4.14–4.16, and analogously for Δ_c and Δ_ψ.

The background events do not usually have a true vertex to reconstruct: typically it is some sort of average between the primary and semileptonic decay vertices (for misidentified muon background) or between the b and c decay vertices (for cascade background). A non-zero error correction on the backgrounds could reflect this; on the signal it would indicate that the errors were incorrectly determined.

4.7.1 Fit Results

From the section 4.4.3 mass fit (figure 4.5) and this lifetime fit, shown in figures 4.13–4.15, we obtain

- number of selected J/ψs, $N_{\mathrm{J}/\psi} = 363 \pm 19$,
- fraction of prompt J/ψ, $N_{\mathrm{prompt}}/N_{\mathrm{J}/\psi} \equiv G_\psi = (9.6 \pm 3.2)\%$, and
- B lifetime, $\tau_{\mathrm{B}} = (1.53 \pm 0.11)$ ps.

after applying the section 4.4.2 lifetime bias correction.

Apart from the error correction, Δ_ψ, in figure 4.15, all fit errors are symmetric (to within 2 in the last quoted figure) with parabolic fit function around the minimum. The correlation coefficient between G_ψ and τ_{B} is +0.23. The slightly larger error on G_ψ compared to the fit result in figure 4.15 is due to the uncertainties in λ_s, λ_w, and λ_c (mainly the latter). Varying the parameter values input to the fit by their errors (from the Poisson variation in the sample sizes or the figure 4.5 fit errors on $f_{\mathrm{J}/\psi}$ and N_w, which were used to calculate the λs) gave a variation in G_ψ of +1.4% and -1.0% and in τ_{B} of $\pm$0.02 ps. The effect of the statistical uncertainties in α and σ_α is negligible.

The composition of the signal window sample is

- $B \to$ J/ψ, $N_{\mathrm{decay}} = 328 \pm 21$,
- prompt J/ψ, $N_{\mathrm{prompt}} = 35 \pm 12$,

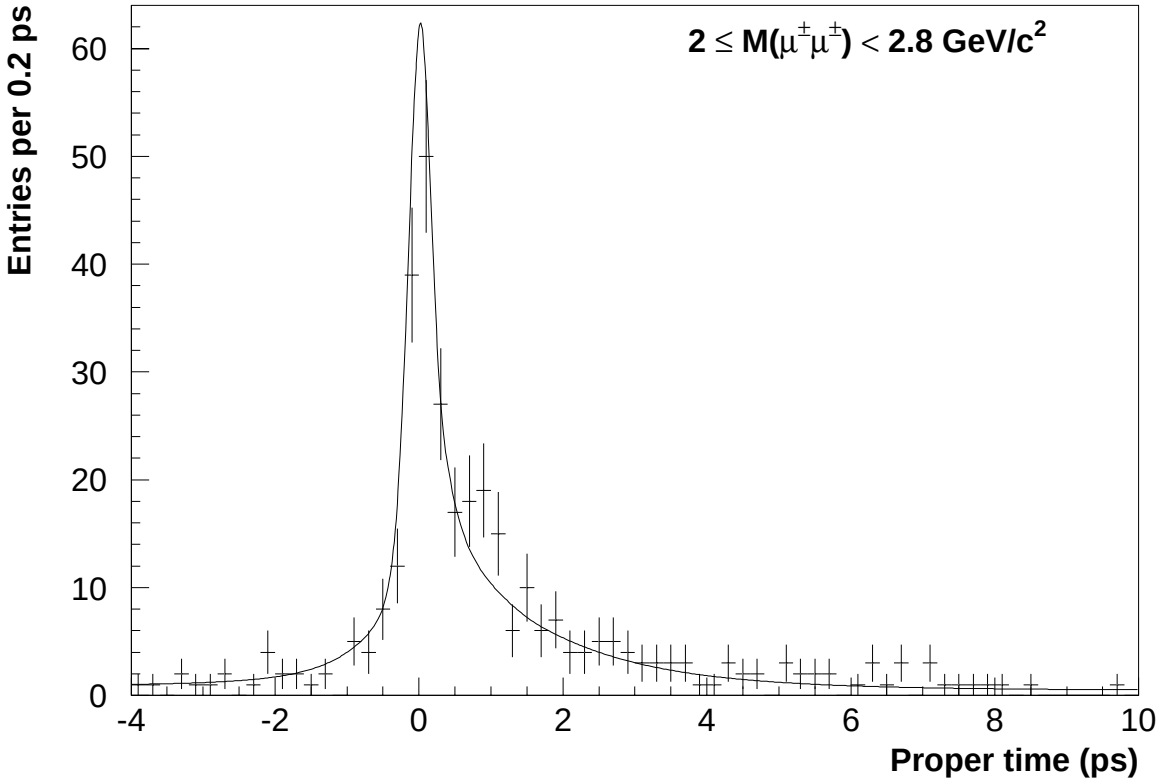

Misidentified muon background lifetime fit (333 like-sign candidates)

prompt fraction	$G_m =$	(34.6±3.6)	%
decay fraction	$E_m =$	(51.3±4.0)	%
lifetime	$\tau_m =$	(1.26±0.16)	ps
error correction	Δ_m	(0.12±0.02)	ps
function vs. histogram	$\chi^2 =$	30.1	(23 d.f.)

Figure 4.13: Lifetime distribution for like-sign candidates in the sideband $2 \leq M_{\mu\mu} < 2.8$ GeV/c^2. The curve, with fit parameters here above, shows the results of the equation-4.14 part of the fit, which can be compared with the histogram shown.

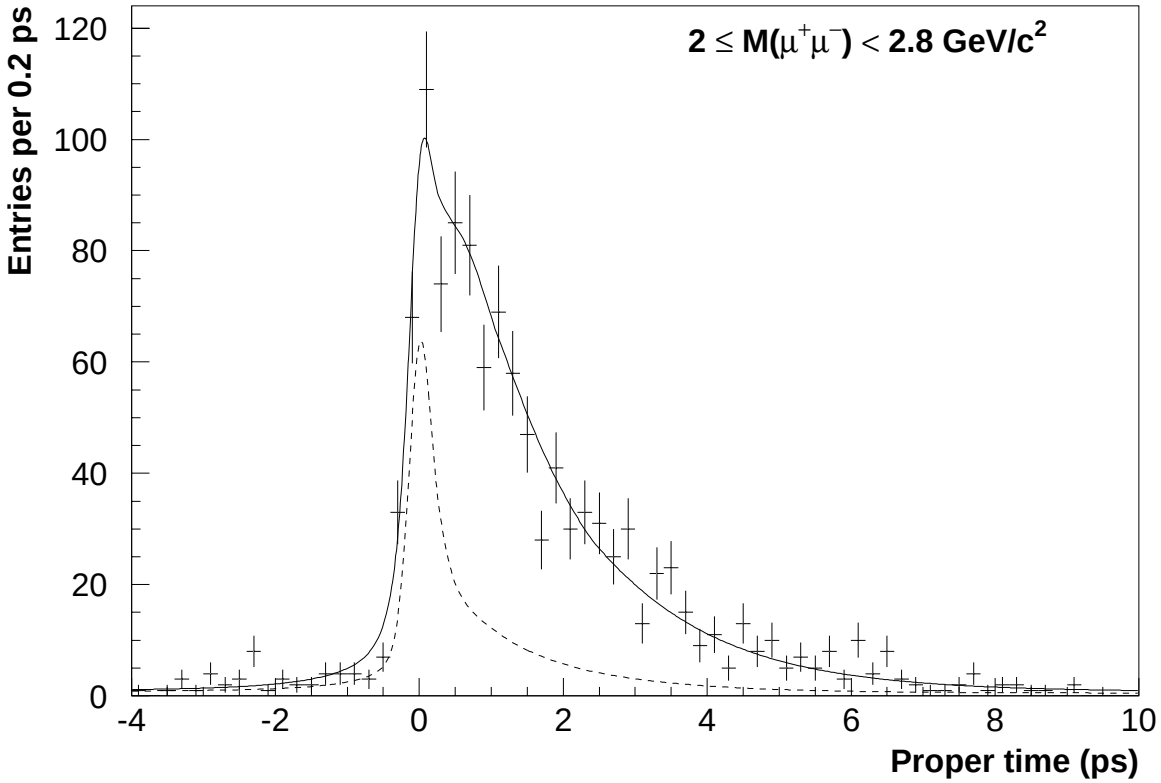

Cascade background lifetime fit (1155 sideband candidates; $\lambda_s = 0.288 \pm 0.018$)

prompt fraction	$G_c =$	(-6.3±4.2)	%
lifetime	$\tau_c =$	(1.44±0.09)	ps
error correction	Δ_c	(0.33±0.07)	ps
function vs. histogram	$\chi^2 =$	72.4	(39 d.f.)

Figure 4.14: Lifetime distribution for opposite-sign candidates in the sideband $2 \leq M_{\mu\mu} < 2.8$ GeV/c^2. The solid curve shows the results of the equation-4.15 part of the fit, which can be compared with the histogram shown. The dashed curve shows the misidentified muon component of this function, as specified in figure 4.13, scaled by λ_s. The difference is the cascade component, whose parameters are specified here above.

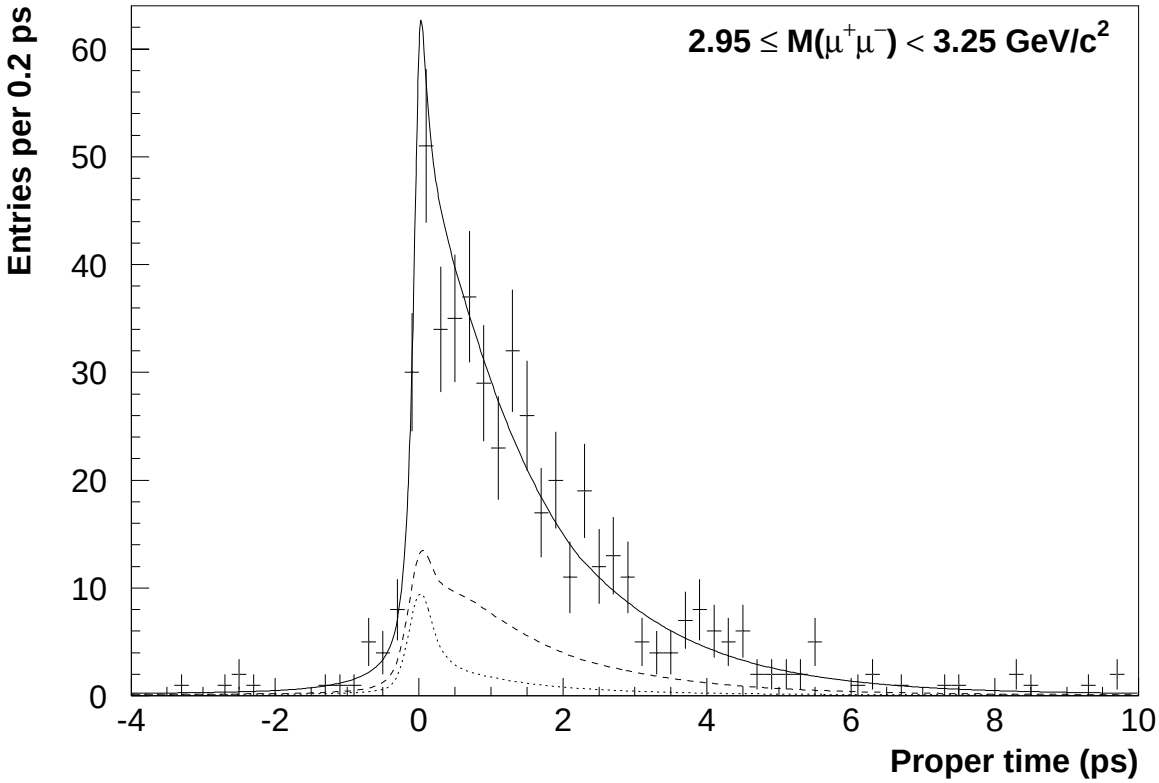

Signal lifetime fit (495 window candidates; $\lambda_w = 0.0949 \pm 0.0064$, $\lambda_c = 0.172 \pm 0.097$)

prompt fraction	$G_\psi =$	(9.6±2.8)	%
lifetime	$\tau_{\rm B}$	(1.45±0.11)	ps
error correction	Δ_ψ	$(-0.03^{+0.06}_{-0.01})$	ps
function vs. histogram	$\chi^2 =$	29.3	(25 d.f.)

Figure 4.15: Lifetime distribution for opposite-sign candidates in the signal window $2.95 \leq M_{\mu\mu} < 3.25$ GeV/c^2. The solid curve shows the results of the equation-4.16 part of the fit, which can be compared with the histogram shown. The dotted curve shows the misidentified muon component of this function, as specified in figure 4.13, scaled by λ_w. The dashed curve shows the cascade component of this function, as specified in figure 4.14, scaled by $1 - \lambda_w - f_{\rm J/\psi}$. The remainder (fraction $f_{\rm J/\psi}$) is the J/ψ component, whose parameters are specified here above.

- cascade decays, $N_c = 85 \pm 12$, and
- misidentified muons, $N_m = 47 \pm 2$,

though of course with highly correlated errors.

4.7.2 Fit to Monte Carlo Data

The method was repeated using an initial sample of 7,082,380 simulated hadronic events. The mass and lifetime fit results are shown in table 4.4 and, after correcting for the lifetime bias, we obtain

- $N_{\mathrm{J}/\psi} = 822 \pm 28$,
- $G_\psi = (2.2 \pm 1.7)\%$, and
- $\tau_{\mathrm{B}} = (1.56 \pm 0.07)$ ps.

This can be compared with 842 true J/ψs selected, of which 1.0% were formed at the primary vertex, the rest coming from B-hadrons with generated lifetime of 1.6 ps. The fitted background fractions all agree with the true numbers of misidentified muon and cascade events within each sample.

Additional cross-checks were performed using the same Monte Carlo sample but with $B \to \mathrm{J}/\psi$ lifetimes reweighted to 1.4 ps and 1.8 ps. 2,190,147 simulated $\mathrm{b\bar{b}}$ events provided another cross-check with no prompt component and different background fractions. In all cases the generated and measured lifetimes and prompt fractions were compatible.

4.8 Systematic Errors

The beauty of this method is that most of its inputs are measured from the data, so their uncertainties are statistical rather than systematic. In particular, the uncertainties due to the statistical errors on background shapes and fractions are already

Opposite-sign mass fit (3377 candidates; 1016 in $2.95 \leq M_{\mu\mu} < 3.25$ GeV/c^2 window)

J/ψ fraction in window	$f_{\mathrm{J}/\psi} =$	(80.9±1.1)	%
hemiparabola fraction	$P_N =$	(67.6±1.0)	%
total ψ(2S)s	$N_{\psi(2\mathrm{S})} =$	55.2±9.2	
J/ψ mass	$M_{\mathrm{J}/\psi} =$	(3101.1±1.5)	MeV/c^2
ψ(2S) mass	$M_{\psi(2\mathrm{S})} =$	(3679±9)	MeV/c^2
hemiparabola root	$x_0 =$	(3814±39)	MeV/c^2
error scale factor	$\alpha_\sigma =$	1.02±0.03	
function vs. histogram	$\chi^2 =$	51.8	(56 d.f.)
χ^2 in window	$\chi^2_w =$	6.1	(5 d.f.)

Like-sign mass fit (605 candidates; 63 in $2.95 \leq M_{\mu\mu} < 3.25$ GeV/c^2 window)

total in window	$N_w =$	53.6±2.3	
exponential parameter	$\kappa =$	(1.37±0.12)	$(\mathrm{GeV}/c^2)^{-1}$
function vs. histogram	$\chi^2 =$	55.6	(56 d.f.)
χ^2 in window	$\chi^2_w =$	1.2	(5 d.f.)

Misidentified muon background lifetime fit (361 like-sign candidates)

prompt fraction	$G_m =$	(23.3±4.8)	%
decay fraction	$E_m =$	(64.0±4.7)	%
lifetime	$\tau_m =$	(1.22±0.16)	ps
error correction	Δ_m	(0.28±0.05)	ps
function vs. histogram	$\chi^2 =$	27.2	(25 d.f.)

Cascade background lifetime fit (1963 sideband candidates; $\lambda_s = 0.184 \pm 0.011$)

prompt fraction	$G_c =$	(-0.2±1.8)	%
lifetime	$\tau_c =$	(1.55±0.06)	ps
error correction	Δ_c	(0.12±0.03)	ps
function vs. histogram	$\chi^2 =$	66.2	(46 d.f.)

Signal lifetime fit (1016 window candidates; $\lambda_w = 0.0527 \pm 0.0028$, $\lambda_c = 0.139 \pm 0.054$)

prompt fraction	$G_\psi =$	(2.2±1.7)	%
lifetime	τ_{B}	(1.48±0.07)	ps
error correction	Δ_ψ	$(0.04^{+0.04}_{-0.08})$	ps
function vs. histogram	$\chi^2 =$	32.5	(34 d.f.)

Table 4.4: Monte Carlo fit results, analogous to those shown in figures 4.5 and 4.13–4.15.

included above (the former are included by the fitting procedure and the latter were added explicitly).

The main sources of systematic error are from the parameterizations of the background mass and lifetime distributions, and from the two Monte Carlo inputs to the B momentum determination, α and σ_α. The error due to the estimation of the bias correction is calculated in section 4.4.2.

For the opposite-sign mass distribution (used to determine $f_{J/\psi}$), three changes in parameterization were considered separately. $M_{J/\psi}$ and $M_{\psi(2S)}$ were fixed to 3.097 and 3.686 GeV/c^2 [2] respectively rather than being allowed to vary in the fit; the error scaling, α_σ, was removed (fixed to 1); and the hemiparabolic background term (which gave the better fit to the data) was replaced with an exponential term. Only the change to α_σ had any significant effect: $f_{J/\psi}$ changes from 73.3 to 69.1%. When fed into the lifetime fit this causes an increase in G_ψ to 10.2%.

The estimate of the number of misidentified muon candidates in the window is improved by using a parameterization of the like-sign mass distribution. If the parameterization's exponential term is replaced by a hemiparabola, N_w increases from 47.0 to 50.6. This yields a decrease in G_ψ to 9.4%. If on the other hand we choose to use the actual number of like-sign candidates in the window and allow for a 1σ Poisson variation ($N_w = 41 \pm 6.4$), G_ψ varies from 9.6% to 10.6%.

Unlike G_ψ, τ_B is relatively insensitive to the background fractions due to the similarity of the fitted background and signal lifetimes.

An alternative parameterization for the cascade decay lifetime distribution was also tested. This might be expected to be better described by the convolution of two exponentials corresponding to the B decay following by the D decay (this is still not an ideal description because the two resulting muons don't come from a single vertex). This function is $E(x;\tau_1) - E(x;\tau_2)$, where the two lifetimes, τ_1 and τ_2, can be fitted for (actually fit parameters τ_1 and $\xi = \tau_2/\tau_1$ with $0 < \xi < 1$ are preferable). With this parameterization, a slightly altered $G_\psi = (9.4 \pm 2.9)\%$ was obtained (with $\tau_c = (1.39 \pm 0.11)$ ps, $\xi = 0.20 \pm 0.07$, and $\Delta_c = (-0.02^{+0.08}_{-0.02})$ ps), with only a small

improvement in the quality of the fit. For this reason, and because the particular values of τ_1 and τ_2 are not used, the simpler single exponential form was retained.

The pull distribution in figure 4.11 is far from perfect. A slightly better description is a double Gaussian with common mean -0.021 ± 0.025, central Gaussian width 1.041 ± 0.025, and $(2.4 \pm 1.1)\%$ in tails with width 2.76 ± 0.36 (similar tails are seen in the reconstructed masses). Using such a double Gaussian in the fit function decreases $\tau_{\rm B}$ to 1.41 ps.

There are two principal contributions to the correction factor, α. While the J/ψ mass is a large fraction of that of the B, it nevertheless acquires a boost in the B rest frame. This depends upon the particular decay mode. The second effect is due to anisotropic or momentum-dependent inefficiencies in the lab frame, which can spoil the averaging over all directions in the B rest frame.

The variation in the first effect can be estimated by comparing α for different B parent masses in the absence of detector inefficiencies (i.e. for all generated $\mathrm{B} \to$ J/ψ): $(\alpha, \sigma_\alpha) = (1.069, 0.235)$ ($\mathrm{B}^{0\pm}$), (1.076,0.249) ($\mathrm{B_s}$), and (1.089,0.268) ($\Lambda_{\rm B}$).

The second effect is dominated by the $p_{\mu\mu} \geq 10$ GeV/c cut. Data versus Monte Carlo agree in the mean and RMS momenta of selected candidates to roughly 0.4 GeV/c. Changes in the momentum cut of this order have little effect on α. However, applying the other J/ψ selection cuts changes (α, σ_α) from (1.086,0.231) to (1.094,0.232).

Taking these variations as conservative estimates, we obtain errors on α and σ_α of 0.02 and 0.03 respectively. Varying these two parameters together changes the fitted $\tau_{\rm B}$ by ± 0.02 ps.

Assuming all these errors are independent, and taking them as symmetric, we obtain the systematic errors listed in table 4.5 and quoted below.

Source	Systematic Error	
	τ_B (ps)	G_ψ (%)
Opposite-sign mass parameterization ($f_{J/\psi}$)	negligible	0.56
Like-sign mass parameterization (N_w)	negligible	0.28
Like-sign background fraction (N_w)	negligible	0.97
Cascade decay time parameterization	negligible	0.26
Decay error parameterization (σ_α)	0.034	0.14
Uncertainty on α and σ_α	0.015	negligible
True $B \to J/\psi$ fit bias statistical error	0.037	–
True $B \to J/\psi$ fit bias variation	0.030	–
Total	0.060	1.19

Table 4.5: Summary of systematic errors on the B lifetime (τ_B) and prompt fraction (G_ψ) from sections 4.4.2 and 4.8. These do not include the effect (0.02 ps on τ_B and 1.4% on G_ψ) of the statistical uncertainties in the background fractions (λ_s, λ_w, and λ_c) which are added to the statistical error in section 4.7.1.

4.9 Results and Interpretation

The above measurement of the mean lifetime of B-hadrons produced from the Z^0 and decaying to J/ψs gives

$$\tau_B = (1.53 \pm 0.11\ (\text{stat.}) \pm 0.06\ (\text{syst.}))\ \text{ps}. \tag{4.21}$$

This can be compared with previous LEP $B \to J/\psi$ measurements [146, 150, 151] of $\tau_B = (1.40 \pm 0.13)$ ps.[13]

As noted in chapter 1, if this mean is to be compared or combined with measurements in other channels, such as semileptonic or exclusive B decays, some account should be taken of the composition of the sample. According to the LUND PS Monte Carlo, J/ψs come from 83.8% $B^{0\pm}$, 7.3% B_s, 8.4% Λ_B, and 0.5% B_c (similarly for selected J/ψs). A comparison of different mean B-hadron lifetimes is given in table 4.6.

The measured prompt fraction of J/ψs is

$$\frac{N(Z^0 \to \text{prompt } J/\psi X)}{N(Z^0 \to J/\psi X)} = (9.6 \pm 3.2\ (\text{stat.}) \pm 1.2\ (\text{syst.}))\%. \tag{4.22}$$

[13]Note that 28% ($\sim$ 59 events) of the data that this average is based on is common with the 22% of our sample that was taken in 1992.

Sample	τ_B (ps)
Mean $B \to J/\psi$ at LEP	1.46 $\pm$0.10
Mean Inclusive B decay at LEP	1.576$\pm$0.016
Mean Semileptonic B decay at LEP	1.537$\pm$0.020
Mean $B \to J/\psi$ at the Tevatron ($p\bar{p}$)	1.533$\pm$0.036
B^0	1.56 $\pm$0.04
$B^\pm$	1.65 $\pm$0.04
B_s	1.54 $\pm$0.07
Λ_B	1.22 $\pm$0.05

Table 4.6: Summary of different B lifetime measurements. The LEP $B \to J/\psi$ lifetime is an average of [150, 151] and the measurement made here. The other lifetimes are world-averages given in [5].

This can be compared with previous measurements of $(7.7^{+6.3}_{-5.4})\%$ [146][14] and $(4.8 \pm 1.7\ (\text{stat.}) \pm 1.1\ (\text{syst.}) \pm 1.3\ (\text{theo.}))\%$ [6].

No attempt has been made here to calculate selection efficiencies, but an estimate of the Z^0 branching ratio to prompt J/ψ can be obtained using published values for the branching ratio to all J/ψ. Using (4.22) and $\text{Br}(Z^0 \to J/\psi X) = (0.380 \pm 0.027)\%$ [2, page 218][15] gives

$$\text{Br}(Z^0 \to \text{prompt } J/\psi X) = (0.036 \pm 0.013)\%. \tag{4.23}$$

Because of the $p_{\mu\mu} \geq 10$ GeV/c cut, this number does not take into account the expected larger $N_{\text{prompt}}/N_{J/\psi}$ ratio at lower momenta (especially from the dominant gluon fragmentation [11]).

This can be compared with the previous measurement of $(0.0300 \pm 0.0078\ (\text{stat.}) \pm 0.0030\ (\text{syst.}) \pm 0.0015\ (\text{theo.}))\%$ [153].

It should be noted that our measurement does not distinguish between J/ψs produced directly and those produced via the $\psi(2S)$ (about half of which decay to J/ψ) and other charmonium states. However [7] predicts a smaller rate for prompt $\psi(2S)$ production ($\sim \frac{1}{3}$ the J/ψ rate).

[14] 73% of its data is common with 22% of our sample.

[15] 10% of its data is common with 22% of our sample. The average does not include the recent L3 measurement [152] of $\text{Br}(Z^0 \to JX) = (0.340 \pm 0.023\ (\text{stat.}) \pm 0.027\ (\text{syst.}))\%$, though perhaps J and J/ψ measurements should not be combined!

These numbers are consistent with the theoretical predictions summarized in chapter 1. Summing the contributions from the two principal mechanisms (branching fractions 1.2 and 1.3) gives

$$\mathrm{Br}(\mathrm{Z}^0 \rightarrow \text{prompt } \mathrm{J}/\psi X) = 0.027\% \tag{4.24}$$

Appendix A

The DELPHI Collaboration

P.Abreu[21], W.Adam[49], T.Adye[36], P.Adzic[11], I.Ajinenko[41], G.D.Alekseev[16], R.Alemany[48], P.P.Allport[22], S.Almehed[24], U.Amaldi[9], S.Amato[46], P.Andersson[43], A.Andreazza[9], P.Antilogus[25], W-D.Apel[17], Y.Arnoud[14], B.Åsman[43], J-E.Augustin[25], A.Augustinus[9], P.Baillon[9], P.Bambade[19], F.Barao[21], G.Barbiellini[45], R.Barbier[25], D.Y.Bardin[16], G.Barker[9], A.Baroncelli[39], O.Barring[24], M.Battaglia[15], M.Baubillier[23], K-H.Becks[51], M.Begalli[6], P.Beilliere[8], Yu.Belokopytov[9,52], A.C.Benvenuti[5], C.Berat[14], M.Berggren[25], D.Bertini[25], D.Bertrand[2], M.Besancon[38], F.Bianchi[44], M.Bigi[44], M.S.Bilenky[16], M-A.Bizouard[19], D.Bloch[10], M.Bonesini[27], W.Bonivento[27], M.Boonekamp[38], P.S.L.Booth[22], A.W.Borgland[4], G.Borisov[38], C.Bosio[39], O.Botner[47], E.Boudinov[30], B.Bouquet[19], C.Bourdarios[19], T.J.V.Bowcock[22], I.Boyko[16], I.Bozovic[11], M.Bozzo[13], P.Branchini[39], K.D.Brand[35], T.Brenke[51], R.A.Brenner[47], R.Brown[9], P.Bruckman[35], J-M.Brunet[8], L.Bugge[32], T.Buran[32], T.Burgsmueller[51], P.Buschmann[51], S.Cabrera[48], M.Caccia[27], M.Calvi[27], A.J.Camacho Rozas[40], T.Camporesi[9], V.Canale[37], M.Canepa[13], F.Carena[9], L.Carroll[22], C.Caso[13], M.V.Castillo Gimenez[48], A.Cattai[9], F.R.Cavallo[5], Ch.Cerruti[10], V.Chabaud[9], Ph.Charpentier[9], L.Chaussard[25], P.Checchia[35], G.A.Chelkov[16], M.Chen[2], R.Chierici[44], P.Chliapnikov[41], P.Chochula[7], V.Chorowicz[25], J.Chudoba[29], P.Collins[9], M.Colomer[48], R.Contri[13], E.Cortina[48], G.Cosme[19], F.Cossutti[38], J-H.Cowell[22], H.B.Crawley[1], D.Crennell[36], G.Crosetti[13], J.Cuevas Maestro[33], S.Czellar[15], B.Dalmagne[19], G.Damgaard[28], M.Davenport[9], W.Da Silva[23], A.Deghorain[2], G.Della Ricca[45], P.Delpierre[26], N.Demaria[9], A.De Angelis[9], W.De Boer[17], S.De Brabandere[2], C.De Clercq[2], B.De Lotto[45], A.De Min[35], L.De Paula[46], H.Dijkstra[9], L.Di Ciaccio[37], A.Di Diodato[37], A.Djannati[8], J.Dolbeau[8], K.Doroba[50], M.Dracos[10], J.Drees[51], K.-A.Drees[51], M.Dris[31], A.Duperrin[25], J-D.Durand[25,9], R.Ehret[17], G.Eigen[4], T.Ekelof[47], G.Ekspong[43], M.Ellert[47], M.Elsing[9], J-P.Engel[10], B.Erzen[42], M.Espirito Santo[21], E.Falk[24], G.Fanourakis[11], D.Fassouliotis[11], J.Fayot[23], M.Feindt[17], A.Fenyuk[41], P.Ferrari[27], A.Ferrer[48], S.Fichet[23], A.Firestone[1], P.-A.Fischer[9], U.Flagmeyer[51], H.Foeth[9], E.Fokitis[31], F.Fontanelli[13], B.Franek[36], A.G.Frodesen[4], R.Fruhwirth[49], F.Fulda-Quenzer[19], J.Fuster[48], A.Galloni[22], D.Gamba[44], M.Gandelman[46], C.Garcia[48], J.Garcia[40], C.Gaspar[9], M.Gaspar[46], U.Gasparini[35], Ph.Gavillet[9], E.N.Gazis[31], D.Gele[10], J-P.Gerber[10], L.Gerdyukov[41], N.Ghodbane[25], I.Gil[48], F.Glege[51], R.Gokieli[50], B.Golob[42], P.Goncalves[21], I.Gonzalez Caballero[40], G.Gopal[36], L.Gorn[1,53], M.Gorski[50], Yu.Gouz[41], V.Gracco[13], J.Grahl[1], E.Graziani[39], C.Green[22], A.Grefrath[51], P.Gris[38], G.Grosdidier[19], K.Grzelak[50], M.Gunther[47], J.Guy[36], F.Hahn[9], S.Hahn[51], S.Haider[9], A.Hallgren[47], K.Hamacher[51], F.J.Harris[34], V.Hedberg[24], S.Heising[17], R.Henriques[21], J.J.Hernandez[48], P.Herquet[2], H.Herr[9], T.L.Hessing[34], J.-M.Heuser[51], E.Higon[48], S-O.Holmgren[43], P.J.Holt[34], D.Holthuizen[30], S.Hoorelbeke[2], M.Houlden[22], J.Hrubec[49], K.Huet[2], K.Hultqvist[43], J.N.Jackson[22], R.Jacobsson[43], P.Jalocha[9], R.Janik[7],

Ch.Jarlskog[24], G.Jarlskog[24], P.Jarry[38], B.Jean-Marie[19], E.K.Johansson[43], L.Jonsson[24], P.Jonsson[24], C.Joram[9], P.Juillot[10], F.Kapusta[23], K.Karafasoulis[11], S.Katsanevas[25], E.C.Katsoufis[31], R.Keranen[4], B.A.Khomenko[16], N.N.Khovanski[16], B.King[22], N.J.Kjaer[30], O.Klapp[51], H.Klein[9], P.Kluit[30], D.Knoblauch[17], P.Kokkinias[11], M.Koratzinos[9], V.Kostioukhine[41], C.Kourkoumelis[3], O.Kouznetsov[16], M.Krammer[49], C.Kreuter[9], I.Kronkvist[24], J.Krstic[11], Z.Krumstein[16], P.Kubinec[7], W.Kucewicz[18], K.Kurvinen[15], C.Lacasta[9], J.W.Lamsa[1], L.Lanceri[45], D.W.Lane[1], P.Langefeld[51], V.Lapin[41], J-P.Laugier[38], R.Lauhakangas[15], G.Leder[49], F.Ledroit[14], V.Lefebure[2], L.Leinonen[43], A.Leisos[11], R.Leitner[29], J.Lemonne[2], G.Lenzen[51], V.Lepeltier[19], T.Lesiak[18], M.Lethuillier[38], J.Libby[34], D.Liko[9], A.Lipniacka[43], I.Lippi[35], B.Loerstad[24], J.G.Loken[34], J.H.Lopes[46], J.M.Lopez[40], D.Loukas[11], P.Lutz[38], L.Lyons[34], J.MacNaughton[49], J.R.Mahon[6], A.Maio[21], A.Malek[51], T.G.M.Malmgren[43], V.Malychev[16], F.Mandl[49], J.Marco[40], R.Marco[40], B.Marechal[46], M.Margoni[35], J-C.Marin[9], C.Mariotti[9], A.Markou[11], C.Martinez-Rivero[33], F.Martinez-Vidal[48], S.Marti i Garcia[22], F.Matorras[40], C.Matteuzzi[27], G.Matthiae[37], F.Mazzucato[35], M.Mazzucato[35], M.Mc Cubbin[22], R.Mc Kay[1], R.Mc Nulty[9], G.Mc Pherson[22], J.Medbo[47], C.Meroni[27], A.Miagkov[41], M.Michelotto[35], E.Migliore[44], L.Mirabito[25], W.A.Mitaroff[49], U.Mjoernmark[24], T.Moa[43], R.Moeller[28], K.Moenig[9], M.R.Monge[13], X.Moreau[23], P.Morettini[13], G.Morton[34], K.Muenich[51], M.Mulders[30], L.M.Mundim[6], W.J.Murray[36], B.Muryn[14,18], G.Myatt[34], T.Myklebust[32], F.Naraghi[14], F.L.Navarria[5], S.Navas[48], K.Nawrocki[50], P.Negri[27], S.Nemecek[12], N.Neufeld[9], W.Neumann[51], N.Neumeister[49], R.Nicolaidou[14], B.S.Nielsen[28], M.Nieuwenhuizen[30], V.Nikolaenko[10], M.Nikolenko[10,16], A.Nomerotski[35], A.Normand[22], A.Nygren[24], W.Oberschulte-Beckmann[17], V.Obraztsov[41], A.G.Olshevski[16], A.Onofre[21], R.Orava[15], G.Orazi[10], K.Osterberg[15], A.Ouraou[38], P.Paganini[19], M.Paganoni[27], S.Paiano[5], R.Pain[23], R.Paiva[21], J.Palacios[34], H.Palka[18], Th.D.Papadopoulou[31], K.Papageorgiou[11], L.Pape[9], C.Parkes[34], F.Parodi[13], U.Parzefall[22], A.Passeri[39], M.Pegoraro[35], L.Peralta[21], H.Pernegger[49], M.Pernicka[49], A.Perrotta[5], C.Petridou[45], A.Petrolini[13], H.T.Phillips[36], G.Piana[13], F.Pierre[38], M.Pimenta[21], E.Piotto[35], T.Podobnik[42], O.Podobrin[9], M.E.Pol[6], G.Polok[18], P.Poropat[45], V.Pozdniakov[16], P.Privitera[37], N.Pukhaeva[16], A.Pullia[27], D.Radojicic[34], S.Ragazzi[27], H.Rahmani[31], D.Rakoczy[49], J.Rames[12], P.N.Ratoff[20], A.L.Read[32], P.Rebecchi[9], N.G.Redaelli[27], M.Regler[49], D.Reid[9], R.Reinhardt[51], P.B.Renton[34], L.K.Resvanis[3], F.Richard[19], J.Ridky[12], G.Rinaudo[44], O.Rohne[32], A.Romero[44], P.Ronchese[35], E.I.Rosenberg[1], P.Rosinsky[7], P.Roudeau[19], T.Rovelli[5], V.Ruhlmann-Kleider[38], A.Ruiz[40], H.Saarikko[15], Y.Sacquin[38], A.Sadovsky[16], G.Sajot[14], J.Salt[48], D.Sampsonidis[11], M.Sannino[13], H.Schneider[17], Ph.Schwemling[23], U.Schwickerath[17], M.A.E.Schyns[51], F.Scuri[45], P.Seager[20], Y.Sedykh[16], A.M.Segar[34], R.Sekulin[36], R.C.Shellard[6], A.Sheridan[22], R.Silvestre[38], F.Simonetto[35], A.N.Sisakian[16], T.B.Skaali[32], G.Smadja[25], N.Smirnov[41], O.Smirnova[24], G.R.Smith[36], A.Sopczak[17], R.Sosnowski[50], D.Souza-Santos[6], T.Spassov[21], E.Spiriti[39], P.Sponholz[51], S.Squarcia[13], D.Stampfer[49], C.Stanescu[39], S.Stanic[42], S.Stapnes[32], I.Stavitski[35], K.Stevenson[34], A.Stocchi[19], J.Strauss[49], R.Strub[10], B.Stugu[4], M.Szczekowski[50], M.Szeptycka[50], T.Tabarelli[27], F.Tegenfeldt[47], F.Terranova[27], J.Thomas[34], A.Tilquin[26], J.Timmermans[30], L.G.Tkatchev[16], T.Todorov[10], S.Todorova[10], D.Z.Toet[30], A.Tomaradze[2], B.Tome[21], A.Tonazzo[27], L.Tortora[39], G.Transtromer[24], D.Treille[9], G.Tristram[8], A.Trombini[19], C.Troncon[27], A.Tsirou[9], M-L.Turluer[38], I.A.Tyapkin[16], S.Tzamarias[11], B.Ueberschaer[51], O.Ullaland[9], V.Uvarov[41], G.Valenti[5], E.Vallazza[45], G.W.Van Apeldoorn[30], P.Van Dam[30], J.Van Eldik[30], A.Van Lysebetten[2], I.Van Vulpen[30], N.Vassilopoulos[34], G.Vegni[27], L.Ventura[35], W.Venus[36], F.Verbeure[2], M.Verlato[35], L.S.Vertogradov[16], V.Verzi[37], D.Vilanova[38], L.Vitale[45], E.Vlasov[41], A.S.Vodopyanov[16], V.Vrba[12], H.Wahlen[51], C.Walck[43], C.Weiser[17], A.M.Wetherell[9], D.Wicke[51], J.H.Wickens[2], G.R.Wilkinson[9], M.Winter[10], M.Witek[18], T.Wlodek[19],

G.Wolf[9], J.Yi[1], O.Yushchenko[41], A.Zalewska[18], P.Zalewski[50], D.Zavrtanik[42], E.Zevgolatakos[11], N.I.Zimin[16], G.C.Zucchelli[43], G.Zumerle[35]

[1] Department of Physics and Astronomy, Iowa State University, Ames IA 50011-3160, USA
[2] Physics Department, Univ. Instelling Antwerpen, Universiteitsplein 1, BE-2610 Wilrijk, Belgium and IIHE, ULB-VUB, Pleinlaan 2, BE-1050 Brussels, Belgium and Faculté des Sciences, Univ. de l'Etat Mons, Av. Maistriau 19, BE-7000 Mons, Belgium
[3] Physics Laboratory, University of Athens, Solonos Str. 104, GR-10680 Athens, Greece
[4] Department of Physics, University of Bergen, Allégaten 55, NO-5007 Bergen, Norway
[5] Dipartimento di Fisica, Università di Bologna and INFN, Via Irnerio 46, IT-40126 Bologna, Italy
[6] Centro Brasileiro de Pesquisas Físicas, rua Xavier Sigaud 150, BR-22290 Rio de Janeiro, Brazil and Depto. de Física, Pont. Univ. Católica, C.P. 38071 BR-22453 Rio de Janeiro, Brazil and Inst. de Física, Univ. Estadual do Rio de Janeiro, rua São Francisco Xavier 524, Rio de Janeiro, Brazil
[7] Comenius University, Faculty of Mathematics and Physics, Mlynska Dolina, SK-84215 Bratislava, Slovakia
[8] Collège de France, Lab. de Physique Corpusculaire, IN2P3-CNRS, FR-75231 Paris Cedex 05, France
[9] CERN, CH-1211 Geneva 23, Switzerland
[10] Institut de Recherches Subatomiques, IN2P3 - CNRS/ULP - BP20, FR-67037 Strasbourg Cedex, France
[11] Institute of Nuclear Physics, N.C.S.R. Demokritos, P.O. Box 60228, GR-15310 Athens, Greece
[12] FZU, Inst. of Phys. of the C.A.S. High Energy Physics Division, Na Slovance 2, CZ-180 40, Praha 8, Czech Republic
[13] Dipartimento di Fisica, Università di Genova and INFN, Via Dodecaneso 33, IT-16146 Genova, Italy
[14] Institut des Sciences Nucléaires, IN2P3-CNRS, Université de Grenoble 1, FR-38026 Grenoble Cedex, France
[15] Helsinki Institute of Physics, HIP, P.O. Box 9, FI-00014 Helsinki, Finland
[16] Joint Institute for Nuclear Research, Dubna, Head Post Office, P.O. Box 79, RU-101 000 Moscow, Russian Federation
[17] Institut für Experimentelle Kernphysik, Universität Karlsruhe, Postfach 6980, DE-76128 Karlsruhe, Germany
[18] Institute of Nuclear Physics and University of Mining and Metalurgy, Ul. Kawiory 26a, PL-30055 Krakow, Poland
[19] Université de Paris-Sud, Lab. de l'Accélérateur Linéaire, IN2P3-CNRS, Bât. 200, FR-91405 Orsay Cedex, France
[20] School of Physics and Chemistry, University of Lancaster, Lancaster LA1 4YB, UK
[21] LIP, IST, FCUL - Av. Elias Garcia, 14-1^o, PT-1000 Lisboa Codex, Portugal
[22] Department of Physics, University of Liverpool, P.O. Box 147, Liverpool L69 3BX, UK
[23] LPNHE, IN2P3-CNRS, Univ. Paris VI et VII, Tour 33 (RdC), 4 place Jussieu, FR-75252 Paris Cedex 05, France
[24] Department of Physics, University of Lund, Sölvegatan 14, SE-223 63 Lund, Sweden
[25] Université Claude Bernard de Lyon, IPNL, IN2P3-CNRS, FR-69622 Villeurbanne Cedex, France
[26] Univ. d'Aix - Marseille II - CPP, IN2P3-CNRS, FR-13288 Marseille Cedex 09, France
[27] Dipartimento di Fisica, Università di Milano and INFN, Via Celoria 16, IT-20133 Milan, Italy
[28] Niels Bohr Institute, Blegdamsvej 17, DK-2100 Copenhagen Ø, Denmark
[29] NC, Nuclear Centre of MFF, Charles University, Areal MFF, V Holesovickach 2, CZ-180 00, Praha 8, Czech Republic
[30] NIKHEF, Postbus 41882, NL-1009 DB Amsterdam, The Netherlands
[31] National Technical University, Physics Department, Zografou Campus, GR-15773 Athens, Greece
[32] Physics Department, University of Oslo, Blindern, NO-1000 Oslo 3, Norway
[33] Dpto. Fisica, Univ. Oviedo, Avda. Calvo Sotelo s/n, ES-33007 Oviedo, Spain
[34] Department of Physics, University of Oxford, Keble Road, Oxford OX1 3RH, UK
[35] Dipartimento di Fisica, Università di Padova and INFN, Via Marzolo 8, IT-35131 Padua, Italy
[36] Rutherford Appleton Laboratory, Chilton, Didcot OX11 OQX, UK
[37] Dipartimento di Fisica, Università di Roma II and INFN, Tor Vergata, IT-00173 Rome, Italy

[38] DAPNIA/Service de Physique des Particules, CEA-Saclay, FR-91191 Gif-sur-Yvette Cedex, France
[39] Istituto Superiore di Sanità, Ist. Naz. di Fisica Nucl. (INFN), Viale Regina Elena 299, IT-00161 Rome, Italy
[40] Instituto de Fisica de Cantabria (CSIC-UC), Avda. los Castros s/n, ES-39006 Santander, Spain
[41] Inst. for High Energy Physics, Serpukov P.O. Box 35, Protvino, (Moscow Region), Russian Federation
[42] J. Stefan Institute, Jamova 39, SI-1000 Ljubljana, Slovenia
and Department of Astroparticle Physics, School of Environmental Sciences, Kostanjeviska 16a, Nova Gorica, SI-5000 Slovenia,
and Department of Physics, University of Ljubljana, SI-1000 Ljubljana, Slovenia
[43] Fysikum, Stockholm University, Box 6730, SE-113 85 Stockholm, Sweden
[44] Dipartimento di Fisica Sperimentale, Università di Torino and INFN, Via P. Giuria 1, IT-10125 Turin, Italy
[45] Dipartimento di Fisica, Università di Trieste and INFN, Via A. Valerio 2, IT-34127 Trieste, Italy
and Istituto di Fisica, Università di Udine, IT-33100 Udine, Italy
[46] Univ. Federal do Rio de Janeiro, C.P. 68528 Cidade Univ., Ilha do Fundão BR-21945-970 Rio de Janeiro, Brazil
[47] Department of Radiation Sciences, University of Uppsala, P.O. Box 535, SE-751 21 Uppsala, Sweden
[48] IFIC, Valencia-CSIC, and D.F.A.M.N., U. de Valencia, Avda. Dr. Moliner 50, ES-46100 Burjassot (Valencia), Spain
[49] Institut für Hochenergiephysik, Österr. Akad. d. Wissensch., Nikolsdorfergasse 18, AT-1050 Vienna, Austria
[50] Inst. Nuclear Studies and University of Warsaw, Ul. Hoza 69, PL-00681 Warsaw, Poland
[51] Fachbereich Physik, University of Wuppertal, Postfach 100 127, DE-42097 Wuppertal, Germany
[52] On leave of absence from IHEP Serpukhov
[53] Now at University of Florida

Appendix B

Track Parameterization

Several track parameterizations are used in DELPHI. During the track reconstruction, TER and TKR forms are used (stored in the TE and TK TANAGRA banks respectively). For track extrapolation and fitting, the EXX form is used. The **perigee parameters** define the track at its point of closest approach to a reference point (usually the origin). Because the reference point is implicit, only five parameters are required. The other parameterizations also define the distance from the origin (in either R or z) at which they apply. It is the perigee parameters and their weight matrix (inverse covariance matrix) that are stored on the DST and used in most of the subsequent analysis.

TER	$(R, R\Phi, z, \theta, \phi, -q/p_{xy})$	or	$(x, y, z, \theta, \phi, -q/p_{xy})$	
TKR	$(R, R\Phi, z, \theta, \phi, -q/p)$	or	$(x, y, z, \theta, \phi, -q/p)$	
EXX	$(R, \Phi, z, \theta, \beta, \kappa)$	or	$(z, x, y, \theta, \phi, \kappa)$	*[sic]*
Perigee	$(\epsilon, z, \theta, \phi, \kappa)$			

The parameters (R, Φ, z) are the cylindrical position coordinates and (x, y, z) are the Cartesian position coordinates (in cm). The cylindrical forms are used mostly in the barrel and the Cartesians mostly in the endcaps. θ and ϕ are, respectively, the polar and azimuthal track directions at the specified point. β is the azimuthal angle, relative to a radial track ($\beta \equiv \phi - \Phi$). All angles are in radians.

The particle's momentum components are given by

$$\begin{aligned} p_x &= p\sin\theta\cos\phi & (0 \le \phi < 2\pi) \\ p_y &= p\sin\theta\sin\phi & (0 \le \theta < \pi) \\ p_z &= p\cos\theta & p_{xy} = p\sin\theta \end{aligned} \tag{B.1}$$

p is the momentum (in GeV/c), q the charge (relative to that of the proton), and κ the track curvature (in cm^{-1}), i.e. in the central region, where the magnetic field is parallel to the z-axis,

$$\kappa \equiv 1/\rho = -qB/p_{xy}\,, \tag{B.2}$$

where $|\rho|$ is the track's radius of curvature in the xy plane, and B is the magnetic field (1.2 tesla = 0.0036 GeV/c/cm).

ϵ is the **geometric impact parameter**, whose magnitude gives the distance from the origin (or other reference point) to the **perigee**, the point of the track's closest approach in the xy plane. The sign of ϵ is positive if the track passes to the right of the origin, when looking along $-z$ (see figure B.1).[1] Formally,

$$\epsilon = (\mathbf{x_0} \times \hat{\mathbf{p}}) \cdot \hat{\mathbf{z}} \tag{B.3}$$

where $\mathbf{x_0}$ is the vector from the origin to the perigee, $\hat{\mathbf{p}}$ is a unit vector along the track direction there, and $\hat{\mathbf{z}}$ is a unit vector along the z-axis. The position of the perigee is thus given by

$$(x_0, y_0, z_0) = (\epsilon\sin\phi, -\epsilon\cos\phi, 0) \tag{B.4}$$

For lifetime studies, it is often convenient to use another signing convention: the **lifetime-signed impact parameter**. In this case, a positive sign is assigned if

[1] It is common (eg. [66]) to define the sign of ϵ in terms of the track curvature (whether the origin is enclosed by the track), with an additional sign for a positively charged particle. Although equivalent to the one given above, such a definition engenders the incorrect implication that the track's charge plays a rôle, whereas in fact ϵ is equally applicable to neutral tracks.

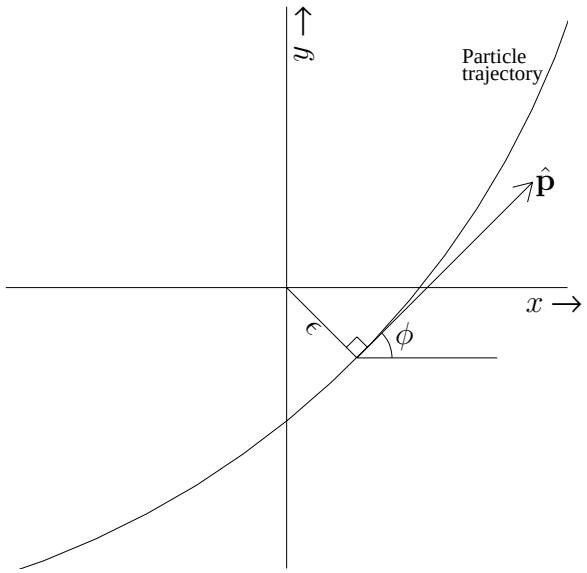

Figure B.1: Illustration of the track impact parameter. In this case, the impact parameter, ϵ, and curvature, κ, are positive. Since DELPHI's magnetic field is parallel to the z-axis (pointing out of the paper), $\kappa > 0$ corresponds to a negatively charged particle.

the track intersects the direction vector (often estimated from the thrust axis) of a presumed decaying particle in front of the reference point (usually the beamspot or reconstructed primary vertex). For a large boost, the average lifetime-signed impact parameter is proportional to the decay lifetime [154]. Since we can reconstruct the J/ψ vertex directly, this method and the lifetime signing convention are not used in this thesis.

Appendix C

G64 crates and Elementary Processes

Partition	G64 s/w	EP name	EP s/w	Channels #	Channels type	Channels m/c	Function
VD	S	FB	S	6	digital	m/c	Fastbus crate power supplies
		PWON	S	1	digital	c	Bias voltage control
		VOLT	S	576	analog	m	Bias voltages and leakage currents
	S	TEMP	S	16	analog	m	Temperatures. A high temperature interlocks the power supplies.
ID	–	HV_FS	M	13	'CAEN'	m/c	Field shaping and jet/trigger chamber high voltages supplied by Lecroy units. These are controlled via RS232–C by special processes on the VAX, which emulate G64s controlling CAEN power supplies, allowing standard EPs with minimal changes to be used.
	–	HV_JT*	M	34	'CAEN'	m/c	
	S	HV_DVM	S	24	analog	m	Field shaping high voltages monitored via a digital voltmeter
		FB	S	21	digital	m/c	Fastbus crate power supplies
		LV	S	9	analog	m	Low voltages
		TEMP	S	16	analog	m	Temperatures

(PTO)

Table C.1: G64 crates and Elementary Processes used by each detector partition in 1994 (the 1995 configuration, despite the new Inner Detector, was practically identical). A brief description of each detector partition's slow controls is given in section 3.2. The Elementary Process names are used as object names for SMI. If they are marked with an asterisk (*), then the EP controls high voltages which must be lowered during LEP filling and high background conditions. The detector-monitoring G64 and VAX Elementary Process software is indicated as being a **S**tandard, **M**odified, or **P**artition-specific program in the *s/w* columns. Elementary Processes that perform monitoring only (*m*), control only (*c*), or both monitoring and control (*m/c*) are indicated in the *m/c* column.

Partition	G64 s/w	EP name	EP s/w	Channels #	Channels type	Channels m/c	Function
TPC	P	CAEN*	P	89	CAEN	m/c	Sense wire high voltages and drift field very high voltages. The high voltages are automatically reduced if the currents are too high.
		TEMP	P	98	analog	m	Temperatures and pressures
	P	PREAMP_B	P	21	digital	c	Wire and B-side pad preamplifiers
				42	analog	m	
		FB_B	P	138	digital	m/c	B-side fastbus crate power supplies
				230	analog	m	
	P	PREAMP_D	P	15	digital	c	D-side pad preamplifiers
				30	analog	m	
		FB_D	P	99	digital	m/c	D-side fastbus crate power supplies
				165	analog	m	
	P	GATES	P	38	digital	m/c	Gating grid
		CALGEN	P	36	digital	m/c	Calibration generators
OD	S	HVAN*	S	26	CAEN	m/c	Anode high voltages
		FBUS	S	18	digital	m/c	Fastbus crate power supplies
	S	CRTE	S	78	analog	m	Crate voltages and temperatures
		PLNK	S	196	analog	m	Plank positions and temperatures
FCA	M	HV_B*	M	24	CAEN	m/c	High voltages with automatic trip recovery and grouped ramping
		FB	S	12	digital	m/c	Fastbus crate power supplies
FCB	M	HV_A*	M	24	CAEN	m/c	A-side high voltages with automatic trip recovery and grouped ramping
		FB_A	S	12	digital	m/c	A-side fastbus crate power supplies
		LV	S	2	analog	m	Low voltage supplies
	M	HV_C*	M	20	CAEN	m/c	C-side high voltages (similar to HV_A)
		FB_C	S	12	digital	m/c	C-side fastbus crate power supplies
HPC	S	HV*	P	144	CAEN	m/c	Proportional chamber and drift field high voltages
				144	analog	m	
				3	digital	c	
	S	TEMP	S	144	analog	m	Temperatures
	P	LV	P	168	analog	m	Preamplifier and shaper low voltages
		FB	P	24	analog	m	Fastbus crate power supplies
		DV	P	49	analog	m	Gas test chamber drift velocity and pulse heights
		PH	P	49	analog	m	
SCI	–[1]	THV	P	170	CAEN	m/c	Phototube high voltages

(PTO)

Table C.1 (cont.)

[1] SCI uses HPC low voltage G64 crate.

Partition	G64 s/w	EP name	EP s/w	Channels #	Channels type	Channels m/c	Function
EMF	P	HV_A	P	4	digital	c	A-side High voltages
				1280	analog	m	
		LV_A	P	64	digital	m	A-side Low voltages
		FB_A	P	16	digital	m/c	A-side Fastbus crate power supplies
				8	analog	m	
		TEMP_A	P	128	analog	m	A-side Temperatures
	P	HV_C	P	4	digital	c	C-side High voltages
				1280	analog	m	
		LV_C	P	64	digital	m	C-side Low voltages
		FB_C	P	16	digital	m/c	C-side Fastbus crate power supplies
				8	analog	m	
		TEMP_C	P	128	analog	m	C-side Temperatures
HAC	M	HVBA	S	24	CAEN	m/c	Barrel A-side high voltages with automatic trip recovery
		PLBA	M	480	analog	m	Barrel A-side high voltage current monitoring. Individual Planes can be switched off by the G64 if too much current is drawn. Analog and digital channels combined in the G64.
					digital	c	
		HVBC	S	24	CAEN	m/c	Barrel C-side high voltages with automatic trip recovery
		PLBC	M	480	analog	m	Barrel C-side high voltage current monitoring (similar to PLBA)
					digital	c	
	M	HVFA	S	24	CAEN	m/c	Endcap A-side high voltages with automatic trip recovery
		PLFA	M	480	analog	m	Endcap A-side high voltage current monitoring (similar to PLBA)
					digital	c	
		HVFC	S	24	CAEN	m/c	Endcap C-side high voltages with automatic trip recovery
		PLFC	M	480	analog	m	Endcap C-side high voltage current monitoring (similar to PLBA)
					digital	c	
	S	LVBA	S	6	digital	m/c	Barrel A-side low voltage supplies
		LVFA	S	6	digital	m/c	Endcap A-side Low voltage supplies
		LVBC	S	6	digital	m/c	Barrel C-side low voltage supplies
		LVFC	S	6	digital	m/c	Endcap C-side Low voltage supplies
		FBUS	S	3	digital	m/c	Fastbus crate power supplies
	P	STR_A	P	2	analog	m	Endcap A-side gas test streamer tubes
		STR_B	P	4	analog	m	Barrel gas test streamer tubes
		STR_C	P	2	analog	m	Endcap C-side gas test streamer tubes

(PTO)

Table C.1 (cont.)

Partition	G64 s/w	EP name	EP s/w	Channels #	Channels type	Channels m/c	Function
RIB	S	HV_A*	M	108	CAEN	m/c	A-side MWPC high voltages. Ramping triggered by hardwired signal directly from G64 to CAEN.
				1	digital	c	
		CRAT	S	52	digital	m/c	Fastbus crate power supplies
	S	HV_C*	M	108	CAEN	m/c	C-side MWPC high voltages (similar to HV_A)
				1	digital	c	
	M	VHV	P	9	digital	m/c	Drift cage currents. Heinzinger very high voltage unit is controlled via GPIB bus.
	P			81	analog	m	
	P	HEATING	P	64	digital	m/c	Barrel heating and temperatures
				118	analog	m	
	P			118	analog	m	
	P			32	digital	c	Heating of gas pipes, racks, and other devices outside the barrel
				102	analog	m	
	P[2]	DRI	P	117	digital	m/c	Drift gas flow, pressures, temperatures, and TMAE
				24	analog	m	
	P[2]	MON	P	52	digital	m/c	Drift gas quality
				8	analog	m/c	
	P[2]	GAS	P	70	digital	m	Gas radiator
				34	analog	m	
	P[2]	LIQ	P	130	digital	m/c	Liquid radiator
				11	analog	m	
RIF	S	HV_A*	S	52	CAEN	m/c	A-side MWPC high voltages and drift field very high voltages
		UV_A	S	12	CAEN	m/c	A-side calibration ultraviolet lamps
	M	TV_A	S	42	analog	m	A-side vessel temperatures with interlock to stop TMAE flow if too cool
				1	digital	c	
		FB_A	S	48	analog	m	A-side fastbus crate power supplies and preamplifier temperatures. Crates switched off from G64 if too hot.
				27	digital	m/c	
	S	HV_C*	S	52	CAEN	m/c	C-side MWPC high voltages and drift field very high voltages
		UV_C	S	12	CAEN	m/c	C-side calibration ultraviolet lamps
	M	TV_C	S	42	analog	m	C-side vessel temperatures (similar to TV_A)
				1	digital	c	
		FB_C	S	48	analog	m	C-side fastbus crate power supplies and preamplifier temperatures (similar to FB_A)
				27	digital	m/c	
	P[2]	DRI	P	123	digital	m/c	Drift gas
				35	analog	m	

(PTO)

Table C.1 (cont.)

[2]The RICH fluid systems are controlled by Siemens systems which perform a function analagous to that of the G64s.

Partition	G64 s/w	EP name	EP s/w	Channels #	Channels type	Channels m/c	Function
MUB	S	HV_B	M	52	CAEN	m/c	B-side high voltages with automatic trip recovery and conditioning of frequently-tripping channels. Ramping is done in steps with continuous monitoring. Volts are lowered if gas problems.
		LV_B	S	31	analog	m	B-side low voltages
		FB_B	S	1	analog	m	B-side fastbus crate power supply
				1	digital	c	
	S	HV_D	M	48	CAEN	m/c	D-side high voltages (similar to HV_B)
		LV_D	S	31	analog	m	D-side low voltages
		FB_D	S	1	analog	m	D-side fastbus crate power supply
				1	digital	c	
MUF	M	HV_A*	M	16	CAEN	m/c	A-side high voltages. Anode voltages supplied by CAEN. EP provides automatic trip recovery, and adjusts voltage levels according to the atmospheric pressure. Field grading supply status controlled and monitored; voltage values monitored.
				50	digital	m/c	
				2	analog	m	
		LV_A	S	8	digital	m	A-side low voltage power supply status
		FB_A	S	4	digital	m/c	A-side fastbus crate power supplies
	M	HV_C*	M	16	CAEN	m/c	C-side high voltages (similar to HV_A)
				50	digital	m/c	
				2	analog	m	
		LV_C	S	8	digital	m	C-side low voltage power supply status
		FB_C	S	4	digital	m/c	C-side fastbus crate power supplies
HOF	–[3]	HV_A	M	16	CAEN	m/c	A-side high voltages
	–[3]	HV_C	M	16	CAEN	m/c	C-side high voltages
MUS	S	HV_A	S	16	CAEN	m/c	A-side high voltages
		HV_C	S	16	CAEN	m/c	C-side high voltages
TOF	S	VOLT	S	88	CAEN	m/c	Photomultiplier high voltages
		FB	S	9	digital	m/c	Fastbus crate power supplies

(PTO)

Table C.1 (cont.)

[3] HOF uses MUF G64/CAEN crates.

Partition	G64 s/w	EP name	EP s/w	Channels #	Channels type	Channels m/c	Function
SAT[4]	M	BIAS	M	4	analog	m/c	Calorimeter bias voltages and currents
		SWST	S	1	digital	m	Bias supply status
		FB	S	4	digital	m/c	Fastbus crate power supplies
		TEMP	S	10	analog	m	Temperatures
STIC	M	HV_C*	S	2	'CAEN'	m/c	Calorimeter high voltages. G64 emulates a CAEN high voltage unit controlling voltages and currents for each endcap.
		HV_E	S	370	analog	m	Individual calorimeter phototetrode currents and statuses
				21	digital	m	
	–[5]	BIAS	M	6	analog	m/c	Bias voltages, currents, and status
				2	digital	m/c	
		HV_V*	S	3	digital	m/c	Veto counter photomultiplier high voltages
		POSI	S	22	analog	m	Positions
		TEMP	S	96	analog	m	Temperatures
		FB	S	6	digital	m/c	Fastbus crate power supplies
VSAT	–[5]	BIAS	M	20	analog	m/c	Bias voltages and currents
		SWST	S	3	digital	m	Bias supply statuses
		FB	S	2	digital	m/c	Fastbus crate power supply

(PTO)

Table C.1 (cont.)

[4]The SAT was replaced by the STIC in 1994.

[5]The VSAT and STIC (BIAS and FB) use G64 hardware and software originally developed for the SAT.

Partition	G64 s/w	EP name	EP s/w	Channels #	Channels type	Channels m/c	Function
D1[6]	S	AIR	S	4	analog	m	Air conditions
		BTEM	S	32	analog	m	Barrel temperatures
		H2OM	S	3	analog	m	Cooling water
		FBD1	S	48	digital	m/c	Central data acquisition fastbus crate power supplies
				150	analog	m	
TP	–[7]	FB	S	6	digital	m/c	Trigger partition fastbus crate power supplies
Gas[8]	P[9]	GAS_ALARM	P	730	analog	m/c	Accepts messages from 28 of the gas-system G64s and sets SMI states and injects EMU messages based on the conditions in each partition
				563	digital	m/c	
GSS[8]	–	G_TO_D	P	~ 400	–	m	Transfers GSS-detected conditions to DELPHI (SMI and EMU)
Sol[8]	P	SELTEK_RECEIVE and LOG	P	60	Seltek	m	Solenoid temperatures, currents, strains, and field measured using a Seltek data logger
	P	NMR	P	5	analog	m	NMR field measurements
	P	SOL_ALARM	P	103	–	m	Power supply and vacuum system alarm handling. Control reserved for separate interactive programs.
	P	PRESSURE_LOG	P	16	analog	m	Cryostat pressures

Table C.1 (cont.)

Notes

1. Apart from the SAT, the configuration described here was in operation from the start of 1994 datataking.
2. Table 3.2 lists the numbers of G64 crates used by each detector partition. Here we specify the software running in each, and so G64 crates whose backplanes are chained together using a single CPU are counted together.
3. Processes have only been included in this table if they perform an action analagous to the standard Elementary Processes, ie. each is the lowest-level VAX process for interpretation of the hardware in terms of an SMI object. Thus a few partition-specific software monitoring processes (eg. jobs to check that other jobs are running) and interface programs have been excluded, even if they have associated SMI objects.
4. Elementary Processes are marked as modified (M) only for instances that actually make use of the modification. For example the VSAT FB and SWST EPs run the same program as the BIAS, but the modifications to the standard EP that this has only apply to bias channels.
5. The number of channels given are as seen by the Elementary Processes, where each channel performs independent monitoring or control of a specific piece of hardware. Thus, most notably, the two PIA channels used to switch on and off a fastbus crate power supply's DC are counted as one, since the G64 Skeleton controls both channels based on EP commands for a single channel.

[6]The G64 crate in barrack D1 is used to monitor general environmental conditions.
[7]The trigger partition uses the FCA G64 crate.
[8]The gas, GSS, and Solenoid systems are described in section 3.9.
[9]There are 34 G64s in the gas-system, though the 6 supervisors do not communicate with GAS_ALARM.

Appendix D

Fitting Methods

We fit $f(x;\mathbf{p})$ to be proportional to the probability density function for N measurements $x_i,\ldots,x_N$ in the range $x_0 \le x_i < x_h$. The fit parameters are $\mathbf{p}$. $f(x;\mathbf{p})$ is normalized such that $\int_{x_0}^{x_h} f(x;\mathbf{p})dx \equiv A(\mathbf{p})$.

D.1 Unbinned Extended Maximum Likelihood Fit

The normalized likelihood of each event is $f(x_i;\mathbf{p})/A(\mathbf{p})$. We can assume a Poisson variation for the measured number of events, N, about some true mean value, which we require our fitted function to be normalized to by taking as $A(\mathbf{p})$. The likelihood of obtaining this set of events is thus

$$\mathcal{L}_u(\mathbf{p}) = \frac{A(\mathbf{p})^N e^{-A(\mathbf{p})}}{N!} \prod_{i=1}^{N} \frac{f(x_i;\mathbf{p})}{A(\mathbf{p})}\,. \tag{D.1}$$

It is more convenient to work with the negative log-likelihood

$$\mathcal{F}_u(\mathbf{p}) \equiv -\ln \mathcal{L}_u(\mathbf{p}) = -\sum_{i=1}^{N} \ln\left(\frac{f(x_i;\mathbf{p})}{A(\mathbf{p})}\right) - N\ln A(\mathbf{p}) + A(\mathbf{p}) + \ln N! \tag{D.2}$$

which has its minimum at the same parameter values, $\mathbf{p}$, as the maximum of the likelihood, $\mathcal{L}_u$. Dropping the constant term, $\ln N!$, and cancelling the $N\ln A(\mathbf{p})$

terms, we have

$$\mathcal{F}_u(\mathbf{p}) = -\sum_{i=1}^{N} \ln f(x_i;\mathbf{p}) + A(\mathbf{p}) \tag{D.3}$$

as our function to minimize with respect to $\mathbf{p}$.

D.2 Unbinned Maximum Likelihood Fit

If we now define $f'(x;\mathbf{p}) \equiv f(x;\mathbf{p})/A(\mathbf{p})$, so that $f'(x;\mathbf{p})$ is normalized to 1, we obtain the standard Maximum Likelihood function

$$\mathcal{F}'_u(\mathbf{p}) = -\sum_{i=1}^{N} \ln f'(x_i;\mathbf{p})\,. \tag{D.4}$$

This is the desired function if the experiment is performed such that a fixed number of events are taken (and hence we do not use the Poisson factor in equation D.1) rather than taking everything that comes within the time interval allotted.

The normalization of $f'(x;\mathbf{p})$ can be any constant (with respect to $\mathbf{p}$), not just 1, since this would merely introduce an additive constant which will not change the fit results, just the value of $\mathcal{F}'_u(\mathbf{p})$ at the minimum.

Computationally, if $\mathcal{F}'_u(\mathbf{p})$ cannot be minimized analytically, the standard Maximum likelihood method is usually more difficult, since here we must calculate the normalization, $A(\mathbf{p})$, for every set of values, $\mathbf{p}$, that we visit.

D.3 Binned Maximum Likelihood Fit

If we have M bins with a constant bin-width of $h \equiv \frac{x_h - x_0}{M}$, then the measured contents of bin b ($b = 1 \ldots M$) will be

$$n_b = \int_{x_0+h(b-1)}^{x_0+hb} \sum_{i=1}^{N} \delta(x - x_i)dx\,, \tag{D.5}$$

while the fitted bin contents will be

$$f_b(\mathbf{p}) = \int_{x_0+h(b-1)}^{x_0+hb} f(x;\mathbf{p})dx\,. \tag{D.6}$$

In this case we do not have to normalize $f(x;\mathbf{p})$. This is because it is now simply a parameterization of the shape — and height — of the histogram, and need not be interpreted as a probability density function.

If we assume a Poisson distribution for the number of events in each bin, n_b, the histogram likelihood is

$$\mathcal{L}_b(\mathbf{p}) = \prod_{b=1}^{M} \frac{f_b^{n_b} e^{-f_b}}{n_b!} \tag{D.7}$$

(taking $f_b \equiv f_b(\mathbf{p})$), giving

$$\mathcal{F}_b(\mathbf{p}) \equiv -\ln \mathcal{L}_b(\mathbf{p}) = -\sum_{b=1}^{M} (n_b \ln f_b - f_b - \ln n_b!)\,. \tag{D.8}$$

$\sum_{b=1}^{M} f_b$ is simply $A(\mathbf{p})$ (the fitted contents of all bins). $\sum_{b=1}^{M} \ln n_b!$ is independent of $\mathbf{p}$, and does not alter the fit result. Ignoring this constant, we obtain the function to minimize

$$\mathcal{F}_b(\mathbf{p}) = -\sum_{b=1}^{M} n_b \ln f_b + A(\mathbf{p})\,. \tag{D.9}$$

The final term may be dropped if, as in the standard Maximum Likelihood fit, the function normalization is independent of the fit parameters.

We now see how this is related to the unbinned case by expanding the definitions of n_b and f_b (equations D.5 and D.6)

$$\mathcal{F}_b(\mathbf{p}) = -\sum_{b=1}^{M} \left[\int_{x_0+h(b-1)}^{x_0+hb} \sum_{i=1}^{N} \delta(x-x_i)dx\right] \left[\ln\left(\int_{x_0+h(b-1)}^{x_0+hb} f(x;\mathbf{p})dx\right)\right] + A(\mathbf{p})\,. \tag{D.10}$$

If $f(x;\mathbf{p})$ is approximately constant over a bin, then we can replace $\int_{x_0+h(b-1)}^{x_0+hb} f(x;\mathbf{p})dx$ by $hf(x_0+h(b-\frac{1}{2});\mathbf{p})$ which, being a constant, can be moved inside the first integral.

But those limits are the same, so we can replace $x_0 + h(b - \frac{1}{2})$ by x again.

$$\mathcal{F}_b(\mathbf{p}) \approx -\sum_{b=1}^{M} \int_{x_0+h(b-1)}^{x_0+hb} \sum_{i=1}^{N} \delta(x - x_i) \ln[hf(x;\mathbf{p})]dx + A(\mathbf{p}) \tag{D.11}$$

$$= -\sum_{i=1}^{N} \int_{x_0}^{x_h} \delta(x - x_i) \ln[hf(x;\mathbf{p})]dx + A(\mathbf{p}) \tag{D.12}$$

$$= -\sum_{i=1}^{N} \ln[hf(x_i;\mathbf{p})] + A(\mathbf{p}) \tag{D.13}$$

$$= -\sum_{i=1}^{N} \ln f(x_i;\mathbf{p}) + A(\mathbf{p}) - N \ln h \tag{D.14}$$

and dropping the final constant term we obtain the same expression as for the unbinned extended log-likelihood, $\mathcal{F}_u(\mathbf{p})$, in equation D.3.

Hence, when the function does not vary much over a bin, we have shown that the binned Maximum Likelihood fit gives us the same results as the unbinned Extended Maximum Likelihood fit. Note that in this approximation, the definition of $f_b(\mathbf{p})$ (equation D.6) becomes $f(x_0 + h(b - \frac{1}{2}); \mathbf{p})$ and $A(\mathbf{p})$ its sum over all the bins which, for simplicity, is what is often used in a binned fit.

D.4 Binned χ^2 Fit

If the expected number of events in each bin is large, then we may approximate the Poisson distribution in equation D.7 by a Gaussian with mean f_b and variance f_b [155, page 40].

$$\mathcal{L}_{\chi^2}(\mathbf{p}) = \prod_{b=1}^{M} \frac{1}{\sqrt{2\pi f_b}} e^{-(n_b - f_b)^2/2f_b} \tag{D.15}$$

giving

$$\mathcal{F}_{\chi^2}(\mathbf{p}) \equiv -\ln \mathcal{L}_{\chi^2}(\mathbf{p}) = -\sum_{b=1}^{M} \ln \frac{1}{\sqrt{2\pi f_b}} + \frac{1}{2} \sum_{b=1}^{M} \frac{(n_b - f_b)^2}{f_b}\,. \tag{D.16}$$

If the fitted bin contents, f_b, is large enough, then it may be approximated by the measured bin contents, n_b, in the first term which is then independent of the fit

parameters, and we obtain the well-known χ^2 formula[1]

$$\chi^2 \equiv -2 \ln \mathcal{L}_{\chi^2}(\mathbf{p}) = \sum_{b=1}^{M} \frac{(n_b - f_b)^2}{f_b} \,. \tag{D.17}$$

Thus the χ^2 fit to a histogram assumes that the fitted number of events in each bin is large.

[1] [156, page III.36, equation 2.9] gives this incorrectly as $\chi^2 \equiv -\frac{1}{2} \ln \mathcal{L}_{\chi^2}(\mathbf{p})$, so maybe it isn't all that well known! (It is corrected in [157, equation 17.10].)

References

[1] P.R. Collins, *A Study of* J/ψ *Production and a Measurement of the Mean B Hadron Lifetime at the* Z^0 *Resonance,* doctoral thesis, University of Oxford, RAL report **RALT–024,** August 1994.

[2] Particle Data Group, R.M. Barnett *et al.*, *Review of Particle Physics,* Phys. Rev. **D54** (1996).

[3] I.I. Bigi, *Heavy Quark Expansions for Inclusive Heavy Flavor Decays and the Lifetimes of Charm and Beauty Hadrons,* Proc. Workshop on Heavy Quarks at Fixed Target (HQ'96, St. Goar, October 1996); and UND-HEP Report **96-BIG06**, November 1996.

[4] M. Neubert, *Theory of Beauty Lifetimes,* Proc. 2nd Conference on B Physics and CP Violation, (Honolulu, March 1997); and CERN/TH Preprint **97–148**, 3rd July 1997.

[5] LEP B lifetimes working group, *Averages of B Hadron Lifetimes,* Unpublished draft for 1998 Review of Particle Physics, 30th March 1998.

[6] G. Alexander *et al., Prompt* J/ψ *Production in Hadronic* Z^0 *Decays,* Phys. Lett. **B384** (1996) 343–352.

[7] P. Cho, *Prompt Upsilon and Psi Production at LEP,* Phys. Lett. **B368** (1996) 171–178.

[8] K. Hagiwara, A.D. Martin, W.J. Stirling, J/ψ *Production from Gluon Jets at LEP,* Phys. Lett. **B267** (1993) 527–531; Erratum ibid. **B316** (1993) 631.

[9] P. Cho and A.K. Leibovich, *Color-Octet Quarkonia Production,* Phys. Rev. **D53** (1996) 150–162.

[10] P. Cho and A.K. Leibovich, *Color-Octet Quarkonia Production II,* Phys. Rev. **D53** (1996) 6203–6217.

[11] K. Cheung, W–Y Keung, T. Yuan, *Color-Octet Quarkonium Production at the Z Pole,* Phys. Rev. Lett. **76** (1996) 877–880.

[12] CDF Collaboration, *Production of Heavy Quark States at CDF,* Proc. 30th Rencontres de Moriond: QCD and High-energy Hadronic Interactions (Meribel les Allues, March 1995), ed. J. Tran Thanh Van, Editions Frontieres, 1995.

[13] ALEPH: D. Decamp *et al., ALEPH: A Detector for Electron–Positron Annihilations at LEP,* Nucl. Instr. and Meth. **A294** (1990) 121–178.

[14] DELPHI: P. Aarnio *et al., The DELPHI Detector at LEP,* Nucl. Instr. and Meth. **A303** (1991) 233–276.

[15] L3: B. Adeva *et al., The Construction of the L3 Experiment,* Nucl. Instr. and Meth. **A289** (1990) 35–102.

[16] OPAL: K. Ahmet *et al., The OPAL Detector at LEP,* Nucl. Instr. and Meth. **A305** (1991) 275–319.

[17] (a) *LEP Design Report*, CERN/LEP report **84–01**, June 1884.

(b) S. Myers, *The LEP Collider, from Design to Approval and Commissioning,* Sixth John Adams Memorial Lecture, CERN report **91–08**, 10th October 1991.

[18] G. Arduini *et al., LEP1 Operation, 1989–1995,* Proc. 5th European Particle Accelerator Conference (EPAC'96, Sitges, June 1996), CERN/SL preprint **96–43**, June 1996.

[19] R. Bailey *et al., The Pretzel Separation Scheme in LEP,* Proc. 15th International Conference on High Energy Accelerators (HEACC'92, Hamburg, July 1992), ed. J. Rossbach, Int. J. Mod. Phys. A, (Proc. Suppl.) **2A** (1993) 401–404.

[20] P. Collier, B. Goddard, M. Lamont, *Operation of LEP with Bunch Trains,* Proc. 5th European Particle Accelerator Conference (EPAC'96, Sitges, June 1996), CERN/SL preprint **96–22**, 26th June 1996.

[21] H.J. Hilke, *DELPHI Coordinate System,* CERN/DELPHI note **84–40** GEN–10, 21st June 1984.

[22] DELPHI Collaboration, *DELPHI Technical Proposal,* CERN/LEPC **83–3**, 17th May 1983.

[23] DELPHI Collaboration, *Performance of the DELPHI Detector,* Nucl. Instr. and Meth. **A378** (1996) 57–100.

[24] N. Bingefors *et al., The DELPHI Microvertex Detector,* Nucl. Instr. and Meth. **A328** (1993) 447–471.

[25] V. Chabaud *at al., The DELPHI Silicon Strip Microvertex Detector with Double Sided Readout,* Nucl. Instr. and Meth. **A368** (1996) 314–332.

[26] V. Chabaud, A. Andreazza, P. Collins, H. Dijkstra, *Alignment of the DELPHI vertex detector,* CERN/DELPHI note **95–177** MVX–10, 12th December 1995.

[27] T. Adye, *Vertex Detector Event Display and Slow Controls for the DELPHI Experiment,* First Year DPhil Report, Oxford University, 22nd June 1990.

[28] T. Adye *et al., Vertex Detector Routines,* chapter 11 in *DST Analysis Libraries Writeup,* ed. P.D. Dauncey and L. Mirabito, unpublished CERN/DELPHI note, 15th May 1997.

[29] F. Hartjes *et al., A Drift Chamber With Variable Drift Velocity,* Nucl. Instr. and Meth. **A256** (1987) 55–64.

[30] M. Ŝiket, *An investigation of the properties and behaviour of the straw detector, DELPHI,* CERN/DELPHI note **95–156** TRACK-83, 17th October 1995.

[31] (a) C. Brand *et al., The DELPHI Time Projection Chamber,* Proc. IEEE Nuclear Science Symposium (Orlando, November 1988), ed. R. Pordes, IEEE Trans. Nucl. Sci. **36** (1989) 122–126.

(b) Y. Sacquin, *The DELPHI Time Projection Chamber,* Proc. 6th International Wire Chamber Conference (Vienna, February 1992), ed. W. Bartl *et al.,* Nucl. Instr. and Meth. **A323** (1992) 209–212.

[32] A. Amery *et al., The DELPHI Outer Detector,* Proc. 5th International Wire Chamber Conference (Vienna, February 1989), ed. W. Bartl *et al.,* Nucl. Instr. and Meth. **A283** (1989) 502–508.

[33] (a) E.G. Anassontzis *et al., The Barrel Ring Imaging Cerenkov Counter of DELPHI,* Proc. 6th International Wire Chamber Conference (Vienna, February 1992), ed. W. Bartl *et al.,* Nucl. Instr. and Meth. **A323** (1992) 351–362.

(b) W. Adam *et al.,* Nucl. Instr. and Meth. **A343** (1994) 68.

(c) DELPHI RICH Collaboration, contributions to the Second Workshop on RICH Detectors (Uppsala 1995).

[34] W. Adam *et al., The Forward Ring Imaging Cerenkov Detector of DELPHI,* Nucl. Instr. and Meth. **A338** (1994) 284–309.

[35] (a) W.T. Meyer, *The DELPHI High Density Projection Chamber,* Proc. IEEE Nuclear Science Symposium (Orlando, November 1988), ed. R. Pordes, IEEE Trans. Nucl. Sci. **36** (1989) 352–356.

(b) A. Algeri *et al., Performance of the HPC Calorimeter in DELPHI,* Proc. Nuclear Science Symposium and Medical Imaging Conference (Norfolk, October 1994), ed. E. Barsotti, IEEE Trans. Nucl. Sci. **42** (1995) 491–498.

[36] K. Doroba *et al., Design and Tests of the Scintillator Trigger counters with Plastic Fibre Read out for the DELPHI Detector,* CERN/DELPHI note **88–26** CAL–58, 26th April 1988.

[37] P. Checchia *et al., Performance of the Forward Electromagnetic Calorimeter (FEMC) for the End Caps of the DELPHI Detector,* Nucl. Instr. and Meth. **A275** (1989) 49–58.

[38] G.D. Alekseev *et al., Studies of the Stability and Systematics of Operation of the DELPHI Plastic Streamer Tubes,* Nucl. Instr. and Meth. **A292** (1990) 551–562.

[39] I. Ajinenko *et al., The cathode read-out of the DELPHI hadron calorimeter,* Proc. Nuclear Science Symposium and Medical Imaging Conference (Norfolk, October 1994), ed. E. Barsotti, IEEE Trans. Nucl. Sci. **42** (1995) 485–490.

[40] (a) T.A. Fearnley, *Study of the Performance of the Drift Chambers for the LEP/DELPHI Muon Detector,* masters thesis, University of Oxford, RAL Report **RALT–049,** August 1987.

(b) A.C. Pinsent, *The Barrel Muon Chambers,* section 2.5 in *A Study of Leptonic Decay Channels at the* Z^0 *Resonance Peak,* doctoral thesis, University of Oxford, RAL report **RALT–116,** November 1990.

(c) N.C.E. Crosland, *The Barrel Muon Detector,* chapter 3 in *Studies of Muon-Pair Production in* e^+e^- *Annihilations at the LEP Collider,* doctoral thesis, University of Oxford, RAL report **RALT–117,** January 1991.

[41] J. Buytaert *et al., The Forward Muon Detector of the DELPHI Experiment at LEP,* Nucl. Instr. and Meth. **A310** (1991) 596–606.

[42] DELPHI Collaboration, *Proposal for the DELPHI Surround Muon Chambers,* CERN/DELPHI note **92–139** TRACK–71, 21st October 1992.

[43] J.M. Benlloch *et al., Physical Properties of the Time of Flight Scintillation Counters of DELPHI,* Nucl. Instr. and Meth. **A290** (1990) 327–334.

[44] F. Stichelbaut, *Study of the Performance of the 40° counters with the 94 Data,* CERN/DELPHI note **96–18** HERM–2, 22nd February 1996.

[45] S. Simonetti, *Study of the HPC* 90° *counters,* CERN/DELPHI note **93–142** CAL–111, 9th December 1993.

[46] S.J. Alvsvåg *et al., The SAT calorimeter of the DELPHI experiment at LEP: Results of a module test,* Nucl. Instr. and Meth. **A290** (1990) 320–326.

[47] L. Bugge *et al., Large Area Silicon Detectors with Front End Electronics in VLSI as a Luminosity Monitor at LEP,* Oslo report OSLO–**86–10**, April 1986.

[48] (a) The DELPHI Collaboration, *Proposal for the Replacement of the Small Angle Calorimeter of DELPHI,* CERN/LEPC report **92–6**, 1992.

(b) A. Benvenuti *et al., STIC, the New DELPHI Luminosity Monitor,* Proc. 4th International Conference on Calorimetry in High Energy Physics (La Biodola, September 1993); CERN/DELPHI note **94–31** CAL–112, 23rd March 1994.

(c) S.J. Alvsvåg *et al., The DELPHI Small Angle Tile Calorimeter,* Proc. Nuclear Science Symposium and Medical Imaging Conference (Norfolk, October 1994), ed. E. Barsotti, IEEE Trans. Nucl. Sci. **42** (1995) 478–484.

(d) The DELPHI Collaboration, *Performance of the New High Precision Luminosity Monitor of DELPHI at LEP,* Proc. International Europhysics Conference on High-Energy Physics (EPS–HEP'95, Brussels, July 1995); CERN/DELPHI note **95–68** PHYS–503.

[49] (a) S. Almehed *et al., A Silicon-Tungsten Electromagnetic Calorimeter for LEP,* Nucl. Instr. and Meth. **A305** (1991) 320–330.

(b) DELPHI Collaboration, *High precision relative luminosity measurement with a Very Small Angle Tagger (VSAT) in DELPHI,* Proc. 26th International Conference on High-Energy Physics (ICHEP'92, Dallas, August 1992); CERN/DELPHI note **92–77** PHYS–188.

[50] R.Q. Apsey *et al., Design of a 5.5 Metre Diameter Superconducting Solenoid for the DELPHI Particle Physics Experiment at LEP,* Proc. Applied Superconductivity Conference (San Diego, September 1984), ed. M.A. Green, IEEE Trans. Magnetics **21** (1985) 490–493.

[51] W. Adam *et al., Design and Performance of the DELPHI Data Acquisition System,* Proc. 7th Conference on Real-Time Computer Applications in Nuclear, Particle and Plasma Physics (RT91, Julich, June 1991), ed. F.A. Kirsten, IEEE Trans. Nucl. Sci. **39** (1992) 166–175.

[52] (a) V. Bocci *et al., Basic Concepts and Architectural Details of the DELPHI Trigger System,* Proc. Nuclear Science Symposium and Medical Imaging Conference (Norfolk, October 1994), ed. E. Barsotti, IEEE Trans. Nucl. Sci. **42** (1995) 837–843.

(b) V. Bocci *et al., Architecture and Performance of the DELPHI Trigger System,* Nucl. Instr. and Meth. **A362** (1995) 361–385.

[53] US National Instrumentation Methods (NIM) Committee, *FASTBUS Modular High Speed Data Acquisition and Control System,* US Department of Energy Division of High Energy Physics, DOE/ER–0189.

[54] DELPHI Collaboration, *DELPHI Data Analysis Program (DELANA) User's Guide,* CERN/DELPHI note **89–44** PROG–137, 17th May 1989.

[55] D. Bertrand and L. Pape, *TANAGRA, Track Analysis and Graphics Package,* CERN/DELPHI note **87–95** PROG–98, 13th November 1987.

[56] Yu. Belokopytov, S. Gumenyuk, V. Perevozchikov, *DELPHI Detector Description Application Package User Manual,* CERN/DELPHI note **90–37** PROG–154, 29th July 1990.

[57] J. Wickens, *DELANA Tags for 1991 Data,* CERN/DELPHI note **91–20** PHYS–91 PROG–160, 30th April 1991.

[58] J. Wickens, *Physics Team Tagging Critera in PXTAG,* CERN/DELPHI note **92–44** PROG–184, 14th April 1992.

[59] T. Adye *et al., Fixing Routines,* chapter 11 in [28] *ibid.*

[60] (a) P. Abreu *et al., First Measurement of the Strange Quark Asymmetry at the* Z^0 *Peak,* Z. Phys **C67** (1995) 1–13.

(b) P. Abreu *et al., Charged Kaon Production in Tau Decays at LEP,* Phys. Lett. **B334** (1994) 435–449.

[61] L. Chevalier, *Identification des Particules par leur Ionisation dans la Chambre a Échantillonnage Temporel de DELPHI,* doctoral thesis, Saclay, DAPNIA/SPP **92–32**, 1992.

[62] P. Bambade and P. Zalewski, *Study of Electron Identification in Hadronic Jets,* CERN/DELPHI note **92–32** PROG–183, 7th May 1992.

[63] (a) G.V. Borisov, *Lifetime Tag of Events* $Z^0 \to b\bar{b}$ *with the DELPHI detector: AABTAG program,* CERN/DELPHI note **94–125** PROG–208, 11th August 1994.

(b) W.J. Murray, *Improved B tagging using Impact Parameters,* CERN/DELPHI note **95–167** PHYS–581, 20th November 1995.

[64] M. Goosens, O. Schaile, J. Shiers, J. Zoll, *ZEBRA,* CERN Program Library Long Writeup **Q100/Q101**, February 1994.

[65] Ph. Charpentier *et al., DELPHI Event Data Layout: Online and Offline Formats,* CERN/DELPHI note **88–64** PROG–115 DAS–88, revised 22nd February 1989.

[66] Y. Sacquin, *Description of the DELPHI DST Content,* CERN/DELPHI note **94–161** PROG–210, revised 20th December 1994.

[67] Tz. Spassoff, *DELPHI LongDST Content,* Version 1.03, CERN/DELPHI note in preparation, 1st April 1996.

[68] Tz. Spassoff, *DELPHI ShortDST Content,* Version 1.03, CERN/DELPHI note in preparation, 1st April 1996.

[69] Tz. Spassoff, *DELPHI MiniDST Content,* Version 1.02, CERN/DELPHI note in preparation, 4th October 1995.

[70] H.J. Klein and J. Zoll, *PATCHY Reference Manual,* Version 4.13, CERN Program Library Long Writeup, March 1988.

[71] P. Billoir, *Track Fitting with Multiple Scattering: A New Method,* Nucl. Instr. and Meth. **225** (1984) 352–366.

[72] W.J. Murray, *Measurement of the Beam Position in DELPHI,* CERN/DELPHI note **96–6** PHYS–590, 5th February 1996.

[73] (a) G. Wilkinson, *Muon Identification,* chapter 4 in *A Study of* $B^0\bar{B}^0$ *Oscillations at the* Z^0 *Resonance,* doctoral thesis, University of Oxford, RAL report **RALT–173,** August 1993.

(b) P.R. Collins, *Lepton Identification and Sample Selection*, chapter 3 in [1], *ibid.*

(c) F. Stichelbaut and G.R. Wilkinson, *Performance of Muon Identification in DELPHI for the 93 and 94 Data,* CERN/DELPHI note **95–140** PHYS–565, 30th August 1995.

(d) G. Wilkinson, *Improvements to the Muon Identification in the 94C2 Short DST Production,* CERN/DELPHI note **97–37** PHYS–690, 23rd April 1997.

[74] N. Crosland, P. Kluit, G. Wilkinson, *EMMASS Muon Identification Within DELPHI,* CERN/DELPHI note **92–17** PHYS–157, 10th February 1992.

[75] P.R. Collins and G.R. Wilkinson, *MUCFIX — Refining the Muon Chamber Information on the DST,* CERN/DELPHI note **93–13** PHYS–262, 4th March 1993.

[76] L. De Boeck and G.R. Wilkinson, *MUFLAG — A Framework for Muon Identification,* CERN/DELPHI note **93–14** PHYS–263, 1st April 1993.

[77] (a) DELPHI Collaboration, *DELSIM, Delphi Event Generation and Detector Simulation User's guide,* CERN/DELPHI note **89–67** PROG–142, 10th July 1989.

(b) DELPHI Collaboration, *DELSIM, DELPHI Event Generation and Detector Simulation Reference Manual,* CERN/DELPHI note **89–68** PROG–143, 1st September 1989.

[78] T. Sjöstrand, *High-Energy-Physics Event Generation with PYTHIA 5.7 and JETSET 7.4,* Comput. Phys. Commun. **82** (1994) 74–90.

[79] Application Software Group, *GEANT — Detector Description and Simulation Tool,* CERN Program Library long writeup **W5013**, October 1994.

[80] C.A.E.N. (Costruzioni Apparecchiature Elettroniche Nucleari s.r.l.), *SY127 High Voltage System, Technical Information Manual,* Viareggio, Italy, September 1986.

[81] T. Adye, A. Augustinus, M. Dönszelmann, T. Rovelli, R. Sekulin, G. Smith, *The Slow Controls of the DELPHI Experiment at LEP,* Proc. 10th Conference on Computing in High Energy Physics (CHEP92, Annecy, September 1992), ed. C. Verkerk and W. Wojcik, CERN report **92–07** (1992) 765–768.

[82] T.J. Adye, A. Augustinus, M. Dönszelmann, T. Rovelli, R.L. Sekulin, G.R. Smith, *The Design and Operation of the Slow Controls for the DELPHI Experiment at LEP,* RAL report **94–029** and CERN/ECP preprint **94–3**, 18th March 1994; Nucl. Instr. and Meth. **A349** (1994) 160–182.

[83] R.C.A. Brown, H. Hofmann, D. Pegat, B. Vullierme, M. Kajetanowicz, *Distributed Engineering Controls for the DELPHI Gas Supply System,* Proc. IEEE Nuclear Science Symposium (Orlando, November 1988), ed. R. Pordes, IEEE Trans. Nucl. Sci. **36** (1989) 71–73.

[84] (a) J-P. Puget, E. Sbrissa, L. Vinot, *The General Surveillance System (GSS),* CERN/ECP note **94–5**, 22nd April 1994.

(b) R. Sekulin and G. Smith, *Safety Considerations for DELPHI Slow Controls,* CERN/DELPHI note **88–34** DAS–79, 11th May 1988.

[85] ALEPH: T. Charity, J-M. Maugain, W. von Rüden, S. Wheeler, J. Thomas, *The ALEPH Slow Control System,* Proc. 8th Conference on Computing in High Energy Physics (CHEP90, Santa Fe, April 1990), ed. J. Lillberg and M. Oothoudt, AIP Conference Proceedings **209** (1990) 386–394.

[86] L3: J.M. Le Goff *et al., Use of an Expert System to Monitor and Control a Large High Energy Physics Experiment at CERN: The L-3 Slow Control,* Proc. Conference on Software Engineering Artificial Intelligence Applications in High Energy Physics (Lyon, March 1989), New Computing Techniques in Physics Research CNRS (1990) 403–417.

[87] OPAL: A.K. Amundsen, C. Beard, H.J. Burckhart, R. Hammarström, S. Jaffer, E. Meynet, *The Control System of the OPAL Detector at LEP,* Nucl. Instr. and Meth. **A293** (1990) 145–147.

[88] C. Meroni, W. Kucewicz, A. Stocchi, *μVertex Slow Control Manual,* CERN/DELPHI note **90–52** PROG–157, 6th November 1990.

[89] M. Battaglia *et al., A Capacitive Displacement Monitor System for the DELPHI Microvertex Detector,* Proc. International Conference on Advanced Technology and Particle Physics (Como, June 1990), ed. E. Borachi *at al.,* Nucl. Phys. B (Proc. Suppl.) **23A** (1991) 448–456.

[90] A. Tsirou *et al., A control system for the DELPHI RICH fluids,* CERN/DELPHI note **95–168** RICH–86, 20th November 1995.

[91] M. Sannino and E. Durante, *Alignment in Magnetic Field, Charge Transmission and Drift Velocity Monitoring for the TPC-like Electromagnetic Calorimeter of the DELPHI Experiment at LEP,* CERN/DELPHI note **87–78** CAL–48, 25th September 1987.

[92] M. Voutilainen, *Hardware of the DELPHI Hadron Calorimeter High Voltage Control System,* CERN/DELPHI note **91–15** DAS–109 CAL–80, 21st March 1991; and Helsinki University, HU–SEFT–**1991–06** (1991).

[93] M. Voutilainen, *DELPHI Hadron Calorimeter High Voltage Current Monitor,* CERN/DELPHI note **91–13** DAS–107 CAL–78, 21st March 1991; and Helsinki University, HU–SEFT–**1991–04** (1991).

[94] M. Voutilainen, *Hardware of the DELPHI Hadron Calorimeter Front End Elecronics Control,* CERN/DELPHI note **91–14** DAS–108 CAL–79, 21st March 1991; and Helsinki University, HU–SEFT–**1991–05** (1991).

[95] F. Cao, *The Muon Chambers and the Slow Control System for the Monitoring of the Drift Velocity of the Forward Muon Chambers,* chapter 4 in *A study of the Z^0 Lineshape at LEP through the Reaction $e^+e^- \to \mu^+\mu^-$,* doctoral thesis, Vrije Universiteit Brussel, December 1993.

[96] P. Allen, M. de Fez, A. Ferrer, J. Cuevas, A. Ruiz, *Detector Description Database for the DELPHI Time of Flight Counter,* CERN/DELPHI note **92–152** PROG–191, 2nd November 1992.

[97] H. Abie *et al., The Slow Control System of the DELPHI Small Angle Tagger (SAT) and Very Small Angle Tagger (VSAT),* CERN/DELPHI note **94–6** PROG–204, 21st March 1994.

[98] (a) Gespac SA, *Gespac G-64 and G-96 Specifications Manual,* Geneva, November 1984.

(b) P. Wolstenholme, *The Definition of the G-64 Compatible Bus,* CERN/SPS/ACC technical note **83–24**, 1983.

(c) R. Sekulin and G. Smith, *Specifications for G64 Hardware for use within DELPHI,* CERN/DELPHI note **86–48** DAS–33, April 1986.

[99] A.E. Ball, *MAC-G64 Monitoring and Control — G64 Based System,* CERN/EF note, 20th November 1985.

[100] A. Ball, G. Smith, J. Zaslavski, *Input Output Cards for use with the MAC Chassis,* CERN/EF note, June 1987.

[101] B. Flockhart *et al., 68B09E Paging Processor,* Version 2, SPS 6606–01C, unpublished CERN/SPS note, 16th February 1986.

[102] Motorola Inc., *MC6809–MC6809E 8-bit Microprocessor Programming Manual,* Original Issue, M6809PM(AD), Austin, Texas, 1st March 1981.

[103] (a) S. Brobecker, J. Joosten, *Intelligent Card for Ethernet in G64,* CERN/CS note, December 1988.

(b) P. Lorenz, *Performance measurements with the CATS Enhanced Performance Interface in G64 computers with Motorola 6809 processor,* CERN/DELPHI note **87–86** DAS–63, 15th October 1987.

[104] C. Illinger, *Putting a G64 Program into ROM,* CERN/DELPHI note **90–32** DAS–104, July 1990.

[105] Technical Systems Consultants Inc, *FLEX User's Manual,* Version 9.0, Chapel Hill, North Carolina, 1979.

[106] Certified Software Corporation, *Omegasoft 6809 Pascal Version 2 Language Handbook,* order no. **MPCS2**, Camarillo, California, 1983.

[107] T. Adye and G. Smith, *Using the Paging Facility of the SPS 256k G64 Processor,* CERN/DELPHI note **94–12** DAS–149, 17th October 1994.

[108] T. Adye, T. Berners-Lee, S. Brobecker, A. Camacho, D. Davids, F. Harris, P. Lorenz, *Online Communications in the DELPHI Experiment,* Proc. Conference on Computing in High Energy Physics (CHEP89, Oxford, April 1989), ed. R.C.E. Devenish and T. Daniels, Comput. Phys. Commun. **57** (1989) 466–471.

[109] J-P. Ansart, *OSIAM_C, The OSI Tool Box,* Version 2.0, MARBEN Informatique, Paris.

[110] D. Davids, *CATS/TP4 Software User Manual,* Version 5.0, unpublished CERN/CN note, 1st July 1990.

[111] G. Heiman and T.J. Berners-Lee, *The "CATS" Transport Service Calling Sequence,* Version 4.0.3, CERN/DD/CS note, June 1989.

[112] (a) T.J. Berners-Lee, *Experience with Remote Procedure Call in Data Acquisition and Control,* Proc. 5th Conference on Real-Time Computer Applications in Nuclear, Particle and Plasma Physics (RT87, San Francisco, May 1987), ed. R.T. Kouzes, IEEE Trans. Nucl. Sci. **34** (1987) 1050–1053.

(b) T.J. Berners-Lee, *RPC User Manual,* Version 2.4.0, CERN/DD/OC Writeup, July 1989.

[113] G. Smith, *DELPHI Slow Controls G64 Microcomputers Skeleton Program,* Version 4.2, CERN/DELPHI note **94–13** DAS–150, revised 24th June 1994.

[114] Digital Equipment Corporation, *VMS System Services Reference Manual,* Version 5.5, Maynard, Massachusetts, November 1991.

[115] Digital Equipment Corporation, *VAX FORTRAN Reference Manual,* Version 5.0, Maynard, Massachusetts, May 1988.

[116] M. Metcalf, *Effective Fortran 77,* Clarendon Press, Oxford, 1985.

[117] K. Jensen and N. Wirth, *Pascal User Manual and Report,* Springer-Verlag, New York–Heidelberg–Berlin, 1975.

[118] B.W. Kernighan and D.M. Ritchie, *The C Programming Language,* Second Edition, Prentice Hall, New Jersey, 1988.

[119] *Reference Manual for the Ada Programming Language,* ANSI/MIL–STD–1815A–1983, ISO/8652–1987, Ada Joint Program Office, OUSDRE(R&AT), The Pentagon, Washington D.C., 1983.

[120] Digital Equipment Corporation, *VMS RTL Screen Management (*`SMG$`*) Manual,* Maynard, Massachusetts, June 1989.

[121] C. Boissat, R. Jones, G. Mornacchi, *The Model Human Interface,* Proc. Conference on Computing in High Energy Physics (CHEP89, Oxford, April 1989), ed. R.C.E. Devenish and T. Daniels, Comput. Phys. Commun. **57** (1989) 512–515.

[122] (a) J. Gettys, R.W. Scheifler, R. Newman, *Xlib — C Language X Interface, MIT X Consortium Standard,* X Version 11, Release 4, Massachusetts Institute of Technology, Cambridge, Massachusetts; and Digital Equipment Corporation, Maynard, Massachusetts, 1989.

(b) J. McCormack, P. Asente, R.R. Swick, *X Toolkit Intrinsics — C Language Interface, X Window System,* X Version 11, Release 4, Massachusetts Institute of Technology, Cambridge, Massachusetts; and Digital Equipment Corporation, Maynard, Massachusetts, 1988.

[123] Open Software Foundation, *OSF/Motif Programmer's Reference,* Release 1.1, Prentice Hall, 1990.

[124] M. Dönszelmann, *DELPHI HIPE System User Manual,* Version 2.30, CERN/DELPHI note **92–26** DAS–124, 6th October 1992.

[125] P. Burkimsher, *EMU, The MODEL Error Message Utility,* Version 2.1, CERN/ECP Writeup, December 1990.

[126] F. Harris and K. Spang, *The Use of EMU in the DELPHI Online System,* CERN/DELPHI note **89–19** DAS–95, 16th March 1989.

[127] A. Augustinus, *DELPHI Automatic Beep Caller Facility, Reference Manual,* CERN/DELPHI note **94–17** DAS–154, 22nd February 1994.

[128] T. Rovelli, *The EMU Messages Display Utility,* CERN/DELPHI note **93–30** DAS–142, 24th March 1993.

[129] (a) F. Carena and G. Gopal, *Cargo Data Base Management Systems Manual,* CERN/DELPHI note **86–28** PROG–46, 8th July 1986.

(b) Yu. Belokopytov and V. Perevozchikov, *CARGO Database Management Package,* CERN/DELPHI note **93–5** PROG–195, 29th March 1993.

[130] R. Matthews, *KAPACK: Random Access I/O Using Keywords,* Version 2.12, CERN Program Library Writeup **Z303**, 7th February 1986.

[131] T. Adye, F. Fontanelli, G. Gopal, G. Smith, *Slow Control Database Manual,* CERN/DELPHI note **94–15** DAS–152, 17th October 1994.

[132] Yu. Belokopytov, G. Gopal, V. Perevozchikov, H. Klein, W. Venus, *The DELPHI Database Description: Calibration & Detector Status File,* CERN/DELPHI note **93–4** PROG–194 DAS–138, 22nd November 1993.

[133] (a) J. Barlow, B. Franek, M. Jonker, T. Nguyen, P. Vande Vyvre, A. Vascotto, *Run Control in MODEL: The State Manager,* Proc. 6th Conference on Real-Time Computer Applications in Nuclear, Particle and Plasma Physics (RT89, Williamsburg, May 1989), ed. R. Pordes, IEEE Trans. Nucl. Sci. **36** (1989) 1549–1553.

(b) A. Defendini, R. Jones, J.-P. Matheys, P. Vande Vyvre, A. Vascotto, *The State Manager: A Tool to Control Large Data-Acquisition Systems,* Proc. International Conference on Accelerator and Large Experimental Physics Control Systems (ICALEPCS'91, Tsukuba, November 1991), ed. C.O. Pak, S. Kurokawa, T. Katoh, KEK Proceedings **92-15** (1992) 524–527.

[134] C. Gaspar and M. Dönszelmann, *DIM — A Distributed Information Management System for the DELPHI Experiment at CERN,* Proc. 8th Conference on Real-Time Computer Applications in Nuclear, Particle and Plasma Physics (RT93, Vancouver, June 1993), ed. D. Axen and R. Poutissou, TRIUMF **93–1** (1993) 156–158.

[135] (a) R. Jones, G. Mornacchi, R. Russell, *OSP User's Guide,* Version 3.0, CERN DD/OC Writeup, 26th July 1990.

(b) A. Defendini, B. Franek, J.-P. Matheys, P. Vande Vyvre, A. Vascotto, *Inter-process Control Transactions,* Appendix C in *The MODEL State Manager User Manual,* Version 2.3, CERN/EPC/DS Writeup, 2nd April 1991.

[136] (a) M. Dönszelmann, C. Gaspar, J.A. Valls, *A Configurable Motif Interface for the DELPHI Experiment at LEP,* Proc. International Motif User Conference (Washington DC, December 1992); and CERN/DELPHI note **92–150** DAS–134, 2nd November 1992.

(b) M. Dönszelmann, *DELPHI User Interface Guide,* CERN/DELPHI note **92–149** DAS–133, 24th March 1993.

[137] M. Dönszelmann and C. Gaspar, *The DELPHI Distributed Information System for Exchanging LEP Machine Related Information,* Proc. 3rd International Conference on Accelerator and Large Experimental Physics Control Systems (ICALEPCS'93, Berlin, October 1993), ed. W. Busse and M.C. Crowley-Milling, Nucl. Instr. and Meth. **A352** (1994) 280–282.

[138] B. Franek *et al., Big Brother — A Fully Automated Control System for the DELPHI Experiment,* Proc. 12th Conference on Computing in High Energy Physics (CHEP94, San Francisco, April 1994), ed. S.C. Loken, LBL C94/04/21, 1994.

[139] A. Augustinus and B. Ginoux Defermon, *Evaluation of the use of a Processor from the 68000-family in a G64 Environment,* CERN/DELPHI note **94–16** DAS–153, 22nd February 1994.

[140] R. Barillere *et al., The Cortex Project: A Quasi-real-time Information System to Build Control Systems for High Energy Physics Experiments,* Proc. 3rd International Conference on Accelerator and Large Experimental Physics Control Systems (ICALEPCS'93, Berlin, October 1993), ed. W. Busse and M.C. Crowley-Milling, Nucl. Instr. and Meth. **A352** (1994) 492–496.

[141] T. Sjöstrand, *Event Shapes,* section 15.1 of *PYTHIA 5.7 and JETSET 7.4: Physics and Manual,* LU–TP–95–20, CERN Program Library Long Writeup **W5035/W5044**, August 1995; unpublished appendix to *High-Energy Physics Event Generation with PYTHIA 5.7 and JETSET 7.4,* Comput. Phys. Commun. **82** (1994) 74–90.

[142] P. Billoir, R. Frühwirth, M. Regler, *Track Element Merging Strategy and Vertex Fitting in Complex Modular Detectors,* Nucl. Instr. and Meth. **A241** (1985) 115–131.

[143] T. Adye *et al., Vertex Physics Routines,* chapter 8 in *DST Analysis Libraries Writeup,* ed. P.D. Dauncey and L. Mirabito, unpublished CERN/DELPHI note, 14th July 1994.

[144] Application Software and Databases Group, *Ntuples,* chapter 3 of *HBOOK Reference Manual — Statistical Analysis and Histogramming,* CERN Program Library Long Writeup **Y250**, May 1995.

[145] Application Software Group, *PAW — Physics Analysis Workstation — An Introductory Tutorial,* CERN Program Library Long Writeup **Q121**, February 1995.

[146] P. Abreu *et al.,* J/ψ *Production in the Hadronic Decays of the Z,* Phys. Lett. **B341** (1994) 109–122.

[147] Application Software Group, *COMIS — Compilation and Interpretation System — Reference Manual, Version 2,* CERN Program Library Long Writeup **L210**, July 1993.

[148] F. James, *MINUIT — Function Minimization and Error Analysis — Reference Manual,* CERN Program Library Long Writeup **D506**, March 1994.

[149] B. Franek, *A Production Model Independent Calculation of Charmed Particle Lifetime Using Unconstrained Decays,* RAL Report RAL–**85–026**, May 1985.

[150] G. Alexander *et al., Observation of* J/ψ *Production in Multihadronic* Z^0 *Decays,* Phys. Lett. **B266** (1991) 485–496.

[151] D. Buskulic *et al., Measurements of Mean Lifetime and Branching Fractions of B Hadrons Decaying to* J/ψ*,* Phys. Lett. **B295** (1992) 396–408.

[152] M. Acciarri *et al., Inclusive J,* ψ' *and* χ_{c} *Production in Hadronic Z Decays,* Phys. Lett. **B407** (1997) 351–360.

[153] The ALEPH Collaboration, *Study of prompt* J/ψ *production in hadronic Z decays,* Proc. XVIII International Symposium on Lepton Photon Interactions (LP'97, Hamburg, July 1997).

[154] D. Crennell, C.M. Fisher, R.L. Sekulin, *The Possibility to Study the Production and Decay Systematics of Short-lived* ($\gtrsim 10^{-13}s$) *New Particles in Hadronic Reactions using the Bubble Chamber Technique,* Nucl. Instr. and Meth. **158** (1979) 111.

[155] R. Barlow, *Statistics: A Guide to the Use of Statistical Methods in the Physical Sciences,* John Wiley and Sons, Chichester, 1989.

[156] Particle Data Group, K. Hikasa *et al.*, *Review of Particle Properties,* Phys. Rev. **D45** (1992) Part II.

[157] Particle Data Group, L. Montanet *et al.*, *Review of Particle Properties,* Phys. Rev. **D50** (1994) Part I.

DELPHI notes given here as reference may be obtained from the author or from the DELPHI secretariat (CERN, Geneva, Switzerland; or via electronic mail at `Delphi.Notes@cern.ch`).